Politecnico di Milano
Department of Aerospace Science and Technology
Doctoral Programme In Aerospace Engineering

BLADE PASSIVE SOLUTIONS FOR LOAD MITIGATION ON MULTI-MEGAWATT WIND TURBINES

Doctoral Dissertation of:
Pierluigi Montinari

Supervisor:
Prof. Carlo L. Bottasso

Tutor:
Prof. Gianluca Ghiringhelli

The Chair of the Doctoral Program:
Prof. Luigi Vigevano

Year 2017 Cycle XXIX

Acknowledgments

This dissertation is the fruit of my research work in three years of PhD, during which I have developed expertise and great interest in the topics presented.

The thesis has been accomplished by valued reviews of Prof. Dr. Po Wen Cheng of SWE at University of Stuttgart and Prof. Dr. Lorenzo Battisti of the Department of Civil, Environmental and Mechanical Engineering at University of Trento.

A special acknowledgment goes to my supervisor Prof. Dr. Carlo Bottasso, he has put his experience and expertise at my disposal, giving me inestimable advices.

Thanks also to Prof. Dr. Alessandro Croce and the other colleagues of POLI-Wind, they have contributed to this result through continuous exchanges of material and of ideas that have fed the growth of my competences. Thanks to all the members of the Wind Energy Institute at Technical University of Munich for the fruitful collaboration and helpful support.

Valuable help has been provided by master's thesis students, that have assisted me in the experimental activities.

The exchanges with the European Wind Energy Academy during seminars and conferences and INNWIND.EU project members during meetings are also gratefully acknowledged.

Last but not least I want to address a special thought to my family, my relatives and to those friends that have supported me during ups and downs in this path. They have partly contributed to the achievement of this result.

Vorrei infine volgere un pensiero alla mia famiglia, ai miei parenti ed agli amici che mi hanno sempre sostenuto ed hanno condiviso con me momenti difficili, gioie e soddisfazioni durante questo percorso, prendendo parte al raggiungimento di questo risultato.

Summary

Over the last twenty years wind energy sector has grown remarkably. At the same time, the size of the wind turbine has increased exponentially, mainly for the following reasons: first, larger wind turbines capture more wind power because of greater area swept by the blades, and taller towers allows operation at higher altitudes, escaping the worst conditions of turbulence, obstacles and wind shear near the surface of the earth; second, the costs to control, connect to the grid and maintain are sometimes higher than the capital value of the wind farms, therefore installing greater wind turbines implies reducing the costs for grid connections; third, larger wind turbines provide better land utilisation. To satisfy this trend of growth, with a look on the growth forecast of the future machines, a simple upscaling of the existing ones using the same technology is unfeasible, since the cost of a wind turbine is typically well correlated with its weight and weight with the size of the rotor, following the well known cubic law. Therefore, a naive scaling would translate into an unacceptable growth of cost. Among other approaches, *load alleviation* techniques help address this issue, by increasing the efficiency of the aerostructural configuration and limiting the cost grow rate of wind turbine components through the design of lighter structures and/or the reduced usage of high performance materials. In this dissertation, blade solutions for load alleviation are investigated. At the beginning, *passive* or *active* and *distributed/full-blade span* solutions for load reduction implemented on blades is reviewed. The thesis investigates beyond what has been already conceived for the wind energy systems in this context, focusing on the study of potential of passive solutions to mitigate the loads and to work in synergy with active architectures, with the goal of reducing the Cost of Energy.

The first part of the thesis describes new concepts, based on the deployment of distributed appended devices, mostly used in a passive way, and trying to exploit several tuning approaches, with the goal of demonstrating that passive means of actuation can lead to enhanced performance comparable to more complex active architectures. Extensive analyses are conducted for assessing the impact of the

technology on fatigue and ultimate loads, and evaluating the effects on the annual energy production.

Two types of tuning for passive flaps and free pitching tips are identified as very effective for reducing both fatigue and ultimate loads: *inertial* and *aerodynamic* tuning. In both cases, the goal is to reduce loads with devices that are as simple as possible, do not require sensors nor actuators, resulting in reliable and cheap solutions. They move in response to the structure accelerations and/or in response to the airloads. The modeling and the analysis are conducted preliminarily considering simpler and faster simulation models, with the scope of assessing the feasibility of the passive devices in load mitigation. Then, more complex high-fidelity aeroelastic models in the multibody simulation environment are considered, using large conceptual 10 MW wind turbine model as baseline. Results highlight very interesting capabilities of such devices in mitigating both fatigue and ultimate loads.

The second part of the thesis describes the characterization of *full-blade span* solutions, with the goal of demonstrating via experiments the potential of this means to mitigate loads, withstanding and sometimes complementary to active control architectures. To this end, a scaled representation of a multi-megawatt wind turbine featured with *Bend-Twist Coupling* is realized and characterized in terms of structure, aerodynamics and loads. Blade structural characterization is conducted at bench, by means of dynamic frequency response analysis and static tests. The blade structural properties' identification problem is formulated as a maximum-likelihood constrained optimization, and is performed successfully.

Wind tunnel of *Politecnico di Milano* is used for the aerodynamic and load characterization. The former requires the determination of thrust and power coefficients. To this end, some tests are conducted in the aeronautical section with low turbulence intensity, where different blade pitch angles and tip speed ratios are tested. For the load characterization, boundary layer chamber is used to generate scaled turbulent wind conditions. The model is also tested in partial wake conditions, as likely to occur in wind farm operations. The synergic effect with the active load mitigation strategy is also shown by enabling the *Individual Pitch Control*.

Finally, conclusions and outlook for possible future developments on the topic are drawn.

Contents

List of Figures

List of Tables

List of Acronyms

IEA	International Energy Association
CoE	Cost of energy
LTI	Linear time invariant
DEL	Damage equivalent load
FEM	Finite element method
DLC	Dynamic load case
BEM	Blade element momentum
HAWT	Horizontal axis wind turbine
RWT	Reference wind turbine
LQR	Linear quadratic regulator
AoA	Angle of attack
NTM	Normal turbulence model
ETM	Extreme turbulence model
AEP	Annual energy production
AC	Aerodynamic center
ADC	Actuator duty cycle
BTC	Bend-twist coupling
CG	Center of gravity
DLC	Dynamic load case
EOG	Extreme operating gust
HL	Hinge line
IPC	Individual pitch control
NWP	Normal wind profile
SF	Scale factor
TSR	Tip speed ratio
CNC	Computer numerical control
MW	Mega Watt
FBG	Fiber Bragg Grating
TSR	Tip speed ratio
FRF	Frequency Responce Function

LSCE	Least Squares Complex Exponential
MAC	Modal Assurance Criterion
CAN	Controller area network
PI	Proportional integral
FO	Fiber Optic
FORJ	Fiber Optic Rotary Joint
DOF	Degree Of Freedom
SQP	Sequence Quadratic Programming
SVD	Singular Value Decomposition

List of Symbols

a	Non-dimensional distance between elastic axis and section mid chord
c	Blade chord
e	Distance between flap hinge and mid chord
l	Distance between flap hinge and airfoil trailing edge
b	Section semi-chord
t	Time
τ	Reduced time, Transmission ratio
T	Time interval
h	Plunge motion
m	Mass
m_o	Offset mass
q	Dynamic pressure
S_f	Flap surface
c_f	Flap chord
s	Complex number frequency
s'	Reduced frequency
k,K	Stiffness
k_h, k_θ, k_δ	Plunge, torsion and flap stiffnesses
k_0, k_Ω	Constant stiffness and centrifugal stiffening coefficient
c_h, c_θ, c_δ	Plunge, torsion and flap dampings
V	Wind speed
U	Flow speed
U_e	External flow speed
J	Inertia
C_L	Lift coefficient
C_D	Drag coefficient
C_M	Pitching moment coefficient
C_H	Hinge moment coefficient
P_0	Screw pitch

$\mathbf{x}$	State vector
$\mathbf{u}$	Input vector
$\mathbf{M}$	Mass matrix
$\mathbf{C}$	Damping matrix
$\mathbf{K}$	Stiffness matrix
$\mathbf{A}$	State matrix
$\mathbf{B}$	Input matrix
$\mathbf{A}^{AE}$	Aerodynamic matrix
$\mathbf{r}_1$	Aerodynamic coefficients vector
$\mathbf{s}_1$	Aerodynamic arms vector
$\mathbf{s}_2$	Aerodynamic arms vector
C	Theodorsen function
α	Angle of attack
α_{bl}	Boundary layer power coefficient
β	Blade pitch angle
θ	Torsional rotation, Blade tip relative rotation, Blade twist
δ	Flap deflection, Boundary layer thickness
σ	Integration variable
ψ	Küssner function
ϕ	Wagner function
ρ	Air density
F	Force
g	Gravitational acceleration
J	Moment of inertia
M	Moment
r	Radial position
V	Wind speed
z	Tip spanwise displacement, Vertical position
ψ	Blade azimuth
ω	Modal frequency
Ω	Rotor angular speed
d	Arm wrt hinge
s	Spanwise distribution
n	Scale factor
n_t	Rotor speed ratio
t_{ply}	Single composite ply thickness
R	Rotor radius
$C_{L,\alpha}$	Lift curve slope
W	Blade weight
V_r	Rated wind speed
D	List of given input data
J	Optimization cost function
T_g	Generator torque
T_a	Aerodynamic torque
C_T	Torque coefficient

C_P	Power coefficient
C_F	Thrust coefficient
χ	Vector of shape functions
$\mathbf{p}_s$	Vector of structural design parameters
$\mathbf{K}_{flap}$	Vector of blade flap-wise stiffness distribution
$\mathbf{K}_{edge}$	Vector of blade edge-wise stiffness distribution
$\mathbf{K}_{tors}$	Vector of blade torsional stiffness distribution
$\mathbf{\Phi}$	Eigen-shape
$\mathbf{m}$	Vector of blade mass distribution
η	Non-dimensional blade span, extent
λ	Tip speed ratio
ζ	Structural damping ratio in percent
ϵ	Constraint tolerance
θ_{spar}	Amount of fiber rotation in the blade spar
Re	Reynolds number
Ma	Mach number
Lo	Lock number
Fr	Froude number
$T_{/*}$	Theodorsen coefficients
$\Delta\bar{p}_a(x)$	Schwarz complex solution
$(\cdot)_{/*}, \partial(\cdot)/\partial(\cdot)$	Partial derivative
$(\cdot)_S$	Structural term
$(\cdot)_{QS}$	Quasi-stationary term
$(\cdot)^{NC}$	Non-circulatory term
$(\cdot)^{C}$	Circulatory term
$(\cdot)^{G}$	Turbulent fluctuation term
$(\cdot)^{AS}$	Aeroelastic term
$\dot{(\cdot)}$	Derivative wrt time, $\mathrm{d}\cdot/\mathrm{d}t$
$\bar{(\cdot)}$	Moving-averaged value
$(\cdot)^*$	Reference value, Optimal quantity
$(\cdot)_a$	Aerodynamic term
$(\cdot)_c$	Centrifugal term
$(\cdot)_d$	Direct (yawing) term
$(\cdot)_g$	Gravity term
$(\cdot)_\Omega$	Rotor speed term
$(\cdot)_i$	Inertial term
$(\cdot)_\delta$,$(\cdot)_f$	Flap term
$(\cdot)_q$	Quadrature (nodding) term
$(\cdot)_{PT}$	Passive tip term
$(\cdot)_{SP}$	Semi-passive tip term
$\check{(\cdot)}$	Experimentally measured quantity
$\hat{(\cdot)}$	Quantity pertaining to the scaled model
$\tilde{(\cdot)}$	Quantity pertaining to the full scale system
$(\cdot)^{(2D)}$	Quantity pertaining the beam model
$(\cdot)^{(3D)}$	Quantity pertaining the 3D FEM model

$(\cdot)^T$	Transpose
$(\cdot)_c$	Quantity pertaining the spar chord position
$(\cdot)_w$	Quantity pertaining the spar width
$(\cdot)_w$	Quantity pertaining the spar thickness
$(\cdot)_{[0]_{s_t}}$	Quantity pertaining the blade with the fiber aligned with the pitch axis
$(\cdot)_{[3]_{s_t}}$	Quantity pertaining the blade with the fiber rotated of 3 deg with respect the pitch axis

CHAPTER 1

Introduction and motivation

During the last twenty years the growth rate of renawable energies has increased considerably. This rapid development has resulted in a significant increment of energy security, climate change mitigation and overall economic benefits. Among the different renewable sources, wind power is one of the most reliable and promising. The growth trend for the wind power is remarkably higher than other sources, such as solar power, biomasses, and similar to hydro power. Nowadays the energy marked records 433 GW of wind power spinning around the globe, supplying more new power generation than any other technology in 2015, as recorded by the International Energy Association (IEA) [1].

Together with the growth of the wind energy market, the size of the wind turbine has increased exponentially, as documented by manufacturers and public agiencies, and it appears to be a general trend in the forecasts for the next thirty years. This growth trend is driven by at least three factors. Firstly, it is clear that larger wind turbines capture more wind power because of greater area swept by the blades, and taller towers allow operation at higher altitudes, escaping worse conditions of turbulence, obstacles and wind shear near the surface of the earth. Secondly, the costs to control, connect to the grid and maintain are sometimes higher than the capital value of the wind farms, therefore installing greater wind turbines implies reducing the costs of grid connections. Finally, larger wind turbines provide better land utilisation.

These factors contribute to the common vision of "bigger is better" among the manufacturers, and powered the focus of public reserach in funding the development of even larger machines.

The early sizes within the range of 20-60 kW were clearly not optimized for the

energy market, since small wind turbines remain much more expensive per kilowatt installed than the large ones, especially if the primary function is to produce electricity for the grid. When larger wind turbines of few hundreds of kilowatts became available, the competitiveness of wind energy increased, and it was clear that most of the economic problems could be avoided by increasing the dimensions of the machines.

Nowadays the onshore market is mainly supplied by wind turbines in the range of 1.5 – 3.0 MW. Some projects have shown potential competitiveness of larger machines up to 7.0 MW. However, the key factor that pushes the development of even larger multi-megawatt machine is the offshore market. According to the US Energy Information Agency, offshore plants are more expensive if compared to the onshore ones, but offshore wind power is much more then the onshore and better fits the demand of the people.

The current state of offshore wind power presents many challenges. In this market wind turbines represent only one-third to one-half [2] of the total costs, the rest coming from infrastructure, maintenance, and oversight. For this reason larger turbines with increased power capability create economic advantages, requiring relatively less installed machines, therefore less infrastructures and grid connections. Installed offshore turbines actually have nominal power capability averaging between 2 MW and 5 MW, with towers taller than 60 m and rotor diameters between 75 and 130 m. Therefore, the maximum height of the structure at the tips of the blades, can reach 150 m. Figure 1.1 shows the largest installed wind turbines each year within the last decades, highlighting the size growth trend in the offshore market. The world's largest wind turbine has nominal power capacity of 8 MW, and even larger turbines are being developed and designed in the range of 10 MW and over, for the next offshore wind energy generation.

Figure 1.1: *Growth in size of installed wind turbines over the last decades.*

To deal with these new challanges, both industries and scientific communities have focused their efforts and identified some key points to bring down the costs of these new generation turbines and make the offshore wind more economically viable. Among them, reducing the weight of turbine materials, implementing load mitigation strategies and improving wind turbine design play central roles. These

three points are strictly linked together, since each one influences the others. Indeed, the implementation of a load reduction strategy helps in reducing the stresses on the structure, therefore making feasible the use of less weight and/or less performant materials and the design of slender components with lower admissible stresses.

1.1 Cost of Energy

The key parameter that shall be considered in designing a new wind energy system is the Cost of Energy (CoE). It represents the way to normalize the comparisons among different technologies and to understand the main drivers concurring to the final cost of the produced energy. According to Ref. [3], it accounts for the overall lifecycle cost divided by the total energy production, as indicated by its formula:

$$\mathrm{CoE} = \frac{\mathrm{FCRxICC}}{\mathrm{AEP}} + \mathrm{AOE} \tag{1.1}$$

The term FCRxICC represents the capital expenditure, with the fixed charge rate (FCR) the annual amount per dollar of initial capital cost needed to cover the capital cost, while the initial capital cost (ICC) is the sum of the turbine system cost and the balance of station cost. Annual operating expenses (AOE) is the operational expediture and (AEP) is the net annual energy production.

The cost of the wind turbine varies considerably depending on the size and on the type of operation (onshore/offshore). It is part of the initial capital cost and contributes for around 45-55%. The grid connection is also a part of the the initial capital cost and can be accounted for 15-25 % of the total cost. The AOE index comprises mostly O&M costs, covering approximatly 20-25% of the total cost, with possible peaks of 30-35% for offshore operations. The AOE also accounts for costs of replacements of components or systems and land lease/rent charged for the wind turbine installation. The AEP in CoE is an essential component and weights some of the factors concurring for the final total cost. Since it does not break out as percentage contributor to the CoE it is more effective to examine how changes in AEP impact the result. The increase in AEP reduces the overall CoE, as stated by the Equation 1.1. Reducing the CoE, thereby increasing the AEP, in the wind energy system would obviously translate into choosing the best windy sites, optimizing the wind turbines interactions and, at the wind turbine level, designing more aerodinamically efficient and larger rotors and taller towers. However, it should be taken into account that the increased rotor diameter would in general increase the weight following the well known cubic law, which in turn tipically translates into increased cost of the wind turbine production, transportation and installation, with a negative contribution on the CoE through the ICC index. Therefore, optimizing the design of the wind turbines in order to increase the rotor sizes by keeping the weight the lowest possible is an interesting challenge with regards to reducing the overall CoE.

1.2 Load mitigation

In recent years, both industry and the scientific community tried to reduce the CoE by different means, among them one of the most effective is to increase the annual

energy production by improving the aerodynamic performances of the rotors and by harvesting a greater amount of energy with larger swept areas and taller towers. To satisfy this growth trend, it is clear now that the simple upscaling of existing machines would be unfeasible, since the cost is typically correlated with weight. Therefore, a naive scaling would translate into an unacceptable exponential growth of cost. Among other approaches, load alleviation techniques help address this issue, by increasing the efficiency of the aerostructural configuration and limiting the cost growth rate of wind turbine components through the design of lighter structures and/or the reduced usage of high performance material [4].

The mitigation of loads can be obtained by different means, among the most promising, *distributed* / *full-span* on-blade solutions play the main role.

Load mitigation by distributed devices

Distributed solutions, locally affect the flow by the use of pitchable tips, flaps, tabs or other devices. The local nature of these solutions allows in principle for a high in space and in time bandwidth, which potentially results in a higher load mitigation effectiveness. The adoption of these devices modifies the standard architecture of the HAWT blade, since they mostly need the installation of further sensors and/or actuators, therefore typically increasing the architecture complexity, which might in turn affect CoE via AOE index, because of higher production and maintenance costs and/or decreased availability. On the other hand, if they are conceived as passive, they do not need sensors or actuators, resulting in simpler implementations that may have a reduced or even negligible impact on CoE.

Numerous distributed active solutions for HAWTs have been exploited, often inspired by aeronautical applications. At present, the most mature applications appear to be the ones based on trailing edge flaps [5–7] although also alternative solutions based on micro-tabs and compliant structures have been considered [8, 9].

Passive distributed techniques were first developed for aeronautical applications. One of the first examples of gust-alleviating passive flaps can be found in [10]. That study developed an experimental setup for investigating in a wind tunnel the effects of a long-period dynamically overbalanced flap on a fixed wing aircraft. Results indicated a reduction of accelerations due to gusts, which was however accompanied by a decrease in stability of the vehicle.

For rotorcraft applications, an analytical investigation of various aeroelastic devices appended to rotor blades is reported by [11]. Among different solutions, a passive trailing edge tab concept is considered in that work using a simplified analysis. That study highlighted the crucial importance of tuning, since the tab motion must be phased in a correct manner to reduce the blade harmonic loads that induce vibrations to the mast. Although results appeared to be promising, the device appeared to be counter-productive when examined more carefully with its overall effects. This study identified also the passive blade tip concept as the most promising technique to improve the aeromechanical qualities of the rotor. Blades were modified in their outermost portion to instal a free pitching tip. The relative rotation between tip and the inner blade was driven by the aeroelastic loads, and the device parameters were tuned to achieve the desired dynamic response.

The design of the passive tip is the outcome of an intense research activity at NASA in the 1980s. The simulation of a passive tip concept is described by [12], aiming at a more uniform airload distribution during the blade revolution by self-adjusting blade tips. Analytical results showed an improvement of lift generated by the rotor in cruise conditions and a reduction of drag and required power. Since the mean relative rotation of the tip is related to the restraining moment at the hinge, a preload was used as a tuning parameter to modulate the blade tip angle of attack and the resulting aerodynamic forces. The passive tip concept was also validated through experiments [13], which confirmed a considerable reduction in required power in high thrust conditions. This result is related to a favorable influence of the blade tip negative pitch angle with respect to the inboard blade portion. Furthermore, the flapwise and control loads were reduced considerably, although no positive effect were observed on the lead-lag loads. Additional studies focused on the configuration of a passive torque controller used to adjust the preload [14]. This fully passive mechanism converts centrifugal loads in a preset torque at the movable tip. Including considerations on simplicity and reliability, the most promising solution appeared to be one that generates the output torque from the tensile loading of two twisted wire straps [15].

Although these studies did show the general ability of passive devices of decreasing loads on the rotors, these advantages are typically offset by an increase of weight, to the point that passive solutions do not seem nowadays to be commonly employed in aeronautical applications. Although active flaps have also not yet arrived on the market, they have seen some significant demonstration by industry [16]. In fact, in aeronautical applications higher levels of complexity are acceptable if they entail superior performance and/or weight savings. Therefore, in this case active flaps might be in general more interesting than passive ones.

The situation appears to be somewhat different in the wind energy field. In fact here, although weight is certainly a concern, the key design figure of merit is the CoE, a quantity that captures the effects of all aspects of the design of a machine over its entire lifetime. For a given load reduction achievable by two devices, the one that might actually bring a benefit to the CoE is the one that is less expensive to manufacture but also, and often more importantly, that is less costly to maintain and that ensures a greater availability. These aspects might be even more important for offshore operations, or in general in remote and difficult to reach locations, where simplicity and robustness might be particularly desirable features. Therefore, from this point of view, deploying in the field a wind turbine with active flaps still seems to be a very significant challenge. Therefore, for wind energy applications a passive solution might be more appealing than an active one, if the former implies greater simplicity, robustness and ease of repair than the latter.

Starting from the aforementioned considerations, recently it appears an intense research activity of the scientific community on several techiques to use passive distributed devices, even if it does not seems that a very effective way has been discovered. Among the first applications of passive distributed solutions is the airfoil camber regulation described by [17]. A passive camber control concept is investigated, considering a 2D aeroelastic typical section. A variation of airfoil camber is

obtained by exploiting the chordwise aerodynamic load distribution, which changes as a function of the angle of attack, while the original shape is restored by the use of a spring and damper. Three simplified load cases are evaluated, showing a significant decrease of load fluctuations. This device will however not only respond to undesirable changes of angle of attack due to blade vibrations, but also to the deliberate changes caused by the full span pitching of the active control system that is responsible for the normal operation of the machine. Furthermore, the flexible airfoil camber will change also with the dynamic pressure function of the operative condition. This would be unacceptable in region II, where the aerodynamic optimum in required, resulting in an unavoidable loss of produced power. The latter considerations cast some doubts on the actual final benefits of this particular solution.

A more recent analysis is reported in [18], where a nonlinear lifting line free vortex wake model is employed to assess the performance of the passive device on a multi-megawatt HAWT. Results indicate a reduction of the standard deviation of blade root bending moments, although a single simulation was considered. However, the overall effects, also at the light of AEP considerations, over the entire operation range were not evaluated and remain an open topic.

Passive load alleviation can also be achieved by structural morphing, as reported by [19,20]. It is based on bistable composite structures. The airfoil camber variation is triggered by the aerodynamic loads that modify the equilibrium condition of a compliant structure with embedded multi-stable elements. This technique results in a discrete control action, because only a finite number of stable configurations are possible. Furthermore, an external load has to be provided to restore the original blade camber.

A fully articulated passive flap was first proposed by [21], and detailed hereinafter in Chapter 2. The idea is in that case to offset the flap center of gravity in front of of the hinge line. This way, flapwise accelerations of the blade excite a response of the flap that, by changing the airfoil camber, tends to oppose the acceleration itself, thereby attenuating blade loading and in turn fatigue. The flap is also aerodynamically balanced, in the sense that it is designed in order not to respond to the deliberate changes in angle of attack imposed by the wind turbine control system. Multiple load cases were considered through a loose coupling procedure based on a state-of-the-art aeroservoelastic simulator and a typical section model, indicating very promising performance.

As the literature shows, a few recent studies have considered passive flaps for HAWTs. The blade free-tip, has been explored and tested only during the 1990s by the FLEXHAT program, [22] and [23]. This study aims at developing the components and the configuration for future wind turbines. The main idea implies the inclusion of flexible components into the rotor structure to reduce the loads. The examined configuration was a two-bladed HAWT with an elastomeric teeter, a flexbeam which allows a limited flapping motion and two passively activated blade tips. Despite the considerable advantages in terms of load reduction, the solution was not further developed due to the complexity of the mechanisms installed on the blades.

The study proposed by [24], and hereinafter reported in Chapter 4 investigates various configurations of blade tips for the alleviation of loads on multi-MW wind turbines. Passive, semi-passive and active solutions are considered in order to provide a general overview of the possible range of configurations and their respective performance. The passive solution is purely activated by aerodynamic loads, while the semi-passive one uses an active component to apply a varying restraining torque to limit mean tip deflections according to the machine operating condition. Finally, the active solution uses an actuator to drive the tip deflection based on a feedback control law. Each configuration is analyzed in detail, including the tuning of the respective parameters. Performance is assessed using the accepted international certification standards within a high-fidelity aeroservoelastic simulation environment.

Load mitigation by full blade span solutions

Besides the distributed devices, the load mitigation can also be achieved by full blade span solutions. They involve the response of the entire blade, and can also be distinguished between active and passive. Individual pitch control (IPC) is a well known full-span active technique, which has been investigated for many years by the scientific community, and which is now seeing an ever increasing acceptance by industries. Bend-twist coupling (BTC) on the other hand, is instead an example of the full-span passive category [25].

Full-span active control techniques have the potential of reducing fatigue and possibly ultimate loads on the main structural components of modern wind turbines: blades, drive-train, bearings and the tower. Current literature describes a variety of architectures and of approaches used for the synthesis of the blade IPC laws [26–29], and some of them have been successfully tested in the field [30]. IPC shows a load reduction capability at the cost of an increased pitch activity. This would require the design of more robust pitch actuators with effect on in initial capital cost and/or maintenance.

At the other end, the full-span passive technique is based on the idea of designing a structure that, when loaded, deforms so as to induce a load reduction. A solution to achieve this structural behavior is to design blades with some degree of bend-twist coupling (BTC). This implies that, when the blade bends because of increased loads, a twisting is induced, with consequent effects on the aerodynamic loading due to the change of the airfoils' angle of attack. Passive load mitigation by BTC can be obtained by exploiting the anisotropic mechanical properties of composite materials, like using off-axis fiber angles, and the literature [31, 32] clearly shows the potential benefits of BTC. This form of load alleviation is very attractive because of its passive nature: there are no actuators which may fail, no moving parts which may wear out, all characteristics that are very interesting for wind turbines, where simplicity, low maintenance and high availability are key factors for reducing the CoE.

Recently, it was shown in [25] that, by properly designing a partially coupled BTC blade, a significant load alleviation on the wind turbine sub-structures can be achieved, together with a consistent reduction of the pitch actuator duty cycle (ADC). In fact, since the blade self-reacts to wind fluctuations, less workload is

demanded to the control system. This result is of potential great interest, because it opens the way to a synergy between passive and active load alleviation technologies: since BTC and IPC can both mitigate loads, but BTC reduces ADC while IPC increases it, the systems can potentially work together in a way of maximizing the load reduction without reducing the pitch systems robustness.

1.3 Scientific contribution of this dissertation

This thesis desribes three years of research activity on load reduction techniques for multi-MW HAWT.

The first part of this dissertation describes new concepts for load mitigation, based on the deployment of distributed appended devices, mostly used in a passive way, attempting to exploit different tuning approaches, with the goal of demonstrating that passive means of actuation can lead to performance comparable to more complex active architectures. Extensive analyses are conducted in terms of fatigue and ultimate loads, and evaluating the effects on the AEP.

Two types of tuning for passive flaps and free pitching tips are identified as very effective for reducing both fatigue and ultimate loads: *inertial* and *aerodynamic* tuning. In both cases, the goal is to reduce loads with devices that are as simple as possible, and do not require sensors nor actuators, resulting in reliable and cheap solutions. They move in response to the structural accelerations and/or in response to the airloads. The modeling and the analysis are conducted preliminarily considering simple and fast simulation models, with the scope of assessing the feasibility of these solutions to mitigate loads. Then, more complex high-fidelity aeroelastic models in the multibody simulation environment are considered, using a large conceptual multi-MW wind turbine model as baseline.

To better understand the meaning of tuning a passive appended device, first of all the physical principle of the load reduction is discussed. The idea is that a passive blade device should be able to induce a change of aerodynamic loading distribution that counteracts the blade and/or tower oscillations. In the case of passive solutions, they are essentially mass-spring systems, and their response is purely driven by their aerodynamic and inertial characteristics, without the necessity for sensors/actuators. Clearly, this goes in the direction of a reduced complexity, which might be beneficial for limiting manufacturing, operation and maintenance costs. In principle, a passive response may be obtained by *inertial* or *aerodynamic* means, or a combination thereof. In the first case, the flap device does not respond to airload fluctuations, but to the structural accelerations inducing deformations. They can be either blade or tower tip accelerations. In the second case, the device responds to airload changes, including gust/turbulence fluctuations or deliberate change in angle ot attack and dynamic pressure. Considering either flap or pitching tip, the chord-wise position of the hinge line affects the aerodynamic response of the device, therefore the means of the passive response. In fact, if the hinge line lies close to the aerodynamic center, the aerodynamic moment about the hinge line varies little with respect to changes in the angle of attack. This way, the device is completely or relatively insensitive to aerodynamic load fluctuations. In this case, motion must

therefore be induced by using inertial loads. Tuning of the device is a matter of using offset masses in order to move the device center of gravity away from the hinge line, typically ahead, such that the device responds to the structural accelerations with a deflection that reduces the originating airloads. The advantage of this solution is that the device does not respond to deliberate changes in the operating condition and/or changes in angle of attack, as the ones induced by the wind turbine control system, while a possible drawback appears to be the modification of the overall blade mass distribution.

On the other hand, if the hinge line lies in front of the device aerodynamic center, its response is primarily driven by aerodynamic instead of inertial forces. In this case, changes in pressure distribution due to local angle of attack fluctuations produce changes in the aerodynamic moment about the hinge line, resulting in a device deflection that counteracts the originating disturbance. In this case, no added masses are tipically necessary, as a proper tuning is obtained by purely aerodynamic means. Note that, to achieve a pure aerodynamic tuning, offset masses may in case be necessary to move the center or gravity in the hinge line, thus avoiding any inertially-driven response.

The inertial tuning is illustrated by an implementation of a passive appended device on the 10 MW wind turbine model. In a nutshell, the main idea of the use one or more flaps at suitable locations along the blade span is that such devices move in response to the blade flapping or accelerations induced by the tower top motion in order to reduced it. This is obtained by offsetting a mass with respect to the flap hinge, so that when the blade deforms in one out-of-plain direction the flap automatically deflects such that the resulting change of camber induces a change in the pressure distribution that countereacts the blade deformation.

As this technology should work seamlessly with other standard technologies used on board wind turbines, the passive device concept developed here satisfies by design some additional requirements. First, since the presence of the device should not interfere with active full span blade pitching and should not cause a loss of the machine performances, it should not move in response to changes of angle of attack due to changes in pitch, but only to the blade/tower accelerations. This is obtained by aerodynamic balancing. Second, integration of the proposed device with a blade should not require a radical redesign of the blade and a drastic change in its manufacturing technology. This is obtained by using a standard trailing edge hinged flap, and by sizing the offset mass in such a way that its motion remains confined within the internal void that exists between the suction/pressure sides of the airfoil.

The aerodynamic tuning of the passive distributed device is exploited by an implementation of a pitching tip on the 10 MW wind turbine model. In this case, an aerodynamic tuning approach appears to be more suitable, since several factors make the inertial tuning difficult to implement. The main idea is that a change in the angle of attack, due to either gusts or blade flapping, induces a deflection of the device in order to reduces the airloads, therebay opposing the stress at the main spots. This is obtained by choosing the hinge location as a best compromise between the tendency to align with the wind of the passive device, which suggests a forward po-

sition, and a desire to limit inertial couplings, which suggests a hinge position close to its center of gravity. Furthermore, the spanwise extent of the tip has to be chosen as tradeoff between tip effectiveness and loading at the tip hinge. To avoid affecting power production, the mean misalignment of the tip with respect to the fixed part of the blade should be minimized in region II, where maximum rotor efficiency is necessary, and this is obtained by a scheduling mechanism of the hinge preload.

The second part of this dissertation is focused on the characterization of full-blade span passive solutions, with the goal of demonstrating via experiments the potential of passive means to mitigate the fatigue loads, withstand and sometimes are complementary to the active control solutions.

As previously stated, full blade span technologies are investigated in the literature, mostly in terms of individual pitch control and bend-twist coupling. The literature shows the effectiveness of these technologies in mitigating the wind turbine loads, also considering a synergy between them. Most of the research related to the bend-twist coupling of rotating blades focuses mainly on aero-elastic simulations, while literature reports experiments on the characterization of the BTC blades structural properties [33–35]. It appears that no experiments focused on the complete characterization of the bend-twist coupling were conducted prior to this work, as well as previous experimental activities related to the investigation of the synergy between active control laws and passive control techniques. It is therefore clear that there is need for further experimental investigations on this topic. To fullfill this lack in the literature, the best solution would be conducting testing activity in the field, but this usually presents some hurdles, since it is complicated to have full and accurate knowledge of the environmental conditions and, moreover, costs and times of testing are often very high. The use of scaled models helps overcome the aforementioned limitations, since the testing field would be the wind tunnel, where the environment is controllable with a high level of accuracy, and it is capable of supporting testing activities on scaled wind turbine models not only for the aerodynamics characterization, but also for the aero-servo-elasticity [36].

1.4 Thesis outline

This dissertation is divided in two parts to address the objectives previously described. The parts are further divided in three chapters and two chapters respectively. Concerning the first part, it describes means of load mitigation by blade distributed devices, as following:

- In Chapter 2 the passive actuation by inertial means is verified with a hybrid modeling: a complete 3D aeroservoelastic model of the DTU 10 MW Reference Wind Turbine (RWT), developed by Danmarks Tekniske Universitet (DTU) [37] is used for generating realistic operating conditions at a blade section, which are then in turn fed to a 2D typical section model of the airfoil equipped with the a passive flap. The stability of the system is studied and different scenarios under normal turbulent wind conditions and deterministic gusts over the entire operating range are considered to asses the load reduction capabilities of the passive solution.

- In Chapter 3 the 3D aeroelastic passive flap system is implemented in the high-fidelity multibody environment `Cp-lambda`, using the 10 MW RWT, with the scope of demonstrating the effectiveness of the system with more complex simulation models. In this case the passive flap effectively works on the wind turbine, and accounts for its complex geometry and largely non linear kinematics. More load cases are considered here, performing different types of DLCs, as requested by the certification standards [38, 39]. The most critical design loads cases are simulated, including possible device faults scenarios.

- In Chapter 4 a passive/free pitchable tip is investigated and compared with other proposed semi-passive and active solutions, in order to provide a general overview of the possible range of configurations and their respective performance. The passive solution is purely driven by the aerodynamic loads, since the inertial tuning is found to be not suitable for this specific implementation, as will be remarked in the chapter. The semi-passive coniguration adopts similar working principle to the passive case, but uses an active component to apply a varying restraining torque to limit mean tip deflections according to the machine operating condition. Finally, the active solution uses an actuator to drive the tip deflection based on a feedback control law. Each configuration is analyzed in detail, including the tuning of the proper parameters. Performances are assessed using the certification standards [38, 39] within a high-fidelity aeroservoelastic simulation environment `Cp-lambda`, upon the 10 MW RWT. Also in this case, possible fault scenarios are analyzed.

The second part is focused on the description of activities related to the demonstration via experiments of load mitigation by the full blade span passive solution as following:

- In Chapter 5, to allow the investigation on the bend-twist coupling solution via experiments, three blades featured with the BTC are realized and characterized in terms of structural properties. The designed blade represents an aeroelastic scaling of a multi-megawatt blade, in the the specific a loose-scaled representation of the NREL 5 MW RWT [40]. One blade is equipped with fiber bragg grating (FBG) sensors embedded inside the structure during the manufacturing process in order to evaluate potentialities of the Structural Health Monitoring (SHM) based on fiber optics, since the continuous increase of the wind turbine dimensions needs improvement of safety and reduction of the inspection time, achieved through load detection to the composite structure [42]. The structural characterization consists of blade modal analysis and static testing at bench. Then, an identification procedure is carried out to characterize the stiffness matrix and the mass distribution. The static tests are also used to calibrate the FBG sensors.

- Chapter 6 focuses on the description of wind tunnel activities for aerodynamic and load characterization of a scaled wind turbine model equipped with the BTC blades. The tests are executed in the wind tunnel of *Politecnico di Milano*, that is arranged in a vertical layout. At the bottom level, the aeronautical

section is used for the aerodynamic characterization of the rotor. It is featured of a low turbulence level and a wide flow velocity range. Several test points with different blade pitch angles and tip speed ratios are tested, previously selected with the help of `Cp-lambda` multibody simulation tool. This way the rotor power and thrust coefficients are characterized.

The boundary layer chamber at the top level of the wind tunnel has a wider cross area and length and it is used for the load characterization, since the wider cross-area allows to perform tests with low blockage effects, while scaled turbulent wind is introduced with the use of appropriate turbulence generators installed at the inlet of the chamber. The wider chamber dimensions allowed also to test different load scenarios, including partial wake conditions. For this reason, a wind turbine model equipped with rigid blades is installed ahead, used as a wake generator. Then, the model to be characterized is put downwind, and several partial wake conditons are tested, by placing the downwind model at different positions. All the tests are repeated three times:

1. the downwind model is equipped with rigid blades, in order to have the baseline for the load comparison;
2. the downwind model is equipped with aeroelastic blades with BTC, to characterize the loads of the passive solution and compare with baseline;
3. the downwind model with BTC is tested in synergy with the IPC, to verify the synergy of the integrated passive (BTC) / active (IPC) load reduction solutions.

Finally, conclusions and outlook for possible future developments on the topic are drawn in Chapter 7.

Part I

BLADE DISTRIBUTED SOLUTIONS

CHAPTER 2

Preliminary investigation of a distributed passive aeroelastic device

In this chapter[1] a preliminary investigation of a novel passive concept for the mitigation of loads on wind turbines is investigated. The device, which can be implemented as a flap or a pitching blade tip, moves passively in response to blade vibrations, opposing them, thereby yielding an attenuation of loads. In comparison to other architectures, such as active flaps, this solution has the advantage of not requiring sensors nor actuators, resulting in a particularly simple implementation, with potential benefits in manufacturing and maintenance costs, as well as in reliability and availability.

The chapter first describes the novel passive device in a nutshell, here implemented by means of a flap, highlighting its main characteristics. A proof of concept of the new idea is then given by a simulation study conducted with the combination of a sectional model of the flap and an aeroservoelastic multibody model of the rest of the machine. Results, obtained for a 10 MW wind turbine, indicate the ability of the passive flap in attenuating the blade flapping fluctuations in a significant frequency range, which in turn yield a reduced fatigue damage to the structure without noticeable effects in terms of power production.

The chapter is organized according to the following plan. At first, a simplified mathematical model is developed, to verify the feasibility of the proposed concept and to enable the assessment of its main key characteristics. The model considered here is of a hybrid nature: a complete 3D aeroservoelastic model of the wind turbine is used for generating realistic operating conditions at a blade section, which are

[1] This chapter is a revising of the journal paper "Load mitigation for wind turbines by a passive aeroelastic device"(see Ref. [21]).

then in turn fed to a 2D typical section model of the airfoil equipped with the passive flap. Next, the model is used for the tuning of the main design parameters of the new device. Simulations are then conducted with the goal of assessing the stability of the system, its load reduction capabilities in turbulent wind conditions and under deterministic gusts, as well as its effects on power output. Finally, conclusions are drawn and a plan for further developments is sketched.

2.1 Models and methods

The passive flap considered here is located at 75% span and moves freely and passively in response to blade vibrations, in turn modifying the aerodynamic force distribution around the blade span interval that it occupies, as shown in the picture.

The loosely-coupled hybrid model depicted in Figure 2.1 is used in this work. The model comprises a 3D aeroservoelastic model of the machine, implemented in the flexible multibody code `Cp-Lambda`, and a 2D typical section model. As shown in the picture, the 3D model is used for generating realistic inflow conditions at the blade section. When necessary, a loose coupling strategy is used to connect the 2D and 3D models, by transferring the sectional aerodynamic force perturbations generated by the use of the passive flap back onto the 3D model. A monolithic model of the machine equipped with the flaps is developed in Chapter 3. However, for the preliminary investigation of the passive flap concept that is the object of the present work, the simpler hybrid model was deemed sufficient. In addition, as shown later on, the 2D typical section model provides a wealth of information that is very useful for an initial understanding of the behavior of the system and its sizing.

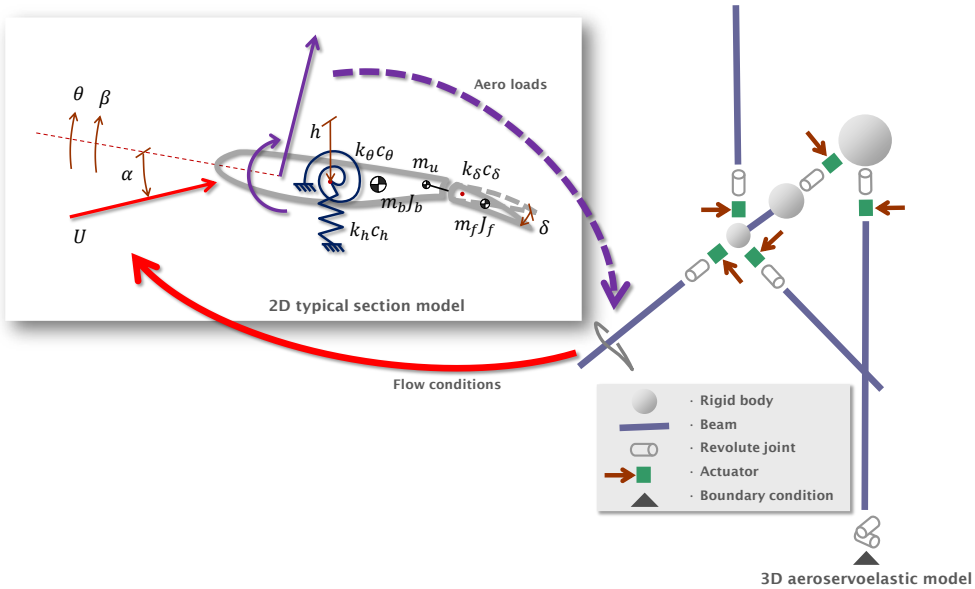

Figure 2.1: *Hybrid simulation model. At right, 3D aeroservoelastic multibody model of the wind turbine. At left, 2D typical section model with passive flap.*

2.1.1 3D aeroservoelastic model

The 3D aeroservoelastic model is based on a multibody formulation for flexible systems with general topologies. The modeling environment features a library of elements, which include rigid bodies, nonlinear flexible elements, joints, actuators and aerodynamic models. Sensor and control elements enable the implementation of generic control laws. The index-3 formulation is expressed in terms of Cartesian coordinates, while constraints are enforced by scaled Lagrange multipliers [44].

Rotor blades and tower are described by nonlinear geometrically exact shear and torsion deformable beam models, including off-diagonal stiffness couplings. Flexible components are discretized in space by the finite element method, leading to a system of differential algebraic equations in the time domain. Time integration is performed by a non-linearly unconditionally stable scheme that includes high frequency dissipation by energy decay [45].

The blade aerodynamic characteristics are defined by lifting lines, which include the spanwise chord and twist distributions as well as sectional aerodynamic coefficients, given in tabular form and parameterized in terms of the Reynolds number. The effects of the wake are modelled by a classical blade-element momentum (BEM) model based on annular stream tube theory with wake swirl and unsteady correction [46]. The aerodynamic description is completed by root and blade tip losses, unsteady aerodynamic corrections, dynamic stall, 3D blade root delayed stall and rotor-tower interference models. The wind field includes deterministic gusts and turbulent time histories, which may be obtained by the open-source software `TurbSim` [47].

The machine is governed over its entire operating range by controllers interfaced with the wind turbine model by external dynamic libraries. A supervisory unit manages the machine behavior by switching among different operating states and handling emergencies. The model is completed by a collective-pitch/torque controller, based here on a speed-scheduled linear quadratic regulator (LQR) [48], capable of controlling the machine over its entire operating envelope.

2.1.2 2D typical section model

The 2D sectional model is directly obtained from the modal condensation of the multibody model [17, 49], with the addition of a movable flap. This reduced order dynamical model has three degrees of freedom: the plunge motion h, which models the flapwise deflection of the blade, the torsional rotation θ about the elastic axis, and the flap deflection δ. The edge displacement is suppressed here since it is essentially due to the gravity effect that is not considered in this preliminary evaluation.

The plunge and twist degrees of freedom are associated with mass m_b, inertia J_b, stiffness k_h and k_θ, as well as damping c_h and c_θ, chosen so as to match the first flapwise and torsional mode frequencies and structural dampings of the rotor. Both the plunging and torsional stiffnesses depend on rotor speed, on account of centrifugal effects, i.e. $k = k_0 + k_\Omega \Omega^2$, where k_0 and k_Ω were tuned for each mode based on an eigenanalysis conducted with the 3D aeroelastic model.

The flap has a mass m_f and an inertia J_f. In addition, the flap has an offset mass

m_u, which is located forward of the flap and that moves within the void existing in that part of the blade between the suction and pressure sides of the airfoil, and backward of the aft shear web. The offset mass is subjected to accelerations when the blade bends, that in turn drive the deflection of the flap to which it is connected, thereby creating aerodynamic forces that countereact the blade bending itself. The maximum positive and negative flap deflections are limited by the thickness of the blade at the flap location, and by the position of the balancing offset mass. The flap is connected to the blade by a hinge, which features an internal rotational stiffness k_δ and damping c_δ. As for plunge and torsion, even the flap stiffness can be expressed as

$$k_\delta = k_{\delta_0} + k_{\delta_\Omega}\Omega^2, \tag{2.1}$$

where k_{δ_0} is the spring stiffness, while k_{δ_Ω} is due to centrifugal effects and it is negative when the flap mass lies between the elastic axis and the flap hinge, as in the present case. The hinge location is aft of the flap leading edge, in order to realize an aerodynamic balancing that reduces the sensitivity of the aerodynamic hinge moment to changes in the angle of attack.

The aerodynamic loads on the blade section are computed using classical unsteady strip theory under the hypotheses of inviscid and incompressible flow. Considering a small disturbance assumption, a closed form solution can be found in the frequency domain by the approach of Theodorsen [50, 51]. This classical approach is widely used to estimate the stability of the typical section. The resulting aeroelastic system writes

$$\left(\mathbf{M}_S\, s^2 + \mathbf{C}_S\, s + \mathbf{K}_S\right) \begin{Bmatrix} h(s)/b \\ \theta(s) \\ \delta(s) \end{Bmatrix} = q\mathbf{A}^{AE}(s') \begin{Bmatrix} h(s)/b \\ \theta(s) \\ \delta(s) \end{Bmatrix}, \tag{2.2}$$

where $\mathbf{M}_S$, $\mathbf{C}_S$ and $\mathbf{K}_S$ represent the structural mass, damping and stiffness matrices, respectively. The right hand side represents the aerodynamic forces and moments, where q is the dynamic pressure. $\mathbf{A}^{AE}$ is the matrix of aerodynamic coefficients expressed as:

$$\mathbf{A}^{AE}(s') = 2b^2\left(\mathbf{M}^{NC}s'^2 + \left(\mathbf{C}^{NC} + C(s')\,\mathbf{r}_1\mathbf{s}_2^T\right)s' + \mathbf{K}^{NC} + C(s')\,\mathbf{r}_1\mathbf{s}_1^T\right), \tag{2.3}$$

where $\mathbf{M}^{NC}$, $\mathbf{C}^{NC}$, $\mathbf{K}^{NC}$ are the non-circulatory mass, damping and stiffness matrices, respectively, b is the reference semi-chord length. Products $\mathbf{r}_1\mathbf{s}_2^T$ and $\mathbf{r}_1\mathbf{s}_1^T$ define the circulatory terms, where $\mathbf{r}_1$, $\mathbf{s}_1$ and $\mathbf{s}_2$ are 3×1 column vectors of coefficients. The complex Theodorsen lift-deficiency function is noted $C(s')$, where the reduced frequency is $s' = sb/U$, U being the flow speed.

To handle arbitrary motions, a time domain model is also considered in this work. This form of the model provides for a state-space representation of the system by using Duhamel's integral of Wagner indicial step response, leading to a linear time invariant (LTI) model that can be readily analyzed using LTI system theory [52]. The aeroelastic model writes in this case

$$\begin{aligned}\mathbf{M}_S \begin{Bmatrix} \ddot{h}(t)/b \\ \ddot{\theta}(t) \\ \ddot{\delta}(t) \end{Bmatrix} + \mathbf{C}_S \begin{Bmatrix} \dot{h}(t)/b \\ \dot{\theta}(t) \\ \dot{\delta}(t) \end{Bmatrix} + \mathbf{K}_S \begin{Bmatrix} h(t)/b \\ \theta(t) \\ \delta(t) \end{Bmatrix} = \\ = 2qb^2 \begin{Bmatrix} -C_L^{NC} - C_L^C - C_L^G \\ C_M^{NC} + C_M^C + C_M^G \\ C_H^{NC} + C_H^C + C_H^G \end{Bmatrix},\end{aligned} \tag{2.4}$$

where $(\cdot)^{NC}$ identifies non-circulatory terms, $(\cdot)^C$ refers to the circulatory ones, while $(\cdot)^G$ indicates terms related to the turbulent flow fluctuations. The non-circulatory terms written in matrix form correspond to the non-circulatory terms in matrix $\mathbf{A}$ of Equation (2.2). On the other hand, the circulatory terms are defined as:

$$C_L^C = C_{L_{/\alpha}} \alpha^C + C_{L_{/\delta}} \delta^C, \tag{2.5a}$$

$$C_M^C = \left(a + \frac{1}{2}\right) C_L^C, \tag{2.5b}$$

$$C_H^C = C_{H_{/\alpha}} \alpha^C + C_{H_{/\delta}} \delta^C, \tag{2.5c}$$

where a is the non-dimensional distance between the elastic axis and the section mid chord, whereas $C_{L/*}$ and $C_{H/*}$ represent the partial derivatives of the lift and hinge moment coefficients with respect to the generic parameter $*$, i.e. the angle of attack α or the flap deflection δ. The circulatory angles α^C and δ^C are computed as:

$$\alpha^C = \alpha_{QS}(0)\,\varphi(\tau) + \int_0^\tau \frac{\mathrm{d}\alpha_{QS}(\sigma)}{\mathrm{d}\sigma} \varphi(\tau - \sigma)\,\mathrm{d}\sigma, \tag{2.6a}$$

$$\delta^C = \delta_{QS}(0)\,\varphi(\tau) + \int_0^\tau \frac{\mathrm{d}\delta_{QS}(\sigma)}{\mathrm{d}\sigma} \varphi(\tau - \sigma)\,\mathrm{d}\sigma, \tag{2.6b}$$

where $\tau = tU/b$ is the traveled distance expressed in semi-chord lengths b. Function $\varphi(\cdot)$ is the Jones approximation of Wagner function [52], while the quasi-steady $(\cdot)_{QS}$ angles are given by

$$\alpha_{QS} = U\theta + \frac{\dot{h}}{b} + b\left(\frac{1}{2} - e\right)\dot{\theta}, \tag{2.7a}$$

$$\delta_{QS} = \frac{U}{\pi}(T_{10} - lT_{21})\,\delta + \frac{b}{2\pi}(T_{11} - 2lT_{10})\,\dot{\delta}. \tag{2.7b}$$

Coefficients T_{ij} depend on the geometrical configuration of the flap [51], while e is the distance between flap hinge and mid chord point, and l the one from flap hinge to the airfoil trailing edge. The lift and pitch moment coefficients are defined as:

$$C_L^G = C_{L_{/\alpha}} \alpha^G, \tag{2.8a}$$

$$C_M^G = \left(a + \frac{1}{2}\right) C_L^G. \tag{2.8b}$$

The angle of attack α^G is obtained as the solution of Küssner problem for an arbitrary vertical gust profile, which gives [52]:

$$\alpha^G = \alpha^G(0)\,\psi(\tau) + \int_0^\tau \frac{\mathrm{d}\alpha(\sigma)}{\mathrm{d}\sigma}\psi\ (\tau-\sigma)\,\mathrm{d}\sigma, \tag{2.9}$$

where $\psi(\cdot)$ is the exponential approximation of Küssner function. The hinge moment coefficient generated by a vertical gust profile has the following expression:

$$C_H^G(\tau) = \frac{1}{2qb^2}\int_b e^b \Delta\bar{p}_a(x) e^{ik\tau}\,(x-be)\,\mathrm{d}x, \tag{2.10}$$

where $\Delta\bar{p}_a(x)$ is Schwarz complex solution [49]. The expression for C_H^G given by Equation (2.10) does not lead to a state space form of the model governing equations. To correct for this, [53] proposed to assume the upwash caused by the gust as constant over the section, which means that the circulatory contribution caused by the sectional motion is the same as the one due to the gust, an assumption that is acceptable for reduced frequencies $s' \ll 1$. This way, $\tilde{\alpha}^G$ can be expressed as

$$\tilde{\alpha}^G = \tilde{\alpha}^G(0)\,\phi(\tau) + \int_0^\tau \frac{\mathrm{d}\alpha(\sigma)}{\mathrm{d}\sigma}\phi(\tau-\sigma)\,\mathrm{d}\sigma \approx \alpha^G, \tag{2.11}$$

which gives:

$$C_H^G = C_{H_{/\alpha}}\tilde{\alpha}^G. \tag{2.12}$$

Finally, Duhamel integrals are solved by state space realization.

The resulting system model can be expressed in LTI form as

$$\dot{\mathbf{x}} = \mathbf{A}\mathbf{x} + \mathbf{B}\mathbf{u}. \tag{2.13}$$

The state vector is noted $\mathbf{x}$, and contains both structural and aerodynamic states. The structural degrees of freedom include the plunge displacement, the torsional rotation and the flap deflection, together with their respective time rates. The aerodynamic states are related to the indicial response, including the approximation of the Wagner function and the one of the Küssner function for unsteady loads. The input vector $\mathbf{u}$ contains the turbulent fluctuations of the angle of attack and the collective-pitch control input.

2.2 Flap sizing, results and discussion

The proposed passive flap concept was applied to the 10 MW RWT, which represents a significant example of the next generation very large HAWTs. The DTU 10 MW RWT is a conceptual machine developed by Danmarks Tekniske Universitet (DTU), freely availably in the public domain for research purposes [54]. The main characteristics of the wind turbine are reported in Table 2.1, while a more complete description of the model is given by [55].

In the following, the flap is sized and its main performance characteristics are evaluated by means of numerical simulations. At first, we consider the problem of aerodynamic balancing, which leads to a choice for the hinge location. Next, the

Table 2.1: *Main parameters of the DTU 10 MW RWT.*

Parameter	Value
Rotor diameter	178.3 m
Hub height	119.0 m
Wind class	IEC 1A
Rated power	10 MW
Cut-in wind speed	4 m/s
Cut-out wind speed	25 m/s

flap is optimized in order to yield the best possible alleviation of fatigue damage, while ensuring a stable response throughout the entire operating envelope of the machine. A transfer function analysis is then used to illustrate the notch filtering action realized by the flap on angle of attack fluctuations in the frequency band that is most responsible for the generation of fatigue damage. The study is concluded by verifying that passive flaps do not affect in a noticeable manner the power production of the machine, nor increase the ultimate loads encountered in emergency shutdown conditions.

2.2.1 Aerodynamic balancing and mitigation of speed dependency

Aerodynamic balancing refers to the reduction of the effects of changes in angle of attack on hinge moments, which are captured by the $C^C_{H_{/\alpha}}$ derivative. A small (ideally null) value of this derivative helps reducing the interaction between the passive device and the active pitch control system of the wind turbine. Indeed, the passive flap should not contrast the activity of the pitch controller, but should only react to changes in angle of attack due to blade vibrations. An aerodynamically balanced flap effectively decouples the flap motion and blade pitch, achieving the desired independence of the passive and deliberate active responses.

Aerodynamic derivatives are estimated here by thin airfoil theory, as described in [51], which allows for the evaluation of the aerodynamic coefficients by analytical expressions. In reality, the aerodynamic derivatives of the flap are also influenced by the local shape and gap between airfoil and flap, as well by fluid viscosity. For these reasons, the results provided by thin airfoil theory can be considered only as approximate estimates, which are nonetheless sufficient for the scopes of the present study.

A balanced flap can be typically obtained by displacing the hinge location aft of the flap leading edge. To find the balancing condition, consider the quasi-steady flap terms in Equation (2.3), which read $C^C_{H_{/\alpha}} = \frac{1}{2} r_{13} s_{12}$. Balancing may be obtained by setting $r_{13} = 0$, which corresponds to an appropriate choice of the overhang, defined as the surplus part of the flap ahead of the hinge divided by the flap chord.

Sizing of the device should also consider that the effective aeroelastic stiffness of the flap depends on flow speed. This is in general an undesirable effect because it tends to detune the flap, thereby reducing its efficacy in certain operating ranges, and it may possibly also affect its stability. In fact, from Equation (2.2), the aeroelastic

flap stiffness k_δ^{AS} can be written as

$$k_\delta^{AS} = k_\delta - \frac{1}{2}\rho U^2 c^2 \left(C_{H_{/\delta}}^{NC} + C(s') C_{H_{/\delta}}^{C} \right), \tag{2.14}$$

where ρ is the air density. This expression shows how the aeroelastic stiffness depends on flow speed through terms $C_{H_{/\delta}}^{NC} = \frac{1}{2} K_{33}^{NC}$ and $C_{H_{/\delta}}^{C} = \frac{1}{2} r_{13} s_{13}$. While the latter term is null for a balanced flap, i.e. when the balancing condition $r_{13} = 0$ is satisfied, the former could also be rendered equal to zero by an appropriate sizing. A better approach, however, is to use it for compensating the centrifugal stiffening term in k_δ (cf. Equation (2.1)), which, depending on rotor speed, is also related to sectional speed.

Figure 2.2 shows the non-circulatory term $C_{H_{/\delta}}^{NC}$ as a function of the overhang, for a flap chord equal to 10% of the sectional chord. By examining the plot, it appears that an overhang equal to 32% makes the non-circulatory term equal to zero, while larger values (corresponding to positive values of this aerodynamic derivative) can be chosen to compensate the (negative) centrifugal stiffening effects.

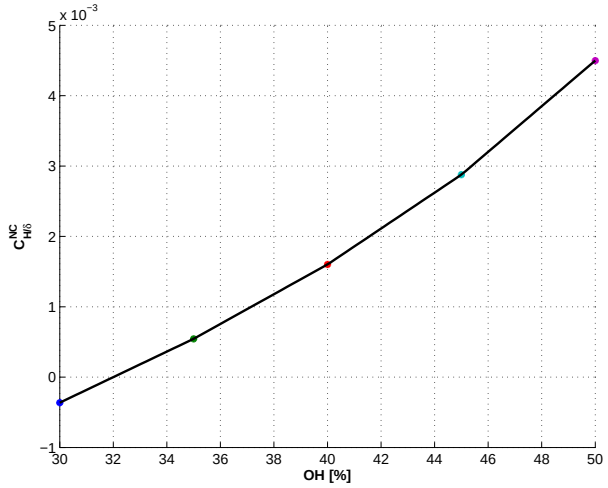

Figure 2.2: *Non-circulatory component of hinge moment derivative $C_{H_{/\delta}}^{NC}$ as a function of overhang OH, expressed as a percentage of flap chord.*

In order to verify the effect of balancing in its ability not to affect changes in angle of attack due to pitching, the plunge and torsional degrees of freedom of the 2D typical section model were frozen, while the flapped airfoil was subjected to turbulent wind fluctuations. Figure 2.3 shows the time histories of lift (at top) and flap deflections (at bottom) for two mean wind speeds. The bottom plots show that the flap deflection is very small, as hinge moments are nearly insensitive to changes in angle of attack. For this reason, the lift plots for the cases with and without flap are nearly identical, indicating that the flap generates negligible aerodynamic forces by its negligible deflection.

These results confirm that, when the blade is not vibrating, the flap essentially does not move even if the flow is fluctuating. On the other hand, when the blade vibrates, accelerations transmitted to the balancing mass are responsible for making the flap respond.

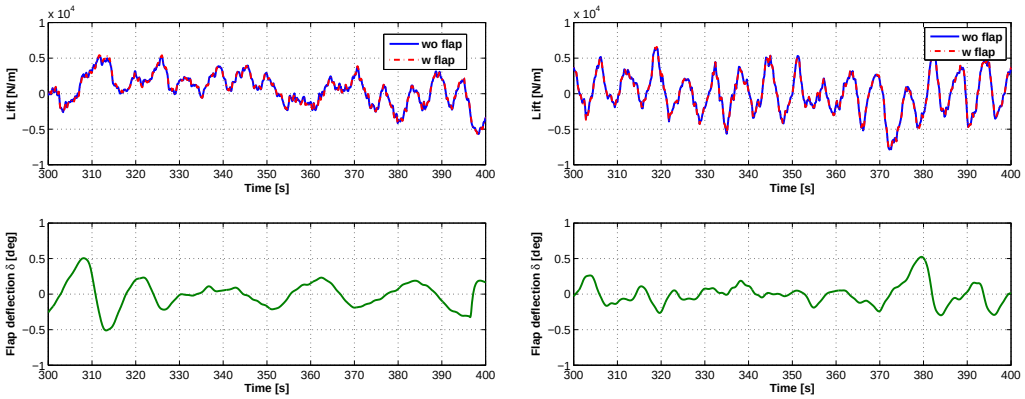

Figure 2.3: *Lift (top) and flap deflection (bottom) vs. time at hub-height wind speed of 13 m/s and 25 m/s, while freezing the plunge and twist degrees of freedom.*

2.2.2 DEL-based sizing

The span-wise position of the passive flap is placed in this study at 75% of blade length. Although this could be further optimized, this location offers a reasonable compromise in terms of effectiveness on the control of the first blade modal shape, while still offering a not too small chord length and sectional thickness. In fact, the thickness of the section limits the possible excursion of the balancing mass, thereby limiting the flap motion and authority. Some relevant blade and sectional parameters are reported in Table 2.2 [56].

Table 2.2: *Blade and sectional parameters for the DTU 10 MW RTW. Sectional data correspond to 75% span.*

Parameter	Value
Chord	3.25 m
Plunge frequency	0.62 Hz
Torsional frequency	4.99 Hz
Plunge damping factor	0.01
Torsional damping factor	0.01
Sectional specific mass)	186 Kg/m
Sectional specific moment of inertia	94.1 Kg m^2/m
Elastic Axis (EA) position from leading edge	35% blade chord
Center of gravity position behind the EA	6.25% blade chord

As the main goal of the passive flap is the reduction of fatigue loading, fatigue was used as the principal metric driving the sizing of the device. Fatigue is here measured in terms of lifetime damage equivalent loads (DEL). The DEL of the plunge displacement of the typical section is considered as an indicator of the flapping motion of the entire blade, and hence of the associated root bending moment. According to this model, a reduction of the plunge DEL of the typical section is interpreted as an increase in the fatigue life of the blade.

DELs are estimated on the 2D typical section model, under flow conditions computed on the 3D closed-loop aeroservoelastic model. The 2D model therefore feels

the effects of flow fluctuations due to vertical wind shear, turbulence and pitch activity. Notice that this is a conservative estimation of DEL, as in reality the typical section would feel reduced flow fluctuations resulting from its reduced oscillations by the flap smoothing of the airloads. Simulations are conducted at different wind speeds in order to cover the entire operating range of the machine, and for multiple realizations of the turbulent wind field, as prescribed by certification guidelines [38, 39]. Lifetime DELs are then obtained by weighting with a Weibull probability function [46].

To identify the best passive flap configuration, DELs are computed for varying values of the flap frequency, damping and chord length. The fraction of sectional chord occupied by the flap clearly plays an important role. In fact, reducing the chord occupation reduces the effectiveness of the flap. At the same time, its maximum allowable excursion is also limited, as the airfoil is thinner towards its trailing edge. On the other hand, too large a flap should be avoided as the balancing mass would start interfering with the aft shear web of the blade. Analyzing the various requirements and the results of simulations, a good compromise was found for a flap chord equal to 16% of the sectional chord, with a distance of the offset mass from the hinge axis equal to 32% of the sectional chord.

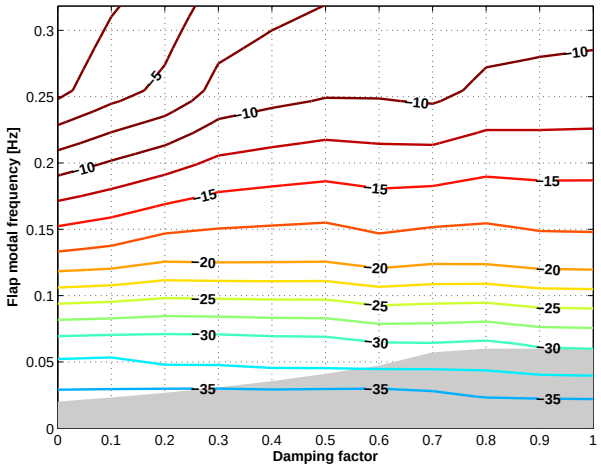

Figure 2.4: *Lifetime DEL percent reduction with respect to the baseline unflapped blade, as a function of flap frequency and damping. The shaded area represents unstable configurations.*

Figure 2.4 reports the iso-contours of the DEL percent reduction with respect to the baseline unflapped blade, computed as previously explained, as a function of flap frequency and damping. Looking at the plot, it appears that low flap modal frequencies are associated with larger DEL reductions. The reason for this behavior will become clear in the response function analysis conducted later on. However, stability limits the flap frequency from below, as shown by the shaded area in the graph that indicates unstable combinations of parameters. A reasonable choice appears to be a modal frequency equal to 0.032 Hz, which corresponds to a DEL reduction of 35%. The figure shows that iso-contour lines in that region of the plot are essentially unaffected by the damping factor. At the light of this consideration, the flap is realized without a hinge damper, which also helps keep the solution away

from the stability limit. A value of the damping factor equal to 0.1 was used in the numerical simulations, to account for the possible presence of friction in the rotation mechanism; however, the plot shows that results are very robust to this possibly uncertain parameter. Values of the flap parameters corresponding to these choices are reported in Table 2.3.

Table 2.3: *DEL-optimized parameters of the passive flap.*

Parameter	Value
Chord	0.51 m
Modal frequency	0.032 Hz
Damping factor	0
Sectional specific mass	5.6 Kg/m
CG position in front of the hinge	16% blade chord
Sectional specific moment of inertia	4.19 Kgm
Overhang	31.9% flap chord
Flap free-play range	-22.5 deg < δ < 15.1 deg

2.2.3 Stability analysis

Figure 2.5 shows the V-g [57], or speed-damping, diagram for a range of hub-height wind speeds from cut-in to cut-out. The solutions corresponding to the passive flap case are reported using solid lines, while the ones without flap by dash-dotted lines. Using the V-g method, a structural damping term g is added in order to bring each mode to the verge of flutter, i.e. to a purely periodic response. For each considered speed, if the resulting g is smaller than the actual structural damping, then the system is stable. The plot shows that the flapped typical section is flutter-free in its entire range of operating conditions, as g is always largely negative.

It appears that the addition of the flap has very limited effects on the torsional mode. On the other hand, the damping of the plunge mode is somewhat affected, but without creating any stability problem. The flap mode is also well damped throughout the entire operating range. This is largely due to the mitigation of speed dependency of the aerodynamic derivatives of the model achieved through aerodynamic balancing and flap sizing, as explained earlier on.

Figure 2.5 shows at right the system modal frequencies as functions of rotor speed, the plot showing the typical effects of centrifugal stiffening. Here again frequencies are well separated and coalescence of the plunging and torsional modes is far outside of the operating conditions. The frequency of the flap mode is essentially constant, and this is again due to aerodynamic balancing and its effects on the mitigation of the dependency of the model coefficients on flow speed.

2.2.4 Transfer functions analysis

To better understand the effects of the passive flap on the response of the system, the transfer functions of the three degrees of freedom of the flapped typical section are computed next, using the state space model.

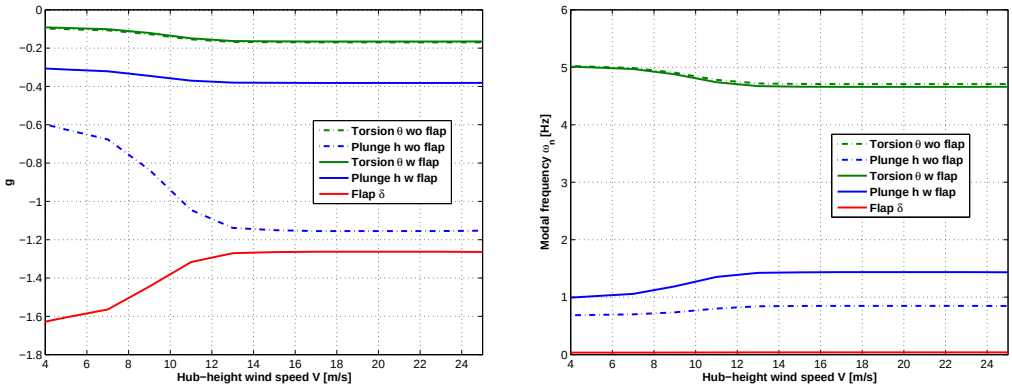

Figure 2.5: *Stability and frequency analysis of the flapped typical section.*

Figure 2.6 shows the transfer functions from angle of attack to plunge, torsion and flap deflection. The transfer functions of the system with passive flap are reported by solid lines, while the case without flap is represented by dash-dotted lines. The plot corresponds to operation at rated wind speed.

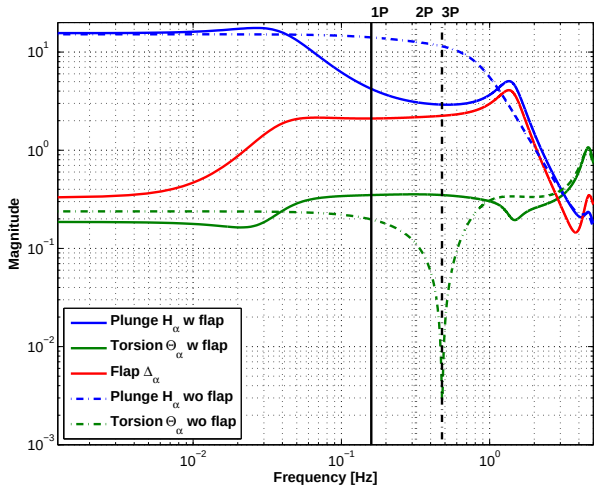

Figure 2.6: *Transfer functions between angle of attack and plunge, torsion and flap deflection for operation at rated wind speed.*

Examining the plunge transfer function, there is a strong reduction in magnitude around the band 1xRev-3xRev when the passive device is used. This transfer function presents two peaks: a mild one in correspondence of the frequency of the flap near 0.03 Hz, and one at the new plunge frequency around 1.5 Hz, which is higher than in the case without flap, as already shown by Figure 2.5.

The flap transfer function is essentially null below the flap natural frequency. This is obtained by design, and it is due to the use of aerodynamic balancing. On the other hand, the flap responds at higher frequencies up to the plunge one, after which its contribution quickly dies off. These results show that the passive flap effectively behaves as a notch filter for the plunge load in the 1xRev-3xRev band, while the torsional motion remains largely unaffected by the presence of the flap.

Figure 2.7 shows at left the transfer function from angle of attack to plunge for varying wind speed for the case without flap, while at right refers to the passive flap case. Here again it appears that the passive flap is capable of creating a very noticeable attenuation in the 1xRev-3xRev band, which remains remarkably constant throughout the entire range of operating wind speeds of interest.

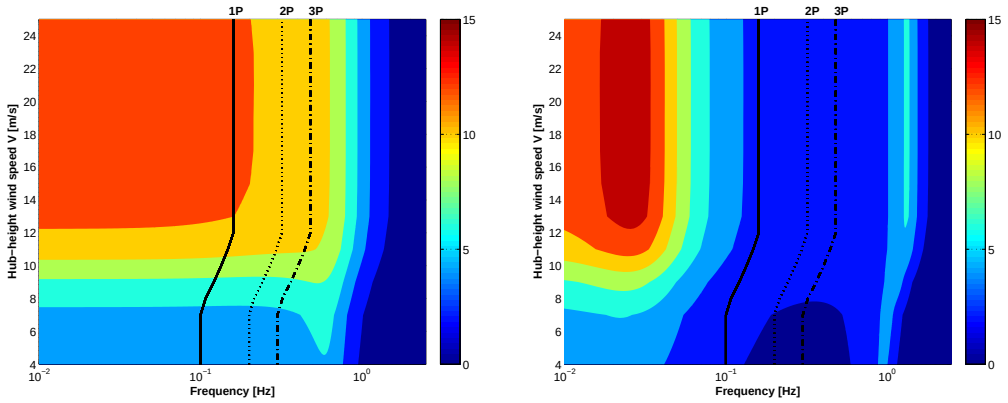

Figure 2.7: *Transfer functions from angle of attack to plunge motion, as functions of hub-height wind speed. Unflapped (left) and flapped (right) baseline configuration.*

The attenuation exhibited by the passive flap in the 1xRev-3xRev band is crucial for the reduction of fatigue loading on the wind turbine. In fact, fatigue is primarily generated in this range of frequencies, and not much of it is caused by fluctuations above the 3xRev. This is shown by Figure 2.8, which reports the normalized blade root lifetime DEL bending moment as a function of load harmonics, as computed for the baseline RWT without passive flap by using the 3D aeroservoleastic model. It appears that DEL increases very rapidly with frequency, to the point that already 75% of damage is accumulated for frequencies up to 1xRev, and then levels off, with very little contributions coming from frequencies above the 3xRev.

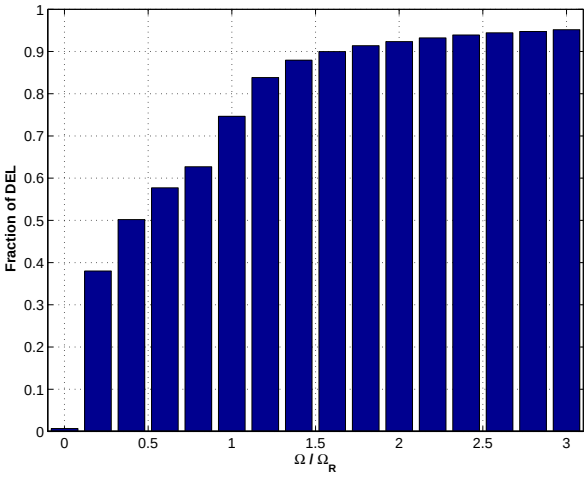

Figure 2.8: *Normalized blade root lifetime DEL bending moment, plotted as a function of load frequency.*

2.2.5 Turbulent wind simulations and fatigue

The effectiveness of the passive flap concept is then evaluated by means of time domain simulations in turbulent wind conditions. The 3D aeroservoelastic model provides the angle of attack time histories that are used for feeding the 2D typical section model, realizing a one-way coupling between the two models. Athough the one-way coupling might seem a limit of the presented method, it produces an overestimation of the aerodynamic loads, since the angle of attack provided to the 2D sectional model includes plunge and torsion contribute of the blade from 3D aeroservoelastic model not equipped with passive flap, which in turn would reduced the plunge motion and therefore the angle of attack fluctuations provided. Figures 2.9 through 2.11 report results obtained for wind speeds of 5 m/s (close to cut-in), 13 m/s (rated) and 25 m/s (cut-out).

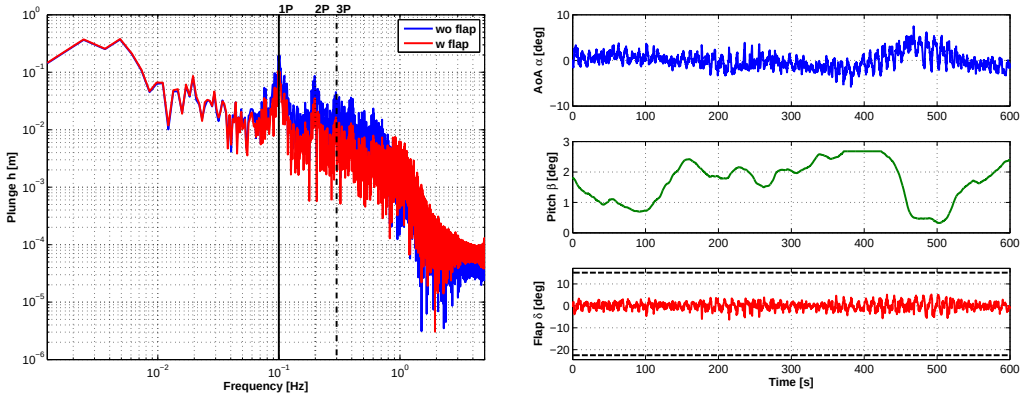

Figure 2.9: *System response around 5 m/s (cut-in). Plunge response spectrum (left) and time histories (right).*

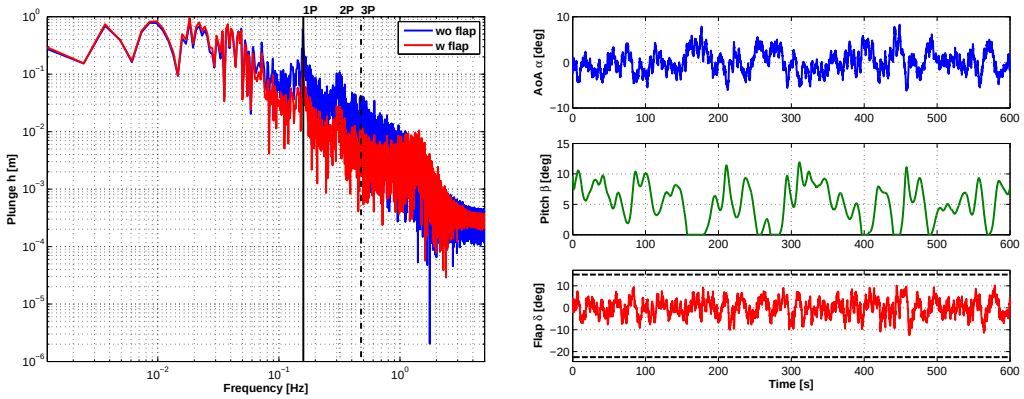

Figure 2.10: *System response around 13 m/s (rated). Plunge response spectrum (left) and time histories (right).*

Figures 2.9, 2.10 and 2.11 report at left the spectrum of the plunge response with and without passive flap. The peaks at the 1, 2 and 3xRev are very noticeable, as expected. In all cases, peaks are very significantly reduced by the passive flap in the 1xRev-3xRev band.

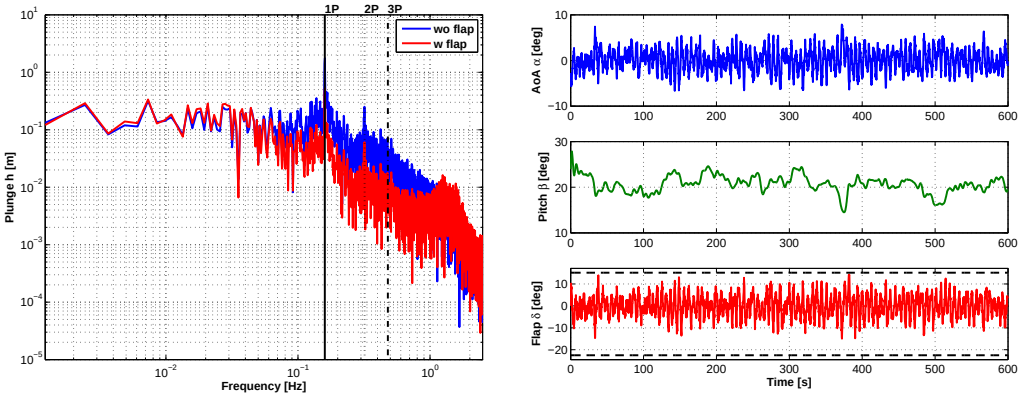

Figure 2.11: *System response around 25 m/s (cut-out). Plunge response spectrum (left) and time histories (right).*

Figures 2.9, 2.10 and 2.11 report at right, from top to bottom, the time histories of the angle of attack, pitch angle and flap deflection. The pitch activity differs significantly in the various plots, on account of the difference in control strategy that is used for regulating the machine throughout different ranges of wind speeds. The flap deflection plots report with black dashed lines the limits of allowable flap deflections, which are constrained by the fact that the balancing mass is restricted to move within the pressure and suction sides of the airfoil. It appears that the maximum allowable excursions are achieved only very seldom and exclusively for the highest wind speed conditions, confirming the correct sizing of the device even from this point of view.

Fatigue damage, as captured by DELs of the typical section plunging motion, is shown in Figure 2.12 for varying wind speeds.

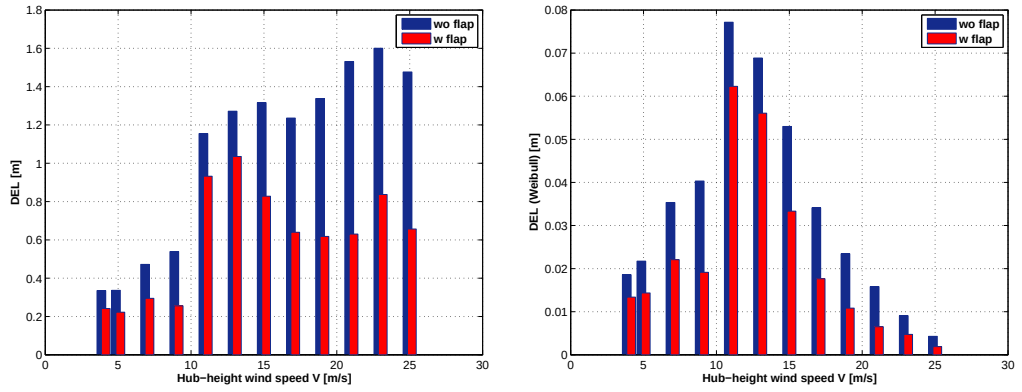

Figure 2.12: *DELs of the typical section plunging motion, with and without passive flap. Blade DELs vs. wind speed. Without Weibull weight at left, with Weibull weight at right.*

The results for the configuration without flap are reported by blue bars, while red bars are used for the rotor equipped with the passive flap. Figure 2.12 reports at left DELs accumulated at each single wind speed. It appears that DELs are particularly high around rated and cut-out, wind speed ranges where the largest loads typically occur. This figure shows in particular how the flap is effective at all

wind speeds. A different view is offered by Figure 2.12 at right, which reports DELs weighted by the Weibull wind probability. The figure shows that the most significant contributions to DELs come from the wind speed range around rated. Summing up over the complete wind range gives the lifetime DEL, which was previously shown in Figure 2.4. All plots confirm the very significant attenuation of DELs given by the use of the passive flap.

2.2.6 Effects on power production

The effects on power production are estimated by the closed loop loosely coupled hybrid model described earlier on. The aerodynamic force time histories generated by the 2D sectional model at each time instant are applied back onto the 3D aeroservoelastic model as perturbations of torque. These perturbations are evaluated along a span portion between 70% and 80% of the blade length, where the flap is supposed to be placed. Simulations are conducted in NTM wind conditions for different values of mean wind speed covering the entire wind speed range. Results are shown in Figure 2.13, which reports the mean value of the electrical power vs. mean hub-height wind speed. The plot shows a very limited effect of the use of the passive flap on power production.

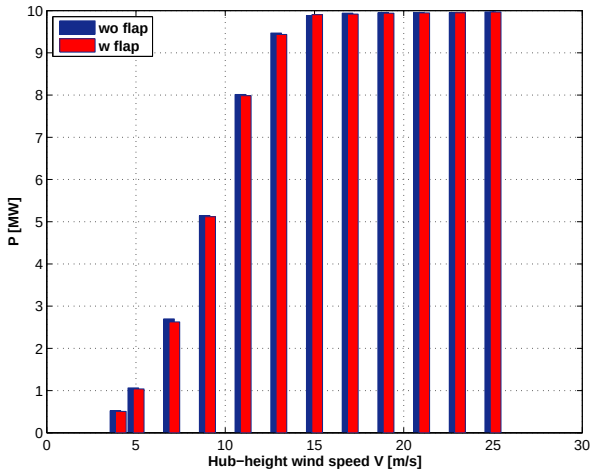

Figure 2.13: *Power production in turbulent condition for varying mean wind, with and without passive flap.*

Weighting the results of Figure 2.13 with the Weibull distribution, yields the annual energy production (AEP). The use of the flap incurs in a reduction in AEP of 0.33% with respect to the baseline unflapped case, which is a modest and acceptable amount.

2.2.7 Ultimate load analysis

Ultimate loads are often generated during emergency shutdowns when, during a strong gust and concomitant loss of connection to the grid, the machine enters into a rapid aerodynamic braking of the rotor by pitching the blades to feather (cf. DLC 2.3 of [39]). This violent maneuver not only rapidly slows down the rotor, but also

makes the machine spring forward, due to the sudden drop and reversal of thrust. Given the fact that the loads generated during these maneuvers are often design drivers, it is important to verify that the use of the passive flap does not increase such ultimate loads.

Figure 2.14 shows the results for an emergency shutdown conducted following a deterministic gust at cut-out, with grid loss at the point of maximum gust peak.

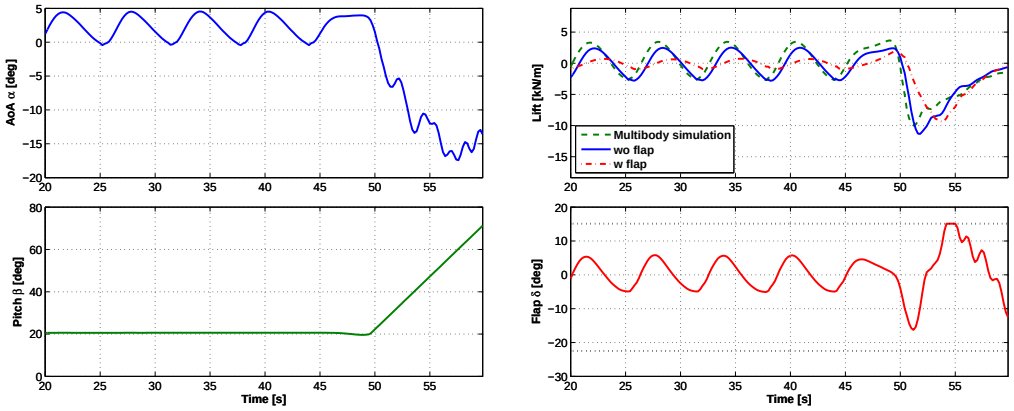

Figure 2.14: *Emergency shutdown following an extreme operating gust with concomitant grid loss at cut-out wind speed. Angle of attack and pitch time histories at left, lift and flap deflection time histories at right.*

Figure 2.14 reports at left the time histories of the angle of attack at the blade section (top) and the blade pitch (bottom). The second plot clearly shows the rapid pitch to feather of the blade commanded by the control system in order to rapidly slow down the rotor.

The top part of right figure compares the lift time history for the 3D multibody simulation of the baseline unflapped rotor (green dashed line), the 2D sectional model without flap (blue solid line), and the 2D sectional model with flap (red dash-dotted line). There is a good matching between the multibody model and the sectional model without flap, which supports the validity of the loose coupling strategy. The load peak, which is achieved during the first swing forward oscillation of the machine, is a little more pronounced and slightly delayed for the sectional model. On the other hand, the response of the flapped section is much smoother because of the load mitigating action of the device, which drastically reduces the prominent 1xRev oscillation visible in the unflapped case. The load peak is also smaller and delayed. The bottom part of the figure plots the time history of the flap deflection, showing that the flap hits the limits of its allowed free deflection during the maneuver. Suitable end stops will have to be designed, in order to cope with the reaching of limit flap excursions in these extreme conditions.

For all possible combinations of gust and grid loss time [39], Figure 2.15 shows the plunge peak for the unflapped and flapped cases. Here again, as in the case of the fatigue analysis, plunge motion is assumed to be well correlated with loads, and it is therefore used as the relevant metric for this analysis. Looking at the results, it appears that even in this case, although this is not its primary goal, the passive device realizes some reductions in the loads.

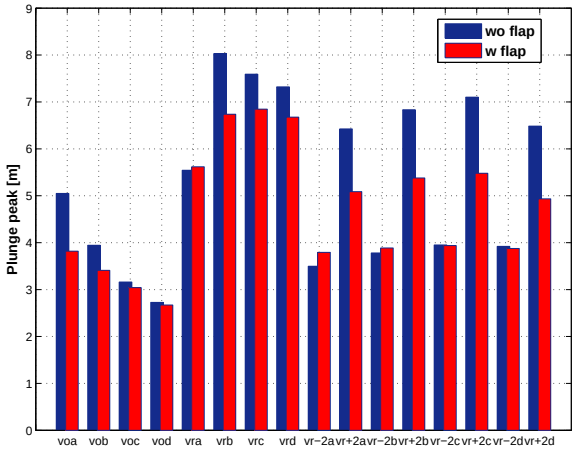

Figure 2.15: *Ultimate (plunge) peaks for extreme operating gust with concomitant electrical loss, DLC 2.3, for the flapped and unflapped cases.*

2.3 Synopsis

In this chapter a preliminary investigation of passive distributed device for wind turbine load mitigation is investigated by a passive flap concept. The model considered here is of a hybrid nature: a complete 3D aeroservoelastic model of the 10 MW machine is used for generating realistic operating conditions at a blade section, which are then in turn fed to a 2D typical section model of the airfoil equipped with the passive flap. The results obtained so far seem to indicate that the proposed concept has some interesting potential:

- The optimal flap parameters are very reasonable, and do not require excessive size nor masses.
- Fatigue load alleviation is very noticeable, and accompanied only by modest AEP reductions
- The behavior is robust and consistent within the entire operating regime of the wind turbine, without necessitating of scheduling of system parameters with respect to wind speed or other quantities. To this end, an instrumental role was played by a sizing of the flap that performs an approximate cancellation of the effects due to centrifugal forces and non-circulatory aerodynamics.
- The solution is compatible with standard active blade pitch control strategies, routinely adopted on board modern wind turbines. In fact, differently from other passive flap concepts, the present device does not respond to deliberate changes in angle of attack due to active blade pitching.
- The flap concept appears to be applicable without the need for radical changes in the design of blades (although, to fully exploit the benefits of the passive device, it is expected that a passive-flap-equipped blade will have to be redesigned, for example by increasing its span, reducing its weight, or resizing some of its components).

- There is the potential also for the reduction of ultimate stresses during violent transients, as in emergency shutdown procedures.

The continuation of this study is described in the next chapter, with the implementation of the passive flap model in the 3D aeroservoelastic environment. In that case, a more comprehensive load analysis is performed, including the effect of turbulence by considering multiple seeds.

CHAPTER 3

3D aeroelastic model of a passive flap for wind turbine load alleviation

This chapter describes the 3D aeroelastic implementation of the passive flap system in the high-fidelity multibody environment `Cp-lambda`, with the scope of demonstrating the potentiality of this passive means in reducing the loads with a more reliable simulation tool. In this case the passive flap effectively works on the wind turbine, and accounts for its complex geometry and largely non linear kinematics. Inertial loads are included, i. e. gravity and centrifugal effects, the former not included in the preliminary investigation discussed in Chapter 2. Multiple scenarios and load cases are considered as required by the certification standards [38, 39] to characterize the loads. The most critical design load cases are analyzed, including possible device faults scenarios.

The chapter is organized according to the following plan: at first, the working principle of the system is explained, then a preliminary evaluation of the parameters that play important roles on the tuning process is conducted. Next, the aerodynamic and structural models used for the passive flap 3D aeroelastic implementation are presented. The tuning of the flap is discussed extensively. Normal turbulent wind simulations with multiple seeds are then performed with the goal of assessing the fatigue load reduction capability. Then, multiple ultimate load scenarios, including deterministic gust in combination with generetor fault, passive flap fault, extreme turbulent wind and storming conditions are analyzed according to the certification standards. Finally, synthetic conclusions are drawn.

3.1 Models and methods

Figure 3.1 shows a wind turbine equipped with one passive flap per each blade. Each flap is located between 70% and 80% of the span, which is the configuration considered at the beginning of this study.

Figure 3.1: *Wind turbine equipped with passive flaps.*

The passive device moves in response to the out-of-plane accelerations, occurring with the blade flapping and/or with the tower bending. The response is driven by the inertia of offset masses put in front of the hinge line. The deflection of the passive flap determines a change of the airfoil camber that reduces the airloads, thereby mitigating the bending moments on the main wind turbine components, such as blade root, main bearing and tower base.

Figure 3.2 shows the blade equipped with the passive flap. The offset masses are installed in front of the hinge line by rods, and lie in the existing void between the pressure and suction sides of the blade. In this configuration, the offset mass is also constrained to lie behind the aft shear web.

To assure a good functionality and effectiveness of the passive flap in reducing the fatigue loads, system needs a proper tuning. An accurate sizing of the passive flap parameters should be perfomed in order to satisfy some design drivers partly mentioned in the preliminary study, and here reported in a more comprehensive form:

1. the flap chord and the offset mass should be selected in order to have load mitigation capability without interfering with the blade aft shear web;
2. the flap extent should be selected large enough to have a certain load authority, but without affecting the rotor aerodynamic capabilities. Futhermore, the spanwise position should be outer enough in order to have a considerable arm with respect to the blade root;

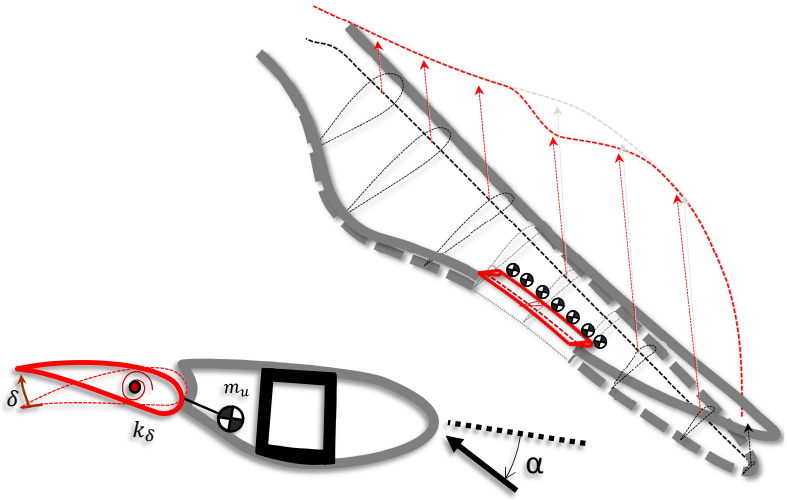

Figure 3.2: *Passive flap concept for load alleviation.*

3. the flap should not respond to the blade pitch angle variations, thus avoiding interactions with the active control on-board that can generate increased blade pitch duty cycle and compromising the emergency recovery procedures. A way to fullfill this requirement is to have a certain degree of aerodynamic balancing;

4. the flap should have negligible impact on the power production. Expecially in region II, where the aerodynamic optimum is required, the device should not significantly modify the rotor shape.

The latter requirement is strictly related to the control strategy of the machine. In the specific, the 10 MW wind turbine is operated with a variable pitch-torque control strategy, including partial load regime (or region II) from cut-in to rated speed, and the full load regime (or region III) from rated to cut-out [64]. To optimize the power capture in region II the rotor as to perform at the maximum efficiency. Since the passive flap modifies the airfoil camber, a loss of the AEP due to the mean flap misalignment is expected. Therefore, an accurate choice of the hinge preload, possibly scheduled with the operative condition, would be an effective mitigation to this concern. The excess power is instead available in region III therefore the blade pitch controllers automatically compensates for the mean flap misalignments, by means of the rotor speed, without incurring in AEP losses. Since its passive nature, the passive flap can be modeled as a spring mass system as following:

$$J_\delta \ddot{\delta} + K_\delta \delta = M_a + M_i + M_p \tag{3.1}$$

where δ is the flap displacement, J_δ the flap inertia, K_δ the hinge stiffness, M_p the hinge preload, M_a the aerodynamic moment and M_i the moment induced by the

inertial coupling. The latter term is related to the offset mass. It can be written as function of offset mass, rotor speed and gravity acceleration:

$$M_i = M_{m_o} + M_\Omega + M_g \tag{3.2}$$

The terms M_Ω and M_g are correlated to the precone, tilt angle and offset mass. In fact, when the precone is different from zero, the centrifugal force acting on the offset mass has a component in a plane perpendicular to the flap hinge, thus creating a constant moment with the arm d. Similarily, through the precone angle, a cyclic moment at 1xRev is caused by the gravity adding to the centripetal acceleration. Furthermore, the up-tilt determines an out-of-plane gravity component that, with the arm d, generates a constant moment to the flap hinge.

The term M_a is the aerodynamic moment:

$$M_a = qS_f c_f C_H + M_a^{NC} \tag{3.3}$$

where q is the dynamic pressure, S_f the flap surface, c_f the flap chord and C_H the hinge moment coefficient $C_H = C_{H0} + C_{H,\alpha}(\alpha^C + \alpha^G) + C_{H,\delta}\delta^C$, and M_a^{NC} represents the non-circulatory unsteady correction. The term $C_{H,\alpha}$ is kept null or negligible to satisfy the aerodynamic balancing. Effective ways to achieve the aerodynamic balancing is to act on the flap leading edge shape and on the flap overhang.

Since both the inertia and the aerodynamic loads are function of the operating condition, the term M_p, representing the hinge preload, can be used to compensate for the mean flap misalignment. In principe it can be either constant or scheduled. A scheduling with the operating condition at which the machine is functioning, i. e. with the wind speed, would require a wind speed estimator that would raise the complexity of the system. A scheduling with the rotor speed is a more reliable solution, since it can be realized mechanically by the use of a screw joint as shown by [12]. In this case, in region III, where the angular speed is constant, the mean flap displacement can not be nullified. This is not a problem since the excess wind power allows to operate in a non-maximum efficiency condition, while for machines with the transition region II ½, the power losses would happend whenever the rotorspeed reaches its upper limit before the rated power is approached.

3.1.1 Constant preload

The mean flap misalignment can be minimized by proper tuning of the hinge preload. A constant value can be selected with the use of a spring. The tuning of the preload should be based on considerations related to loss of AEP and load mitigation capabilities within the operating range of the machine.

3.1.2 Rotor speed varying preload

With the screw joint it is possible to use the centrifugal force acting on the passive flap mass to generate a rotor speed varying preload. In occurance of a flap deflection δ, the screw generates a linear displacement z parallel to the hinge axis. Therefore it is a means of creating a kinematics coupling, which translates into a transmission

ratio, $\tau = P_0/(2\pi)$, where P_0 is the screw pitch. Considering the presence of this transmission ratio, Equation (3.1) modifies as following:

$$\bar{J}_\delta \ddot{\delta} + K_\delta \delta = M_a + M_i + \tau(F_c + F_g) + M_0 \tag{3.4}$$

where the preload moment is $M_p = \tau(F_c + F_g) + M_0$ with M_0 a constant value and F_c and F_g the centrifugal and gravitational forces, respectively. The term $\bar{J}_\delta$ is the inertial moment increased by the transmission ratio, and is expressed as:

$$\bar{J}_\delta = J_\delta + \tau^2 m \tag{3.5}$$

The centrifugal force can be approximately expressed as

$$F_c = m(r + z)\Omega^2 \tag{3.6}$$

where r is the distance of the flap mass with respect to the rotor axis, and z the linear displacement of the flap. Inserting Equation (3.6) into Equation (3.4), one gets:

$$\bar{J}_\delta \ddot{\delta} + (K_\delta - \tau^2 m\Omega^2)\delta = M_a + M_i + \tau m r\Omega^2 + \tau F_g + M_0 \tag{3.7}$$

where it is highlighted that the effective stiffness decreases of a quantity $\tau^2 m\Omega^2$. The gravitational force is expressed by:

$$F_g = mg\cos\psi \tag{3.8}$$

where ψ is the blade azimuthal position and g the acceleration of gravity. The transmisson ratio τ and the constant M_0 are chosen so as to nullify the mean of the right hand side of Equation (3.7):

$$\tau m r\Omega^2 + M_0 = -(M_a + M_i) \tag{3.9}$$

Note that term F_g is not considered in Equation (3.9) since it is a periodic disturbance with zero mean. The tuning of τ and M_0 looks at nullify the mean hinge moment where the control strategy varies the rotor speed, i. e. in region II. A Least-Square method can be used to determine the best fitting values of τ and M_0, after the evaluation of the hinge moment by normal wind profile (NWP) simulations of the wind turbine.

Figure 3.3 shows the mean flap misalignment with the rotor speed varying preload versus the solution with a constant preload. The flap is implemented in the 3D aeroservoelastic model of the wind turbine, whose details are presented in Section 3.1.4. The results are referred to NWP simulations performed over the entire operating range. The figure highlights that with the rotor speed varying preload the flap misalignment is very small in the region from 7 to 11 m/s (where the rotor speed is varied by the control strategy reported in Figure 4.4), then it increases over the solution with constant preload in region III. In the figure, the solution with constant preload guarantees a null mean flap misalignment at the hub height wind speed equal to 9.5 m/s and 14 m/s. The choice of the constant preload, when opting for the solution without scheduling, is very important at the light of limiting the power production loss, as will be shown in the Section 3.3.1.

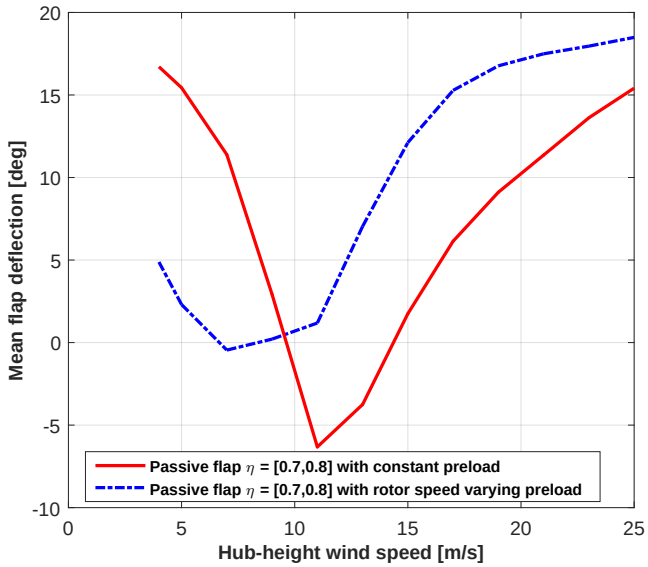

Figure 3.3: *Mean flap misalignment over the entire operating range. Comparison between passive flap with rotor speed varying preload and with constant preload.*

3.1.3 2D sensitivity analysis

In Section 2.2.4 it was shown the transfer function between angle of attack and the three degrees of freedom of the model. In that case the flap was optimized by tuning the flap frequency and the damping. Here, due to the increased modeling complexity in the 3D environment, it is more convenient to account for a larger number of tuning degrees of freedom. The 2D analysis is performed again, with the goal of highlighting the sensitivity of the system to the offset mass at different flap frequencies. Figure 3.4 shows at left the transfer function of the sole plunge with respect to the angle of attack in the rated turbulent wind speed condition. Five plots are shown: the black dotted line represents the typical section without the passive appended device. The red dot-dashed and solid lines refer to the typical section with the flap structural frequency of 90% of the 1xRev and with the offset mass distance respectively of 15% and 20% of the blade chord. The blue dot-dashed and solid lines refer to the typical section with the flap structural frequency reduced of a decade and with the offset mass distance respectively of 15% and 20% of the blade chord. In all the conditions the offset mass is set equal to around 20% of the sectional specific mass. These values are chosen after some trials with the 3D aeroelastic model, whose details are described hereinafter. Looking at all the lines, it is possible to observe that the section with flap shows a bandstop behaviour between the aeroelastic flap frequency[1] considerably below 1xRev and the aeroelastic plunge frequency that is higher then the 3xRev.

Figure 3.4 reports at right the fraction of the blade root bending moment weighted DEL of the blade without flap in function of the load frequency, evaluated in NTM

[1]It should be remarked that the 2D sectional model includes the centrifugal (negative) contribution to the passive flap stiffness

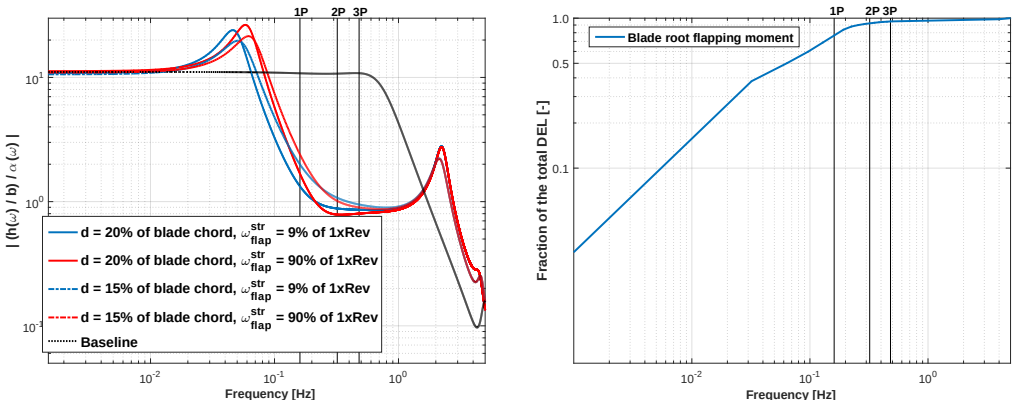

Figure 3.4: *At left: transfer function of the plunge motion of the semi-analytical sectional model vs. angle of attack variation. Comparison between baseline (without flap) and section with flap. At right: fraction of the weighted DEL of the blade root flapping moment vs. frequency of the 10 MW wind turbine baseline (without flap).*

conditions by the Rainflow-counting algorithm. It contains the same informations of Figure 2.8, but plotted here in log scale. As the band increases, the fraction obviously tends to unit value. It is possible to observe that there is a considerable slope until 1xRev where the DEL achieves almost 80%, then rises up to 96% when the 3xRev is approached, finally the curve becomes flat reaching the unit value at very high frequencies. Looking at both graphs of Figure 3.4, one can see that the bandstop behavior exibited by the section with passive flap occurs in the range of frequencies with the highest energy content. Looking at FFT curves again, a lower passive flap frequency increases the bandstop since the lower resonant peak moves backward. Selecting higher offset mass distances helps in reducing the magnitude at frequencies between the lower resonant peak and the 1xRev, where in turn the most ripid slope in terms of DEL accumulation is observed. This brings at the selection of low passive flap frequencies and at maximizing the offset mass distance[2].

3.1.4 3D flap model

Figure 3.5 illustrates the main characteristics of the machine equipped with passive flaps. The multibody formulation of the wind turbine model is described in Section 2.1.1.

The flap aerodynamics is modeled as property of the lifting line using the thin airfoil theory, where the quasi-steady sectional hinge coefficients are estimated with the *ESDU* semi-empirical method [59] and parameterized in function of angle of attack and flap deflection. The WSU post-stall corrections due to control surface deflection are then applied as in Ref. [60]. The other sectional aerodynamic coefficients are also scheduled in terms of angle of attack and flap deflection, the latter parameterization evaluated by the open-source software `XFoil` [61]. The deformable beam model is used for the flap. The blade/flap assembly follows the indications in Ref. [62], in order to avoid hyperstatic constraints that would raise some difficulties

[2]Until the occurrance of instability phenomena or nearness to the aft shear web.

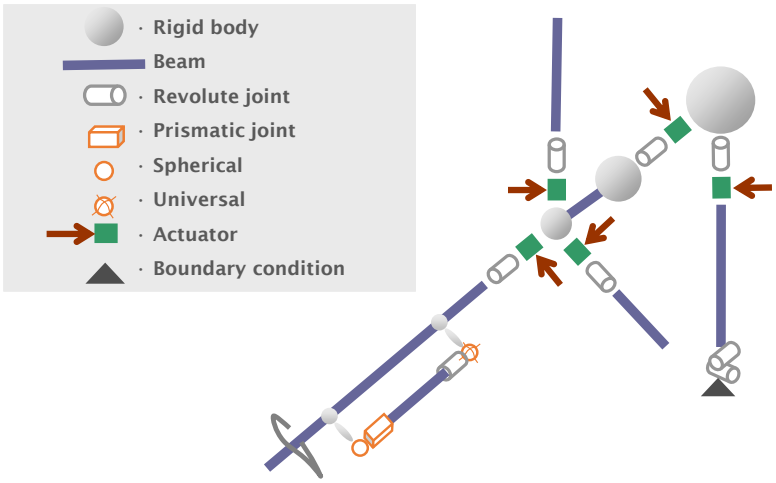

Figure 3.5: *Topology sketch of the wind turbine whose the blade is equipped with the passive flap.*

in the numerical simulations. The flap is attached to the blade by two brackets. Between flap root and inner bracket a universal and a revolute joint are inserted with the scope of reproducing the spherical joint kinematics with the revolute allowing the inclusion of a spring to model the hinge stiffness. A spherical plus a prismatic joint are put between the outer bracket and the flap tip. The prismatic joint is useful to avoid compression in the axial direction. Rigid bodies are used to model the offset masses in front of the hinge line, despite they are not illustrated in the model topology.

3.2 Validation of passive flap 3D aeroservoelstic model

To validate the flap 3D aeroelastic model, the typical section used in Section 3.1.3 is implemented in the mutibody environment. The topology comprises an untwisted and untapered blade with unit span equipped with the passive flap over the entire span. The sectional properties are the ones at 75% of the blade span and the mechanical properties are defined by lumped parameters as following:

- A stiff beam is used for the blade structure, which allow the connection between the aerodynamic and structural grid (beam/lifting line);
- A linear spring on a prismatic joint is used to define the blade flapping stiffness;
- Two torsional springs are put on two revolute joints to define the blade torsional stiffness and the passive flap stiffness.

Equivalently to the 2D typical section, the system has three degrees of freedom: plunge, torsion and flap displacement. The aerodynamics is the one used for the 3D aeroelastic modeling, based on the classical unsteady strip theory extended to the case of large frame motions, general cross-section deformations and general

inflow model, which is provided externally. The coefficients are evaluated here by the Theodorsen method [51], in order to match with the ones used in the 2D modeling for the preliminary investigation, which implements the Wagner theory and four aerodynamic states for the inflow model. The aerodynamic balancing is not included in this model validation, and it would simply require the evaluation of the overhang contribution on the aerodynamic coefficients, not adding any significant difference in the mathematical model.

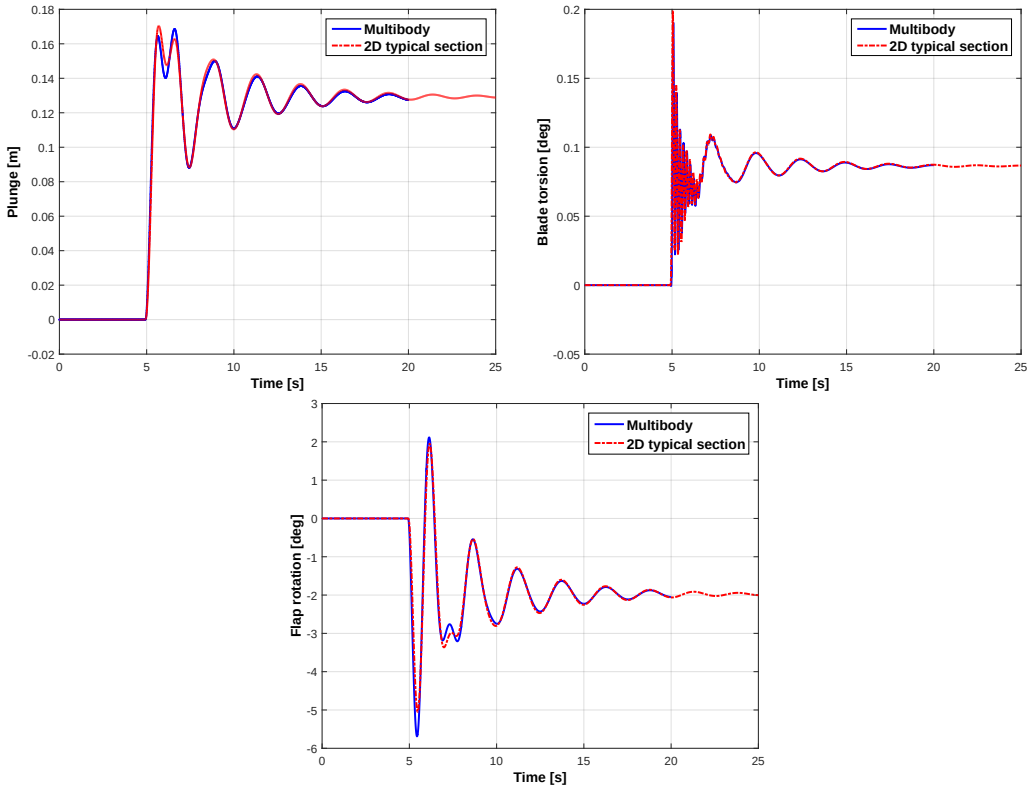

Figure 3.6: *Comparison between 2D sectional model and its implementation in the 3D multibody environment. Blade plunge, blade torsion and flap rotation step response to the angle of attack variation.*

The comparison is perfomed by the response to a step change in angle of attack, imposed with a vertical gust. The results are reported in Figure 3.6, in terms of the three degrees of freedom. The comparison shows a general good agreement between the two models. The regime value is perfectly matched, while minor differences are observed for the first two transient peaks.

3.3 Passive flap sizing

Tuning of the device looks at maximizing the load mitigation by respecting the design drivers discussed in the Section 3.1. The flap is designed as following:

- The overhang is selected in order to achieve the aerodynamic balancing, i.e. a negligible hinge moment rate of change with respect to the angle of attack.

Thus, with the scope of minimizing the interaction with the blade pitch control system;

- The flap initially occupies the blade span between 70% and 80%, then an extent of the flap will be considered next, with the scope of evaluating the trend of growth in load reduction;
- The hinge stiffness is selected to have the natural frequency significantly below the 1×Rev, as suggested by the 2D sensitivity analysis.
- The local chord is 25% of the total blade chord in order to maximize the flap authority for the load mtigation and avoid possible interference with the aft shear web.

3.3.1 DEL-based inertial tuning

Referring to the sketch of the flapped blade section shown in Figure 3.2, offset masses ahead of the flap hinge are necessary in order to achieve an effective inertially driven response.

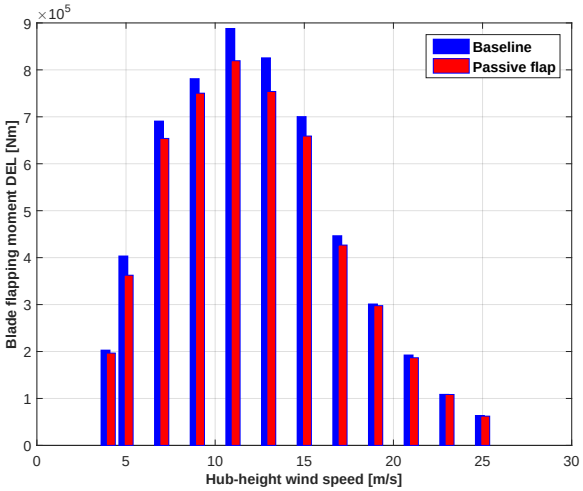

Figure 3.7: *Blade bending moment DEL varying with the operating condition. Comparison between baseline with and without passive flap. Flap parameters not optimized.*

The offset mass with its arm with respect to the hinge line determines the magnitude of the flap deflection, with a direct impact on the loads and performance. Therefore, a first step regards the selection of m_o and d. This is done by some aeroservoelastic simulations in NTM performed by varying these two parameters. For computational cost reasons, this evaluation is made only at $V_{wind} = 9, 11, 13$m/s, where the fatigue load is higher, as shown by Figure 3.7 where it is reported the Weibull weighted DEL of the blade root out-of-plane moment for the 10 MW wind turbine with and without passive flap, whose the tuning parameters are not yet optimized. Figure 3.8 shows the weighted DEL percentage reduction in edgewise and flapwise direction of the bending moment at the blade root. The study is conducted by varying the offset mass, that is reported on the x-axis, and its position ahead of

the hinge, reported in the y-axis. In the grey area the offest mass would be too close to the aft shear web, thus resulting in a possible interference. A significant DEL reduction is achieved in the flapwise direction, which improves as the offset mass becomes higher. Vice-versa, the edgewise records an increased DEL, first due to the drag force incresed by the flap fluctuations, and second due to the increased blade weight caused by the offset masses, that in the in-plane direction pulses at 1xRev with its ample arm.

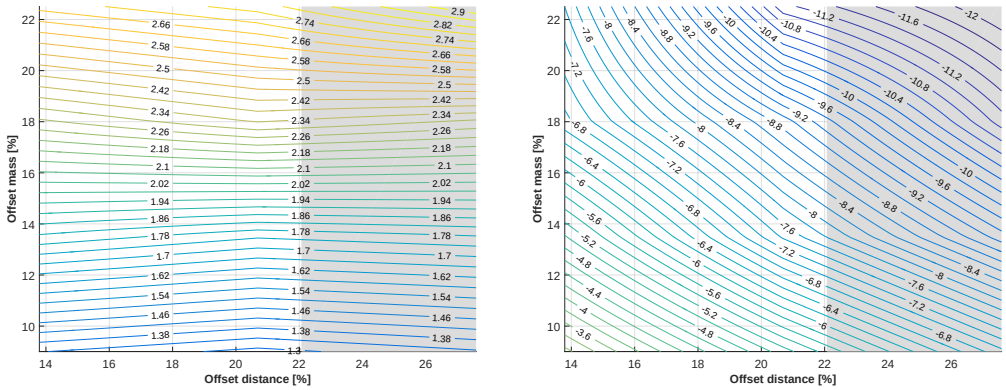

Figure 3.8: *DEL variation percentage with respect to the baseline without passive flap. Sensitivity analysis to offset mass and offset distance from the hinge variations. Blade root edgewise moment component at left. Blade root flapwise component at right.*

An accurate evaluation of the DEL bending moment affecting the fatigue life of the blade root requires the projection of the flapwise and edgewise components at different orientations over a round angle on the spot analyzed. For each orientation, the DEL is calculated. Then, the highest DEL determines the fatigue stress to which the structural component is subjected. Figure 3.9 reports at top the DEL variations considering the highest DEL, which is the *physical* bending moment DEL of the blade root. The most critical direction, i. e. the direction where the highest DEL is registered, appears to be close to the edgewise. The physical DEL reduction is very poor. Avoiding the grey area, at the point where the offset mass is around 18% of the blade specific mass and at a distance from the hinge of around 21% of the blade chord, a corner appears, which represents a local minimum. By the way, higher offset mass values would reduce considerably the blade out of plane modal frequencies. Figure 3.9 shows at bottom left the physical DEL variation of the main bearing bending moment, which is mainly generated by the blade flapping. A DEL reduction is observed here, with trend suggesting the choice of high offset mass and distance values. Keeping the offset mass at 18%, and the distance at 21%, it appears a reduction of around 3.5%. Figure 3.9 shows at bottom right physical DEL variation of the bending moment at the tower base. The highest DEL direction is very close to the fore-aft, and it is mostly generated by the tower top fluctuations induced by the thrust. With the tuning selected, i. e. with the offset mass equal to around 18% and a distance of 21%, a DEL reduction of around 12% is found.

As mentioned before, the choice of the offset mass has significant impact on the overall dynamics of the machine. The first modal frequencies are evaluated

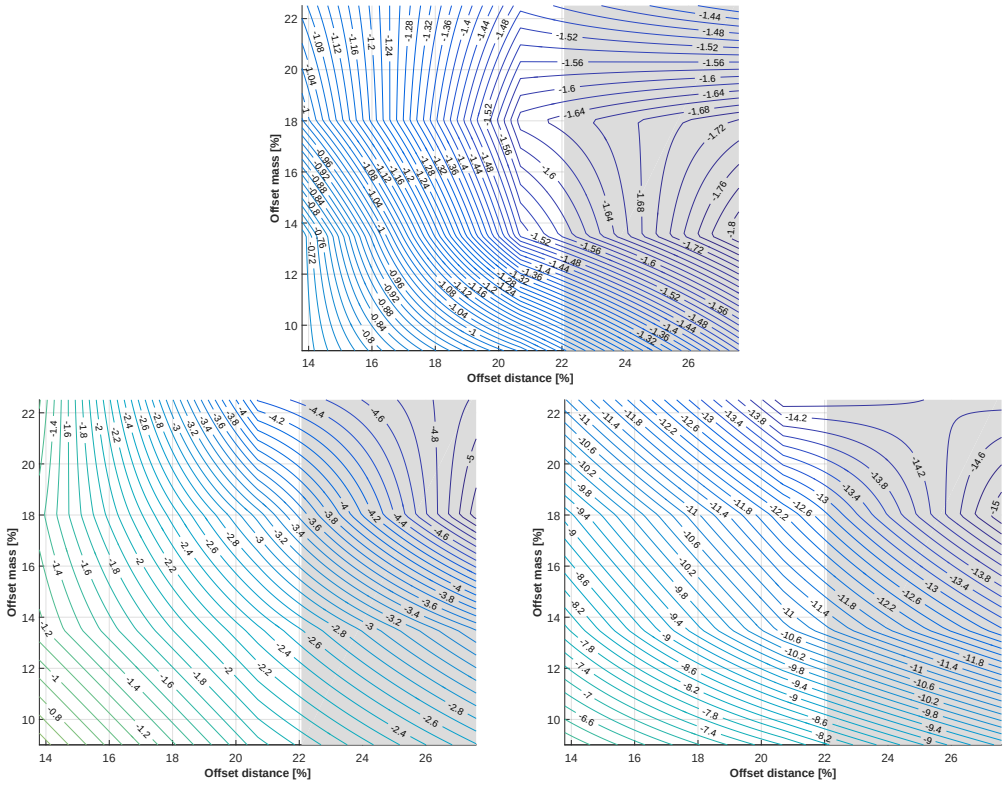

Figure 3.9: *DEL variation percentage with respect to the baseline without passive flap. Sensitivity analysis to offset mass and offset distance from the hinge. Blade root bending moment physical DEL at top. Hub bending moment physical DEL at bottom left, tower base bending moment physical DEL at bottom right.*

accounting for the centrifugal effects, by the Campbell diagram as in Figure 3.10. Minor differencies are found for the the two tower modes (fore-aft and side-side). The three rotor out-of-plane modes appears to be reduced of around 2%. However this reduction still remains acceptable, since crossings with the first three xRev frequencies appear first at a frequency approximately of 120% of the rated rotor speed. This however indicates that an higher value of offset mass would have been unacceptable. Finally the first two rotor in-plane modes are reduced of around 3%, and this is also acceptable since in general they are not critical for the blade design.

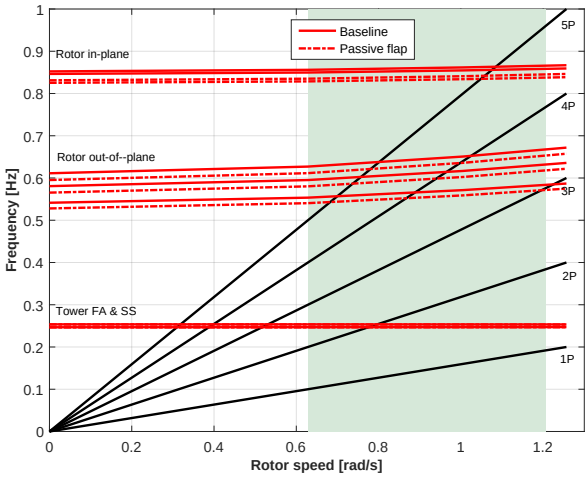

Figure 3.10: *Campbell diagram of the 10 MW wind turbine with and without passive flap. Passive flap span $\eta = [0.7, 0.8]$, flap offset specific mass = 18% of the blade sectional mass, flap offset distance = 21% of the blade chord. The green area is the extended operating range from cut-in to 120% rated rotor speed.*

The hinge preload plays also an important role, since it determines the mean flap misalignment with the fixed part of the blade, thus resulting in a change of the mean airfoil camber that in turn impacts on the rotor aerodynamic efficiency. Indeed, the power production capability of the rotor is characterized by the power coefficient C_p, where in region II is required to be maximized, thus allowing to extract the maximum energy from the wind. In region III the excess power is rejected by the blade pitch control, therefore the maximum rotor efficiency is not required anymore. To this end, the NTM simulations are conducted over the entire operating range, to account for the AEP and DELs. The model is first simulated with three different constant values of the applied hinge preload, respectively $M_{v_w=7.5m/s}$, $M_{v_w=9.5m/s}$ and $M_{v_w=10.5m/s}$, which means the three hinge torsional moments registered at a wind speed of 7.5 m/s, 9.5 m/s and 10.5 m/s. This choice nullifies the mean flap misalignment at those wind speeds. Then, it is also considered the case with the screw joint, tuned following the procedure in the Section 3.1.2, that allows to have a null or very small mean flap displacement in the region II where the rotor speed is varied by the control strategy, as shown in Figure 3.3.

The results are shown in Figure 3.11 in terms of DELs and AEP variation. For the DELs, three bending moments are considered indicative: the blade root flapping, the main bearing and the tower base bending. The results highlighted by the dark

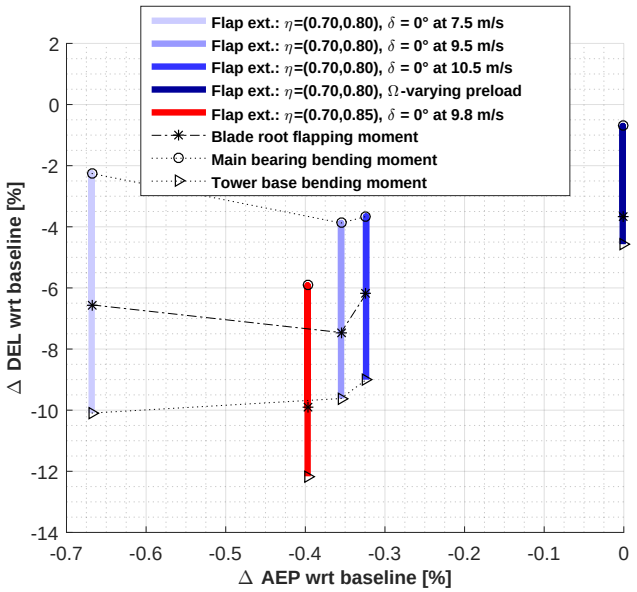

Figure 3.11: *DEL/AEP variation study. Sensitivity analysis by varying the hinge preload. Flap offset specific mass = 18% of the blade sectional mass, flap offset distance = 21% of the blade chord.*

blue bar on the right side of the graph are referred to the case with the screw joint. As expected, this case is the best in terms of AEP, since the loss appears to be practically null, and the DEL reduction goes from around 1% for the main bearing, to around 4.5% for the tower base, which seems not satisfactory if compared with the results obtained with the constant preload, highlighted with bars in light blue scale. This fact is due to several reasons, and they depend on the physics of the scheduling mechanism. Indeed, the preload is generated by the inertial forces acting on the flap mass through the transmission ratio τ (see Equation (3.4)) by the in-plane component of the acceleration, which is not only of centripetal nature, as in the simplification assumed for the tuning of τ and M_0, but it contains many other contributes, among them, the most important are the gravity cyclic component at a 1xRev pulsation (see Equation (3.8)), the blade flapping, the blade rotation and the flap deflection itself. All of these contributions reflect on the flap response since they affect the scheduled preload, with the result of an increased load fluctuation.

Looking at the abscissa it appears that the AEP decreases when the constant preload is imposed equal to the hinge torsional moment at wind speeds in the lower region II. Looking at ordinate, with a preload $M_p = M_{V_w=9.5m/s}$ an optimum in terms of DEL reduction for the blade root flapping and the main bearing bending is observed, while the tower base DEL tends to decrease with the AEP losses. An AEP loss corresponding to this optimum is 0.33%, which is considered acceptable, despite a deeper analysis to quantify the impact on CoE should be conducted to identify the best trade-off.

Furthermore, an increase of 50% of flap extent toward the outer portion of the blade is considered, keeping this time the same inertial tuning, i. e. the same offset

mass distribution m_o, distance d and hinge preload. The results are highlighted in Figure 3.11 by the red bar. The DELs is now reduced of a further 2%, with an increased AEP loss of around 0.05%, denoting an interesting trend of growth in terms of load reduction capability while not significantly impacting on the AEP.

Table 3.1 summarizes the main flap parameters that will be used for more detailed analysis on fatigue and ultimate loads.

Table 3.1: *Passive flap tuned parameters on DTU 10 MW Wind turbine.*

Parameter	Value
Flap extent	$\eta = [0.7, 0.8]/[0.7, 0.85]$
Flap chord	25% blade chord
Flap overhang	53% flap chord
Offset mass	18% blade spec. mass
Offset distance	21% blade chord
Flap frequency	0.014 Hz (9% of 1xRev)
Hinge preload	$M_{Vw=9.5m/s}$ with $\eta = [0.7, 0.8]$

3.4 Results

The performance of the proposed passive flap was evaluated by simulations of the wind turbine in many operating conditions, as required by the certification standards [38, 39]. Among the various design load cases (DLCs) used for the design of the the machine [37], worse scenarios in terms of fatigue and ultimate loads were selected. For the normal turbulent wind conditions, which are used for the fatigue load characterization, the results were averaged over four different turbulence seeds [63].

3.4.1 Standard design conditions

The standard power production range was considered first by the DLC 1.1 from the cut-in to the cut-out speeds in 2 m/sec of increment. The AEP percent variations with respect to the baseline configuration without the passive flap are reported in Figure 3.12. Apparently, the AEP loss is increased now that four turbulence seeds are considered, if compared with the case of one seed used for tuning the flap parameters. Indeed, it appears an AEP loss of 0.5% for the case of flap extent $\eta = [0.7, 0.8]$, while 0.55% for the flap flap extent $\eta = [0.7, 0.85]$. However this is not considered a concern, since Figure 3.11 showed that it is possible to increase the AEP by opportunely change the hinge preload. Therefore, even if not performed here, a further tuning iteration of the hinge preload would be enough to adjust the AEP.

DELs are evaluated at a number of spots on the machine based on Rainflow-counting. The blade root, main bearing and tower base were selected as fatigue verification spots because they are indicative of possible structural regions prone to fatigue problems. DELs corresponding to the combined moment at the most

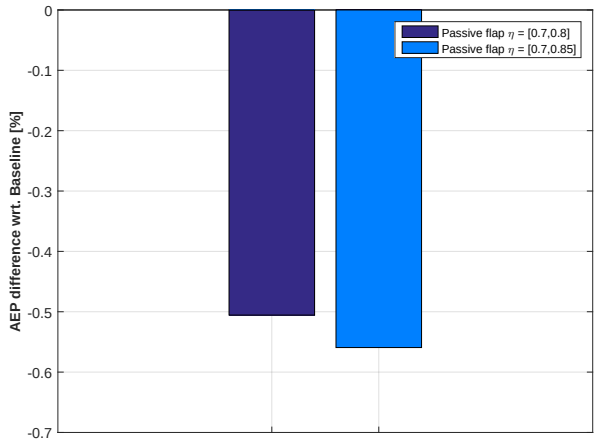

Figure 3.12: *AEP variation percentage with respect to the baseline. Flap offset specific mass = 18% of the blade sectional mass, flap offset distance = 21% of the blade chord.*

damaged point (the physical DEL) at each verification section are reported in Figure 3.13.

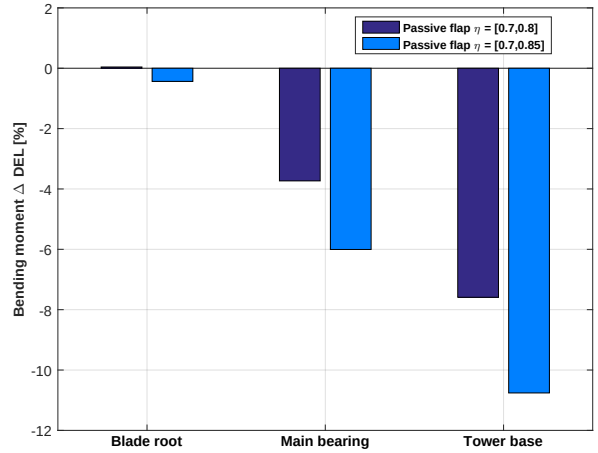

Figure 3.13: *Bending moment weighted DEL variation percentage with respect to the baseline at the main spots: blade root, main bearing, tower base. Flap offset specific mass = 18% of the blade sectional mass, flap offset distance = 21% of the blade chord.*

The flap in both the extents appears to be lowering considerably the fatigue loads at the main bearing and tower base, with a very clear growth trend of capability with the flap extent. It is very interesting to appreciate the ample reduction at the tower base, since the passive flap directly responds to the tower top accelerations caused by the thrust fluctuation, while at the main bearing, the reduction is driven by the the blade flapping reduction. At the blade root the DEL reduction is not appreciable, due to the increased bending moment in the in plane direction as discussed previously.

To this end, Figure 3.14 reports the DEL calculated on the three moment compo-

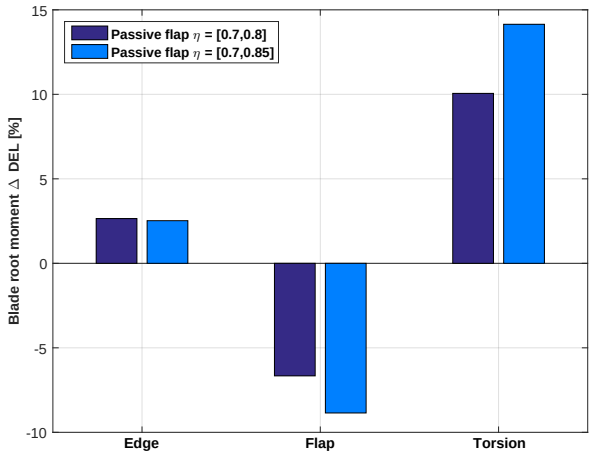

Figure 3.14: *Blade root moment weighted DEL variation percentage with respect to the baseline. Flap offset specific mass = 18% of the blade sectional mass, flap offset distance = 21% of the blade chord.*

nents of the blade root. It appears an increase of around 2.5% in the edge direction for both the flap extents. This is due to an increased drag fluctuation caused by the flap deflections, and also do the cyclic blade weight effect, that is increased with the addition of the offset mass at the blade portion were the passive flap is installed. Looking in the flapping direction, an appreciable DEL reduction of around 6.5% and 8.8% is found for respectively flap extent $\eta = [0.7, 0.8]$ and $\eta = [0.7, 0.85]$, which significantly reflects on the main bearing bending moment. The torsional moment DEL records a significant increase of around 10% for flap extent $\eta = [0.7, 0.8]$ and 14% for the flap extent $\eta = [0.7, 0.85]$, due to the increased pitching moment fluctuation generated by the passive flap deflection. This may affect the fatigue life of the pitch actuator. On the other hand, Figure 3.15, which reports the ADC, shows that pitch activity is reduced, therefore the analysis on the effective pitch actuator workload is much more complex. However, a possible solution to this issue would be the implementation of a system of a trailing edge and leading edge flap, similar to the that proposed in [17], and providing the system with sufficient aerodynamic balancing.

As mentioned, the collective pitch activity is reported in Figure 3.15 in terms of ADC vs. hub-height wind speed, where ADC over a time span T is computed as

$$ADC = \frac{1}{T}\int_0^T |\dot{\beta}|\mathrm{d}t. \tag{3.10}$$

The reduction is noticable and similar for both the flap extents. This can be attributed to the smoothing of the airloads performed by this device, which in turn yields a smoother response of the machine and a consequent reduced activity of the controller in reaction to wind fluctuations.

An ultimate load analysis was performed by considering a selected set of DLCs, usually the most demanding for the wind turbine design. DLC 1.1 and 1.3 focus on power production in standard and extreme turbulence conditions. In DLC 2.3, a

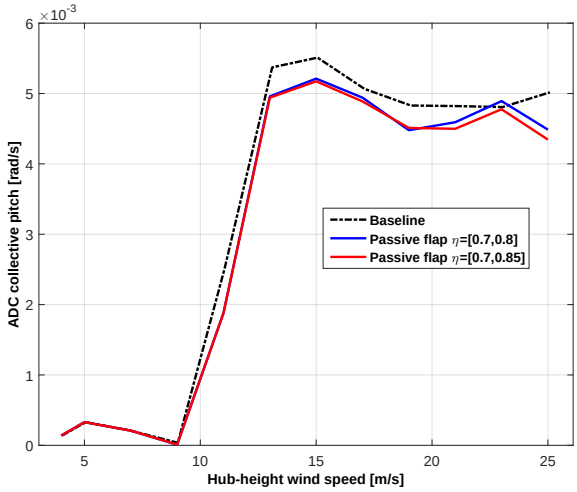

Figure 3.15: *ADC variation percentage with respect to the baseline. Flap offset specific mass = 18% of the blade sectional mass, flap offset distance = 21% of the blade chord.*

deterministic gust occurs in conjunction with a grid loss, and the effects of the fault time are examined by multiple simulations. Finally, DLC 6.2 considers parked conditions with grid failure, where multiple yaw conditions are considered to identify the worst scenario.

Attention is focused on the combined bending moments at blade root, main bearing and tower base, and percent variations of the ultimate loads with respect to the baseline are reported in Figure 3.16. Better performance is achieved at the main bearing and at the blade root, where the most demanding situations occur among the DLC 1.3 scenarios. As in the case of fatigue damage, the passive flap in both the extents seems to be able to smooth out airloads, with a beneficial effects also on peak loads. Furthermore, the increase of the extent appears to have the desired effect of further decrease the loads.

Stormy conditions DLC 6.2 are the most demanding situations for the tower base bending moment. The peaks appears to be reduced by the passive flap, similarly for both the extents. The physical explanation is the reduced sail area of the blade, since during storms the flaps remain deflected in proximity of the stops. This may in turn somewhat reduce loads.

3.4.2 Off-design conditions

The effects of the passive flap failure are investigated to understand if the advantages of the proposed solution can be nullified by a fault of the system. The fault is investigated by blocking the relative rotation of a single passive flap, while the others remain functioning. It is supposed that the wind turbine is equipped with a safety system to detect the fault and trigger an immediate shut down procedure. Generator fault or loss of electrical network are not included in the fault scenario, because simultaneous malfunctions are considered remote scenarios.

The passive flap fault is verified by DLC 2.1 and 2.3 with the scope of identifying the most demanding condition. A single seed is considered for DLC 2.1 NTM sim-

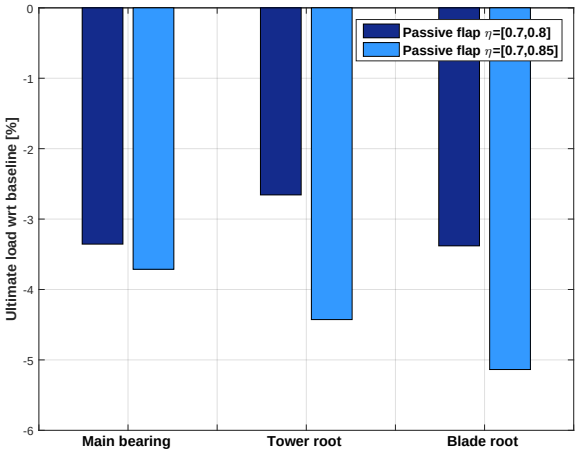

Figure 3.16: *Percent variation of ultimate loads at verification spots with respect to baseline. Flap offset specific mass = 18% of the blade sectional mass, flap offset distance = 21% of the blade chord.*

ulations because the relative position of the fault with respect to wind fluctuations is more important than the analysis of different wind realizations. The passive flap fault is imposed in conjunction with a positive steep gradient or a maximum of the hub-height wind speed. These two conditions are respectively labeled "grad" and "peak". When turbulent winds are considered, each simulation is associated to a number, which represents the mean hub-height wind speed, and a letter, identifying a turbulent seed. DLC 2.3 simulates a deterministic extreme operating gust (EOG) at cut-out (labelled vo), rated (labelled vr) and rated ±2 m/sec (labelled vr±2) wind speed. In total, 16 simulations were performed at each wind speed, varying the time interval between the gust and the fault as well as the azimuthal position of the faulty passive flap. Each simulation is identified by a number that refers to one of these combinations.

The off-design performance is investigated by ranking the ultimate loads of the standard envelope plus the fault conditions in decreasing order, and looking at the maximum load peak. The first three ranking combined moments at the tower base are reported for each configuration in Figure 3.17, where the fault conditions are identified by using gray-shaded bars.

A passive flap failure is considered dangerous if the maximum load peak increases with respect to the baseline configuration. The ranking analysis for blades and main bearing are not reported here, because fault conditions do not modify the highest three ranking loads. In fact, DLC 1.3 remains the load case driving blade and main bearing design. On the contrary, the combined moment at the tower base is affected by the rotor imbalance caused by the passive flap of extent $\eta = [0.7, 0.85]$, as it appears at the third position of the ranking. Therefore, off-design conditions may generate loads that are comparable than in the non-faulty standard DLCs.

The results reported in the figure show that in any case the passive flap fault does not cause an exceeding of the load envelope of the baseline machine. In addition, fault conditions are not load drivers for both the flap extents.

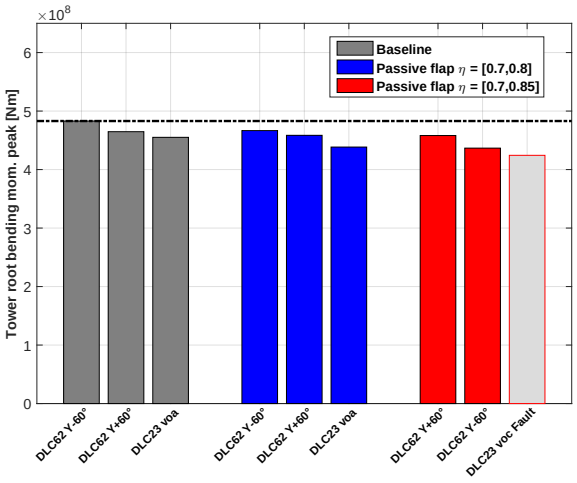

Figure 3.17: *Ranking analysis of tower base combined moment. Passive flap fault conditions are displayed using gray-shaded bars.*

3.5 Synopsis

A passive flap concept for load mitigation on wind turbines has been investigated in this chapter by a 3D aeroelastic model implemented on a large conceptual 10 MW machine. The analysis considered both fatigue and ultimate loads, including also device fault conditions, following accepted standard certification procedures. Based on the results of the present analysis, the following conclusions may be drawn:

- The proposed passive flap solution improve on the baseline in terms of fatigue and ultimate load alleviation. These results might possibly be further improved by a more complete optimization of the devices, including their aerodynamic shape.

- The more significant effects on fatigue are reported at the tower base. This is due to the tower top acceleration that drives the passive flap deflection and smoothing of the airloads. The fatigue at the main bearing is also mitigated, and this is essentially due to the driven flap response by the blade flapping. The fatigue mitigation at the blade root appears very poor. A more detailed analysis on the blade root bending components reveals that this is due to an increased drag fluctuation induced by the flap deflection and the increased blade weight by the installation of offset masses, which increases the bending moment in the edgewise. At the same time a considerable reduction of the bending in the flap wise is encountered.

  The blade torsion DEL is also increased, due to the increased pitching moment fluctuation generated by the passive flap deflection. This may affect the fatigue life of the pitch actuator, which, on the other hand reduces its activity in feedback, due to the smoothing of the airloads performed by the passive device. Therefore the effective actuator workload evaluation requires more complex analysis. However, a possible solution to this issue would be to include also a

leading edge flap that would oppose this pitching moment contribution.

- Ultimate loads see a considerable decrease at the three spots, i. e. blade root, main bearing, and tower base. Therefore the passive flap system, even if not its primary function, appears to be lowering also the ultimate peaks. Furthermore, the increased flap extent showed that the peaks are further decreased.
- The consequences of device faults are limited, with no effect on the ultimate design-driving loads. Indeed, by ranking the results, it seems that increasing the flap extent of 50%, at tower base the bending moment peak becomes comparable to those of the standard design conditions.

CHAPTER 4

3D aeroservoelastic analysis of blade tip device architectures

This chapter[1] investigates the load alleviation capabilities of a blade tip device allowed to have a relative rotation with respect to the inner blade portion. The passive solution, is compared with semi-passive and active architectures, developed ad-hoc for the specific topic. In the passive and semi-passive configurations the tip motion is mainly driven by aerodynamic means, while for the active case the rotation is obtained with an actuator commanded by a feedback control law. Each configuration is analyzed and tested using a high-fidelity aeroservoelastic simulation environment, by considering standard operative conditions as well as fault situations. The potential benefits of the proposed blade tip concepts are discussed in terms of performance in reducing the loads and robustness. Figure 4.1)shows the blade pitching tips for the alleviation of loads on multi-MW HAWTs. Passive, semi-passive and active solutions are considered in order to provide a general overview of the possible range of configurations and their respective performance. The passive solution is purely activated by aerodynamic loads, while the semi-passive one uses an active component to apply a varying restraining torque to limit mean tip deflections according to the machine operating condition. Finally, the active solution uses an actuator to drive the tip deflection based on a feedback control law. Each configuration is analyzed in detail, including the tuning of the respective parameters. Performance is assessed using the accepted international certification standards within a high-fidelity aeroservoelastic simulation environment. The chapter is organized as follows. Section 4.1 considers the tip design problem. Passive and semi-passive

[1] This chapter is a revising of the journal paper "Articulated blade tip devices for load alleviation on wind turbines" (see Ref. [24]).

configurations are examined first, providing some general guidelines and a preliminary sizing of the main system parameters for the aeroelastic integration of the devices on board the wind turbine. The active solution is then introduced, and its control algorithm is tuned. Next, Section 4.2 compares fatigue and ultimate loads as well as off-design conditions. Finally, conclusions and an outlook on possible future developments are reported in Section 4.3.

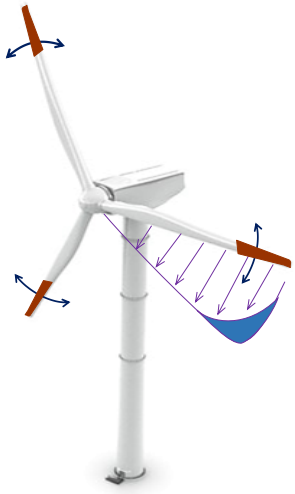

Figure 4.1: *Articulated blade tip concept for load alleviation.*

4.1 Design of blade tip devices

The design of the blade tip focuses here on the properties of the hinge connecting it to the rest of the blade, while the external blade shape is kept constant. This simplification distinguishes the effects of the tip motion per se from further possible effects that could be obtained by modifying its aerodynamic shape. While the approach might be sub-optimal, a specific tailoring of the aerodynamic characteristics of the tip can be analyzed at a later stage.

4.1.1 Passive and semi-passive configurations

The device design aims at optimizing the tip motion in order to mitigate the fatigue load on the blades. The positions of the hinge line (HL), of the tip aerodynamic center (AC) and of the center of gravity (CG) (see Figure 4.2) play a crucial role in determining the physical phenomena contributing to load alleviation.

If the hinge line is close to the aerodynamic center of the blade tip, then the aerodynamic moment is nearly independent from angle of attack changes. Therefore, the device behavior is mainly driven by the inertial response of the blade tip, if its center of gravity is offset with respect to the hinge. This is the same load alleviating mechanism used by Chapter 2 and Chapter 3 for the passive trailing edge flap. On the contrary, if the hinge line is away from the blade tip aerodynamic center while

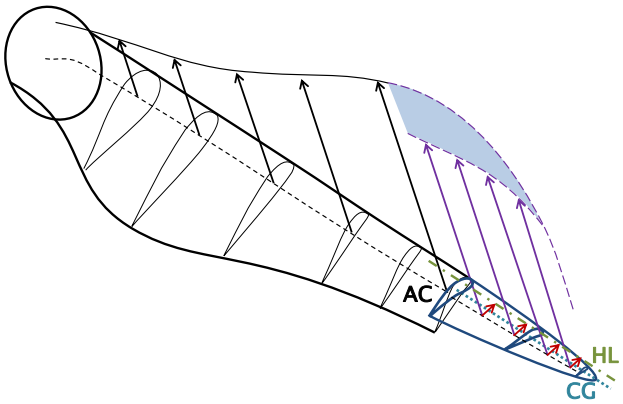

Figure 4.2: *Wind turbine blade with articulated tip.*

the center of gravity is not, then the response is mainly driven by aerodynamic loads. In particular, when the hinge line is forward of the aerodynamic center, an increase in angle of attack at the blade tip will induce an increase in lift and, consequently, a nose down moment at the hinge that will induce a pitch down rotation. This will eventually oppose the original increase in angle of attack, thereby realizing a load mitigating action.

Both the inertial and aerodynamic driven solutions can be used for designing passive load mitigating devices. However, while the former proved to be very effective for the flap case, the latter seems to be better suited for the tip case considered in the present study. Several factors make the inertial-driven solution difficult to implement for this tip device. First, the flap is characterized by the hinge moment rate of change with respect to both angle of attack and flap deflection changes, two parameters that can to a large degree be set independently from each other. On the contrary, a tip device is only characterized by its sole hinge moment rate of change with respect to angle of attack; in addition, the moment with respect to the aerodynamic center is not null because of the non-null camber of the tip airfoils. Therefore, it is much harder for the tip case to obtain good alleviating performance and small sensitivity to disturbances such as gravity and centrifugal loading. In addition, a significant mass ballast is needed to obtain the necessary inertial effects, ballast that in turn lowers the blade natural frequencies and may negatively affect loading. Based on these considerations, the aerodynamic-driven solution is adopted for the present study.

The hinge location is a compromise between the tendency to align with the wind of the blade tip, which sugests a forward position, and a desire to limit inertial couplings, which suggests a hinge position close to the center of gravity of the tip.

The spanwise extent of the blade tip was optimized with the help of a parametric analysis, considering a trade-off among blade root load alleviation, loading at the hinge and impact on power capture.

The wind turbine is operated with a variable-speed pitch-torque control strategy, including the partial load regime (or region II) from cut-in to rated speed, and the full load regime (or region III) from rated to cut-out [64]. The best possible aerodynamic performance is sought in region II to optimize power capture. Therefore,

the mean misalignment of the tip with respect to the rest of the blade should be as small as possible not to negatively affect the rotor efficiency. On the other hand, an excess of power is available in region III, so that a mean misalignment of the tip is permissible in this case as it would be readily compensated by the control system without incurring into any AEP loss.

A torsional spring and torque preload are used at the hinge with the aim of controlling the tip response. The tip pitch dynamic equilibrium writes

$$J_\theta \ddot{\theta} + K_\theta \theta = M_p + M_a, \tag{4.1}$$

where θ is the tip pitch rotation, J_θ the tip inertia, K_θ the torsional spring stiffness at the hinge, M_p the hinge preload and M_a the aerodynamic moment. The primary device design parameters are K_θ and M_p.

The torsional spring K_θ was calibrated to limit the tip pitch oscillation amplitude. This tuning was performed by running aeroservoelastic simulations in steady and turbulent conditions for varying wind speeds spanning the entire operating range of the machine, and identifying an optimal compromise between fatigue alleviation and power loss. Although in principle the spring stiffness might be scheduled with respect to the operating condition, it was found that a constant average value was a simpler and similarly effective solution.

The tip mean misalignment is controlled by providing a torque preload M_p at the hinge. As the aerodynamic loading at the tip, and hence its mean moment at the hinge, depends on the operating condition, the preload should be varied on account of the operating point at which the machine is functioning. In the semi-passive configuration the preload is generated by an actuator, while in the passive case by a mechanical device that produces a torque in response to the centrifugal loads generated by the blade rotation. In both cases, the resulting preload at the hinge is directly related to the rotor angular speed.

A sketch of the passive and semi-passive configurations is reported in Figure 4.3.

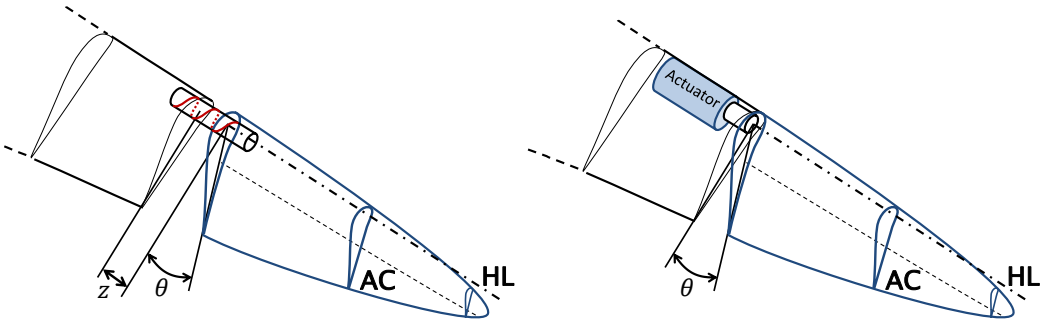

Figure 4.3: *Passive(at left) and Semi-passive (at right) tip configuration.*

As the preload is related to the operating point, its value can be computed in steady state normal wind profile (NWP) conditions using a complete aeroservoelastic model of the wind turbine, scanning wind speeds from cut-in to cut-out. To speed up the identification of the necessary preload value, at each wind speed a simulation was run where the relative rotation in the tip hinge was set to zero. Once the

solution had settled onto a periodic cycle, the mean value of the resulting torque in the hinge was used as the preload value for that operating condition.

In principle, the preload could be scheduled with respect to the mean wind speed or to the rotor angular velocity. The former option is more complicated and possibly less reliable because it requires an observer to estimate the rotor-equivalent wind speed. On the contrary, scheduling the preload with respect to the rotor angular velocity is simpler, since measurements of the rotor speed are available on board wind turbines. As the angular velocity is constant in region III, a constant preload above rated wind speed will results in a non-null mean misalignment of the tip. This is not a problem, as there is a power excess in this condition, so that a less efficient rotor does not pose any concern. The situation would be different for a machine with a transition region II1/2 in between regions II and III —which happens whenever the rotor speed hits its upper limit before rated power is reached—, where scheduling with respect to rotor speed alone might incur in power losses.

For the semi-passive configuration, an actuator applies the necessary preload torque at the hinge based on a look-up table storing the load-rotor speed map $M_p = M_p(\Omega)$ obtained in the previously described analyses, where Ω is the rotor angular velocity. No feedback regulation is involved, and the actuator simply uses the filtered (to remove fast fluctuations and noise) rotor speed as feedforward information.

The passive configuration uses centrifugal forces caused by the rotor angular rotation to generate the necessary preload M_p, without using active components. To this end, in this study the mechanical device described in [12] is considered, characterized by a screw joint that relates any linear displacement z of the tip parallel to its hinge axis to a corresponding rotation θ about the same axis, i.e. $z = \tau\theta$, where τ is the screw joint helical pitch or transmission ratio. The actual mechanical design of this device is beyond the scope of this study, and its characterization is here limited to the evaluation of its parameter τ. The passive tip pitch dynamic equilibrium can be written as

$$J_{PT}\ddot{\theta} + K_{PT}\theta = \tau\left(F_c + F_g\right) + M_a, \tag{4.2}$$

with

$$J_{PT} = J_\theta + \tau^2 m, \tag{4.3a}$$

$$K_{PT} = K_{PT\theta} + \tau^2 K_z, \tag{4.3b}$$

where J_{PT} and K_{PT} are the total inertia and torsional stiffness of the passive tip device. These include the proper inertia of the tip J_θ and the hinge spring $K_{PT\theta}$, in addition to terms contributed by the screw joint, m being the tip mass and K_z the screw linear displacement stiffness. In Eq. (4.2), F_c and F_g are the centrifugal and gravitational forces, respectively, projected into blade spanwise direction. To a first approximation, the effects due to blade out-of-plane and in-plane motion, as well as the contributions of rotor cone and tilt angles are neglected. Therefore, the centrifugal force is expressed as

$$F_c = m\,(r + z)\,\Omega^2, \tag{4.4}$$

where r is the radial position of the tip center of gravity. Inserting Eq. (4.4) into Eq. (4.2), one gets

$$J_{PT}\ddot{\theta} + \left(K_{PT} - m\tau^2\Omega^2\right)\theta = \tau m r\Omega^2 + \tau F_g + M_a. \tag{4.5}$$

The gravitational force writes

$$F_g = mg\cos\psi, \tag{4.6}$$

where ψ is the blade azimuthal position and g the acceleration of gravity. Since F_g is a periodic disturbance with zero mean over a revolution, the transmission ratio τ is chosen such that the first term on the right hand side of the equation balances the aerodynamic moment at the hinge line, leading to:

$$\tau = -\frac{M_a}{mr\Omega^2}. \tag{4.7}$$

An average value of M_a over the most likely operating conditions (between 7 and 9 m/sec, according to the used Weibull distribution) is used to compute τ.

The value of the hinge spring stiffness for the passive tip case was set by requiring this device to have the same modal frequency of the semi-passive case, which is readily computed from Eq. (4.1) as $\omega_{SP}^2 = K_\theta/J_\theta$. By setting $K_z = 0$ and using Eq. (4.5), one gets

$$K_{PT,\theta} = \omega_{SP}^2 J_{PT} + m\tau^2\Omega^2 \approx \omega_{SP}^2 J_{PT}, \tag{4.8}$$

where the term depending on angular velocity was dropped because negligible. This choice results in a hinge stiffness that, conveniently, does not depend on the operating condition, as in the semi-passive case.

It should be stressed that this is not the only possible criterion to determine the hinge spring stiffness for the passive tip case. In fact, the tip mode could in principle be placed anywhere in the spectrum, as long as it does not create resonant conditions with the 1xRev harmonic excitations and with other natural frequencies of the machine. On the other hand, the present approach seemed to work well in practice. In fact, raising this frequency by increasing the spring stiffness, limits the tip pitch oscillations, in turn reducing its authority. The opposite approach of lowering the frequency by softening the spring has the effect of increasing the disturbance caused by gravity. In fact, gravity cyclically pulls on the blade tip, creating a radial displacement that, through the screw joint, induces a pitch rotation, which in turn creates a 1P disturbance. The present approach was found to provide a good compromise between these two contrasting requirements, although a further fine tuning of the parameters is probably still possible.

4.1.2 Reference wind turbine and simulation environment

The blade tip devices are sized and studied with application to the 10 MW RWT. All simulations are performed with an aeroservoelastic model of the wind turbine implemented with the flexible multibody program `Cp-Lambda` (see [65] and references therein). The baseline regulation strategy is provided by an external library implementing the control routines reported in [66]. Based on a parametric study,

the spanwise tip length was set to 15% of the blade length, while the tip hinge line was located at 19.7% of the local blade chord from the leading edge. The tip is connected by a revolute joint to the rest of the blade for the semi-passive and active configurations. In both cases, the hinge rotation is driven by an actuator, modelled as a second order system. For the passive case, the tip is connected to the blade by a screw joint. In all cases, tip excursions are limited to ±20 deg by unilateral contact conditions in the joint. The aerodynamic model is based on standard BEM theory. This limits the computational time and allows a broadband examination of the load conditions encountered in the operative range. This approach neglects the mutual induction between the blade sections, therefore it is not able to model the shed vortex at the blade-tip junction [67]. This vortex induces a velocity field that modifies the orientation of the lift vector on the tip, causing a variation of induced drag that can affect the overall rotor performances [68]. Since the aerodynamic forces are influenced by the induced velocity, further differences are expected on the tip motion too. This can be considered one of the main approximations introduced in the reported approach and it will be investigated in the future if the passive tip concept will prove to be a potentially effective solution.

4.1.3 Sizing of the passive and semi-active solutions

The wind turbine operating range is first analyzed in NWP conditions [39]. The associated rotor speed and blade pitch settings vs. hub-height wind speed are shown in Figure 4.4.

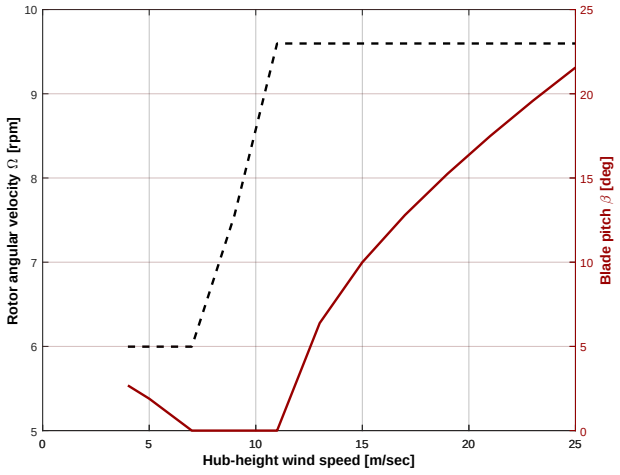

Figure 4.4: *Rotor speed Ω and blade pitch β vs. hub-height wind speed V.*

Nominal values of the torque preload M_p as a function of wind speed were obtained by constraining to zero the tip rotation at the hinge, and measuring the resulting internal moment. The result is shown in Figure 4.5 at left, using a dash-dotted line: by prescribing this preload at the hinge, one would obtain a zero mean misalignment of the blade tip. Since both for the passive and the semi-passive configurations the preload is adjusted based on rotor speed, this reference preload can

be followed only between 7 m/sec and rated wind speed, when indeed the rotor speed changes (see Figure 4.4). Despite the tip activity in region II could threaten the AEP, the appended devices are always active in power production conditions, aiming at the identification of the maximum performance. The AEP will be monitored to measure the interaction effects between tip and trimmer controller and to highlight the variation of the power production.

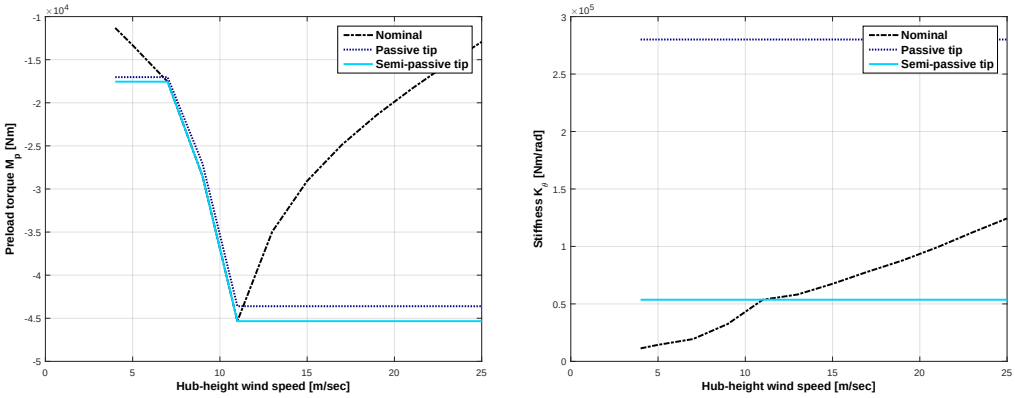

Figure 4.5: *Preload M_p at the hinge line vs. hub-height wind speed at left. Hinge stiffness K_θ vs. hub-height wind speed at right.*

As shown in the figure, for lower and higher wind speeds the actual preload provided by the passive and semi-passive solutions remains constant, implying that the blade tip will have a non-zero mean pitch offset with respect to the blade. The preload can be actively changed by a torque actuator in the semi-passive tip solution, so that the provided preload exactly follows the nominal one in this case. For the passive configuration, the preload is obtained by a constant transmission ratio τ connecting tip spanwise displacements with tip pitch rotations, which, as shown in the figure, still approximates very well the nominal preload behavior.

Figure 4.5 shows at right with a dash-dotted line the hinge spring stiffness that would result in a ±10 deg oscillation of the tip in NWP conditions. As this stiffness changes little with respect to wind speed, it was approximated with a constant value for the semi-passive case, further tuned with the help of turbulent analyses. From a practical point of view, a constant spring stiffness if useful because it reduces the complexity of the device. As previously explained, the hinge stiffness for the passive configuration differs from the one of the semi-passive case. In fact, since the transmission ratio of the screw joint increases the torsional inertia of the blade tip, the hinge stiffness was increased to keep the tip mode at the same frequency in both solutions.

Table 4.1 reports the modal frequencies of the rotating blade in a vacuum at rated speed, for the baseline blade and the semi-passive and passive solutions. Minor differences are due to the adoption of a constant transmission ratio τ, which however is important for the simplicity of the device. The blade tip mode is clearly distinct from the lower blade frequencies, limiting the risk of aeroelastic interactions.

Table 4.1: *Modal frequencies of the rotating blade in a vacuum (in rad/sec).*

Mode	Baseline	Semi-passive tip	Passive tip
1^{st} flap	4.08	3.99	3.99
1^{st} edge	5.67	5.40	5.39
2^{nd} flap	10.3	10.9	10.8
2^{nd} edge	15.6	16.0	15.9
3^{rd} flap	20.0	21.9	21.9
Tip mode	-	25.2	25.1
3^{rd} edge	31.2	33.0	32.6

4.1.4 Active configuration

Besides the passive solutions described earlier, tips can also be used for active feedback control. In that case, pitch motions are actively driven by tip actuators. Due to the lower inertia of the tip with respect to the entire blade, tip based active control might have a higher bandwidth than full-span pitch control. In addition, as the tip has a high moment arm with respect to the blade root, even relatively small changes in the aerodynamic loads might have significant repercussions on the overall loading of the rotor. Both of these effects might be especially visible for larger turbines, although a detailed investigation of scale effects is beyond the scope of the present work.

In this study, cyclic pitch control of the tips is used for the reduction of rotor moments in the fixed system, using a formulation similar to one used for classical full-span IPC [48, 69–72]. Blade bending moments are measured by load sensors at the blade roots, and transformed first into out-of-the-rotor-plane moments, and then into direct M_d and quadrature M_q moments in the fixed frame by the Coleman transformation [73].

After filtering to remove frequencies at and above 1xRev, reference loads are subtracted from the Coleman-transformed moments, yielding the delta-loads used for feedback $\Delta M = M - M^*(\bar{V})$ for both the q and r components, where $\bar{V}$ is a slowly varying moving-average of the wind speed used for scheduling the reference loads. The use of delta-loads is useful because of the lower authority of tip pitch control compared to full-span pitch control. In fact, by cyclically pitching the whole blade, full-span pitch control can very significantly reduce the mean value of fixed frame loads, which is typically not possible with the sole use of tips.

A proportional-integral (PI) controller is then formulated in the fixed frame, giving

$$\beta = k_P \Delta M + k_I \int_0^t \Delta M \, \mathrm{d}t, \tag{4.9}$$

where k_P and k_I are the proportional and integral gains, respectively. The same control law is used for the direct and quadrature components, yielding both the β_d and β_q control inputs in the fixed frame, which are finally transformed back into the rotating system via Coleman's inverse transform.

This IPC formulation results into a 1xRev tip pitch input activity. Higher frequency Coleman transformations could be easily used within the exact same tech-

nique [74] to obtain a higher-harmonic controller. In fact, given the reduced inertia of an active tip device, a wider bandwidth control activity could be more easily achieved than using full-span pitch control, especially for very heavy and large blades.

However, a fatigue analysis performed on the reference wind turbine considered in the present study revealed that fatigue is primarily generated in a very low range of frequencies. In fact, Figure 2.8 reports the normalized blade root lifetime bending moment damage equivalent load (DEL) as a function of load harmonics for the baseline RWT. It appears that DEL increases very rapidly with frequency, to the point that already 75% of damage is accumulated for frequencies up to 1xRev. Damage then rapidly levels off, with very little contributions coming from frequencies above the 3xRev. For this reason, and given the preliminary nature of the present study, it was decided to limit here the tip control activity to the sole 1xRev harmonic.

4.1.5 Tuning of the active tip control law

Tuning of the cyclic tip pitch controller involves setting the reference values for the direct and quadrature loads, as well as the proportional and integral gains.

Figure 4.6 shows the M_d and M_q values vs. wind speed for the baseline wind turbine without tips, using dash-dotted lines. The same figure also shows the reference values M_d^* and M_q^*, using dashed lines. These values were chosen by trial and error and, as previously explained, aim at lowering the feedback loads due to the reduced authority of a tip compared to a full-span pitch control solution.

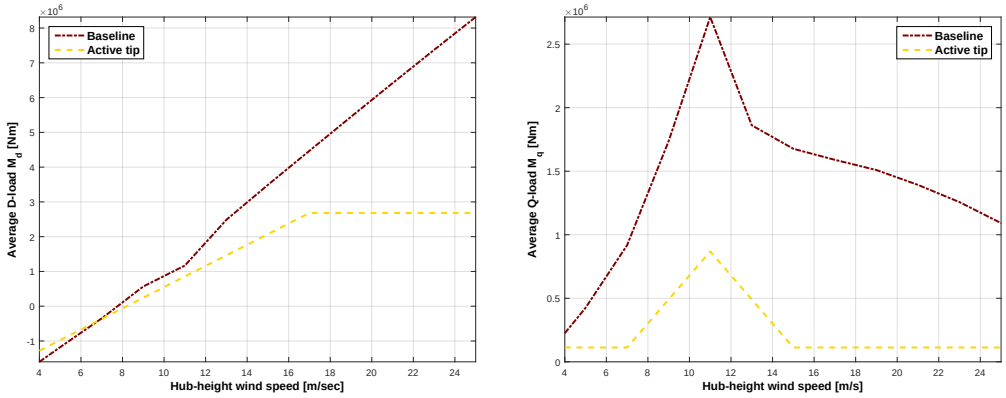

Figure 4.6: *Average M_d load (dashed line) and references value M_d^* (dash-dotted line) vs. wind speed.*

The tip controller was tuned using turbulent wind conditions (DLC 1.1, [38, 39]). Gains were set in order to achieve satisfactory performance on hub loads while at the same time avoiding excessive actuator motion, which would result in disadvantageous in ADC. The performance of the controller has been checked with respect to the most requiring condition (DLC 1.3). A simple gain scheduling was used to further boost performance, by multiplying the gains by a factor of four around rated, and specifically between 9 and 11 m/sec. Due to the lower loads sustained by tip actuators compared to blade root ones, tip IPC was used over the

whole operating range of the machine, and not only in region III as customarily done for full-span blade IPC.

Both the reference loads and gains were scheduled using a 30 sec moving-averaged wind speed measured from the nacelle anemometer. Fixed frame loads were low-pass filtered with a fourth order Butterworth filter with a cut-off frequency of 0.1 Hz.

4.2 Results

The performance of the proposed tip devices was evaluated by studying the wind turbine in different operating conditions, as recommended by international certification standards [39]. Of all various DLCs used to design the machine [37], the most demanding ones in terms of fatigue and ultimate loads were selected. In turbulent wind conditions, results were averaged over four different realizations corresponding to different seeds [63].

4.2.1 Standard design conditions

The standard power production range was simulated by DLC 1.1 from the cut-in to the cut-out speeds in 2 m/sec increments. The AEP percent variations with respect to the baseline configuration without tip devices are reported in Figure 4.7. Apparently, the active tip device has the largest impact on energy capture, possibly due to the choice of operating it also in region II. The maximum AEP reduction is equal to 0.5% and it can not be neglected because it could nullify the advantages due to the load alleviation. Further studies that involve the updating of the wind turbine aerostructural properties are required to combine the variation of the AEP with loads reduction in a single CoE value.

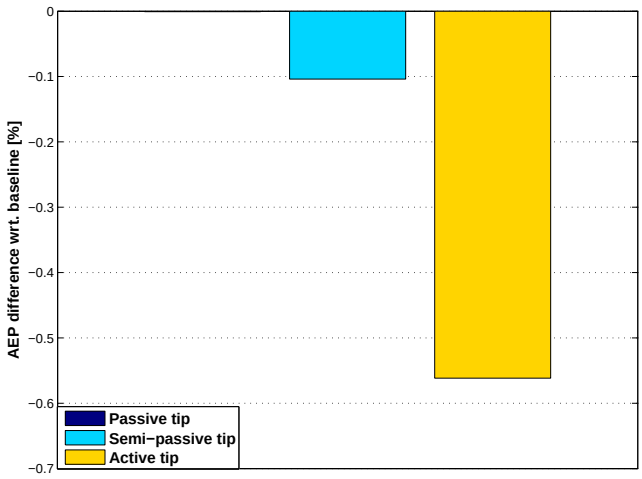

Figure 4.7: *Percent AEP variation with respect to baseline configuration.*

DELs were evaluated at a number of spots on the machine based on Rainflow-counting. The blade, main bearing and tower base were selected as fatigue verifica-

tion spots because they are indicative of possible structural regions prone to fatigue problems. DELs corresponding to the combined moment at the most damaged point at each verification section are reported in Figure 4.9.

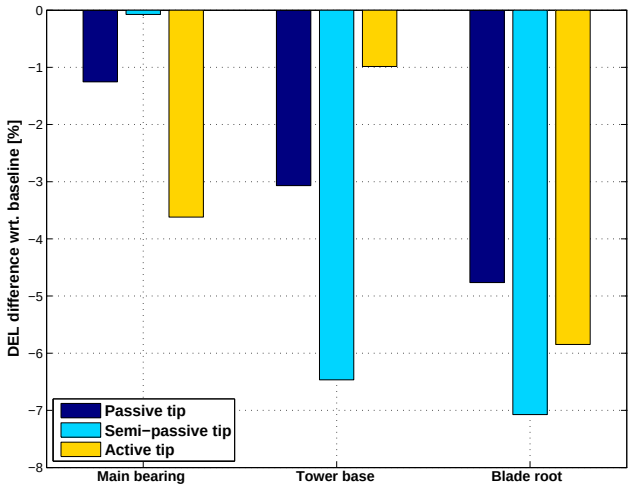

Figure 4.8: *Percent variation of DELs at verification spots.*

The effects of the appended devices at the blade root, main bearing and tower base are shown in the top part of the figure. All three tip devices appear to be lowering fatigue loads, although to a different extent at different verification spots. The active tip achieves the best load reduction at the main bearing, because those are indeed the loads targeted by the tip IPC control algorithm. On the other hand, it is interesting to observe that the passive and semi-passive tips perform better than the active configuration at tower base, where the DEL is mainly due to rotor thrust. In fact, these results seem to indicate the ability of the passive and semi-passive tips to smooth out load fluctuations due to turbulence. As the three tips operate independently, in contrast with the centralized operation of the IPC algorithm, they are better able to locally react to local wind fluctuations, in turn resulting in smaller fatigue damage at tower base. The effects at blade root are also significant, the semi-passive achieving the best results, followed by the active tip, and finally closely followed by the fully passive configuration.

However, a more detailed analysis of blade fatigue reveals significant differences among the three solutions, as shown in the bottom part of Figure 4.9. In particular, the plot of DEL vs. blade span shows that the passive and semi-passive solutions reduce fatigue throughout the whole span of the blade, which again indicates the ability of the tips to smooth out aerodynamic loads. On the contrary, the active tip lowers fatigue towards the root, but increases it at the tip. This is due to the commanded pitch activity that, with the final goal of lowering nodding and yawing moments at the main bearing, in reality overloads the blade tip. Usually fatigue may become a design driver in the inner portion of the blade, so the increase in DEL towards the tip might not be a major source of concern. Nevertheless, a rise of fatigue damage in the tip region should be expected during blade design and would

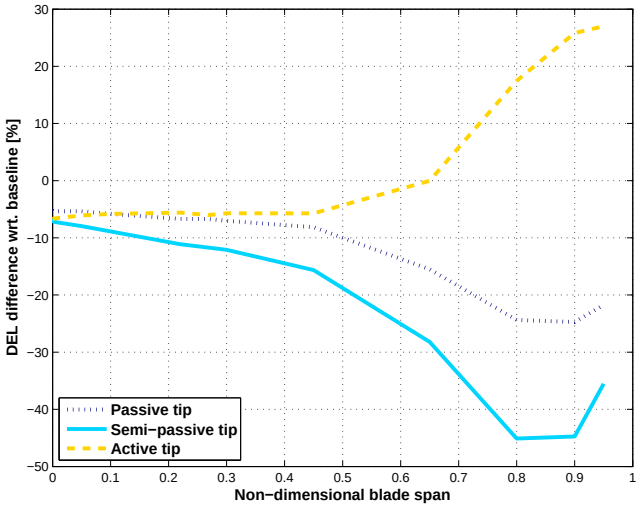

Figure 4.9: *Percent variation of DELs vs. blade span.*

have to be considered.

Collective pitch activity performed by the controller governing the machine [66] is reported in Figure 4.10 in terms of actuator duty cycle (ADC) vs. hub-height wind speed, where ADC over a time span T is computed as

$$ADC = \frac{1}{T}\int_0^T |\dot{\beta}|\mathrm{d}t. \tag{4.10}$$

Differences are modest, with some reduction noticeable for the semi-passive solution. This can be attributed once again to the smoothing of the airloads performed by this device, which in turn yield a smoother response of the machine and a consequent slightly reduced activity of the controller in reaction to wind fluctuations.

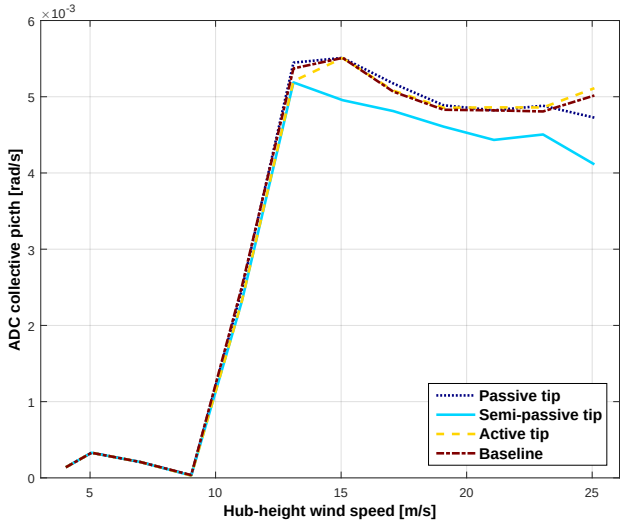

Figure 4.10: *Blade pitch ADC vs. hub-height wind speed V.*

Figure 4.11 shows the tip ADC vs. wind speed. For the passive and semi-passive solutions, ADC is only a measure of how much the tip pitches in response to load fluctuations, while for the active case it represents a measure of the control effort performed by the actuator. The plot shows that the three devices have very roughly similar tip activities, although these are in nature quite different, as shown by the previous load analysis. In addition, it appears that the semi-passive device has a more pronounced activity than the passive one.

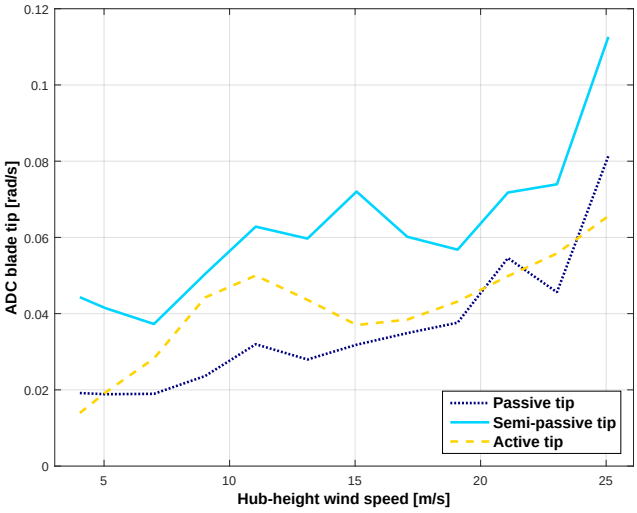

Figure 4.11: *Tip ADC vs. hub-height wind speed V.*

An ultimate load analysis was performed by considering a selected set of DLCs. DLC 1.1 and 1.3 consider power production in standard and extreme turbulence conditions. In DLC 2.3, a deterministic gust occurs in conjunction with a grid loss, and the effects of the fault time are examined by multiple simulations. Finally, DLC 6.2 considers parked conditions with grid failure, where multiple yaw conditions are considered to identify the worst scenario.

Attention is focused on the combined bending moments at blade root, main bearing and tower base, and percent variations of the ultimate loads with respect to the baseline are reported in Figure 4.12. Better performance is achieved at the main bearing and at blade root, where the most demanding situations are due to DLC 1.3. Here again, as in the case of fatigue damage, the tip devices seem to be able to smooth out airloads, with a beneficial effects also on peak loads.

The situation is different for ultimate loads at tower base, which are due to DLC 6.2. Although in this case tip oscillations do not in general help in reducing loads, the ability of the active and semi-passive solutions to deflect the tip can be used to gain a modest advantage. In fact, by pitching the tip one may reduce the sail area of the blade, which in turn may somewhat reduce loads during storms. For these two cases, tips were pitched all the way to their stop positions (20 deg). As shown by the figure, this strategy results in a modest decrease of loads at tower base. This active protection of the rotor in storm conditions is not possible with the fully passive solution, where the tip is free to float into the wind but cannot be controlled

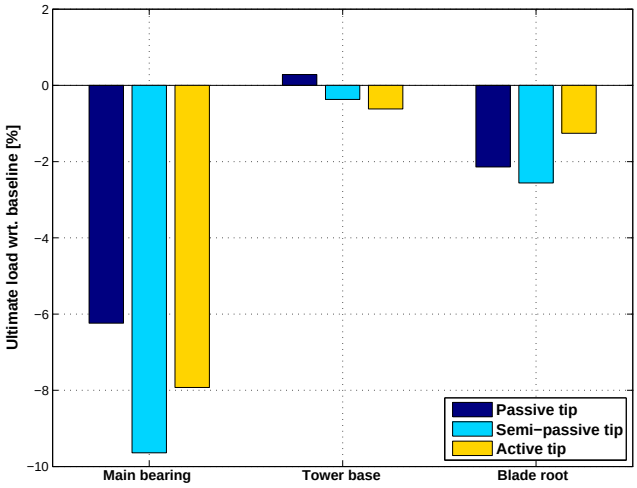

Figure 4.12: *Percent variation of ultimate loads at verification spots with respect to baseline.*

directly. The same figure shows that this has a very modest negative effect on tower loads.

4.2.2 Off-design conditions

The effects of a blade tip failure are investigated to understand if the advantages of the proposed tip devices can be offset by a fault of the tip pitching system. The fault is investigated by blocking the relative rotation of a single blade tip, while the other ones are functioning in a regular way. It is supposed that the wind turbine is equipped with a safety system to detect the fault and trigger an immediate shut down procedure. Generator fault or loss of electrical network are not included in the fault scenario, because simultaneous malfunctions are considered as very unlikely.

Blade tip faults are examined using DLC 2.1 and 2.3 to identify the most critical condition. A single seed is considered for DLC 2.1 NTM simulations because the relative position of the fault with respect to wind fluctuations is more important than the analysis of different wind realizations. The blade tip fault is imposed in conjunction with a positive steep gradient or a maximum of the hub-height wind speed. These two conditions are respectively labeled “grad” and “peak” in the following. When turbulent winds are considered, each simulation is associated to a number, which represents the mean hub-height wind speed, and a letter, identifying a turbulent seed. DLC 2.3 simulates a deterministic extreme operating gust (EOG) at cut-out (labelled vo), rated (labelled vr) and rated ±2 m/sec (labelled vr±2) wind speed. In total, 16 simulations were performed at each wind speed, varying the time interval between the gust and the fault as well as the azimuthal position of the faulty blade tip. Each simulation is identified by a number that refers to one of these combinations.

The off-design performance is investigated by ranking the ultimate loads of the standard envelope plus the fault conditions in decreasing order, and monitoring the variation of the maximum load magnitude. The first three ranking combined mo-

ments at the main bearing are reported for each configuration in Figure 4.13, where the fault conditions are identified by using gray-shaded bars.

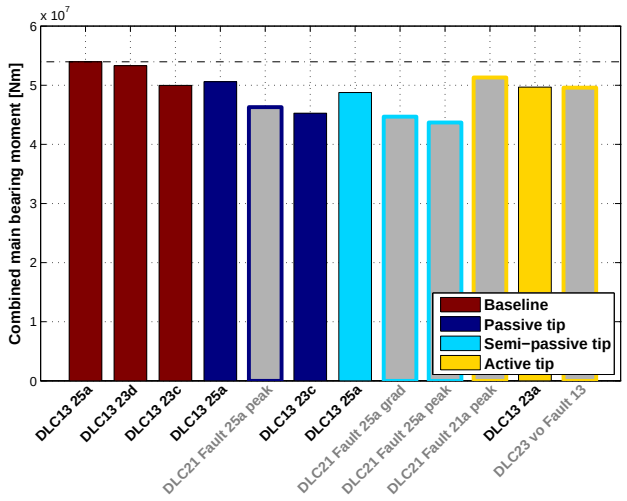

Figure 4.13: *Ranking analysis of main bearing combined moment. Blade tip fault conditions are displayed using gray-shaded bars.*

A blade tip failure is considered dangerous if the maximum load magnitude increases with respect to the baseline configuration. The ranking analysis for blades and tower base are not reported here, because fault conditions do not modify the highest five ranking loads. In fact, DLC 1.3 remains the load case driving blade design, while the tower is still stressed by DLC 6.2. On the contrary, the combined moment at the main bearing is affected by the rotor imbalance caused by the blade tip fault. Therefore, off-design conditions may generate loads that are comparable, or even higher, than in the non-faulty standard DLCs.

The results reported in the figure show that all tip devices do not exceed the load envelope of the baseline machine. In addition, fault conditions are not load drivers for the passive and semi-passive solutions, while they produce the leading load for the active tip case. This might be due to the loss of coordination of the blade tip movement that follows a tip fault.

4.3 Synopsis

A movable blade tip concept for load mitigation on wind turbines has been investigated in this chapter. The device allows for a relative pitching motion of the blade tip with respect to the rest of the blade, introducing a further control capability. A passive solution, which appears to be very interesting at the light of lessening the complexity of the system, was compared with semi-passive and active blade tip architectures.

Based on the results of the present analysis, the following conclusions may be drawn:

- All proposed tip devices improve on the baseline both in terms of fatigue and

ultimate load alleviation, although to a different extent on different wind turbine components. These results might possibly be further improved by a more complete optimization of the devices, including their aerodynamic shape.

- The more significant effects on fatigue are reported at the blade root and tower base. For the passive and semi-passive devices, this seems to be attributable to a smoothing of the airloads. Ultimate loads see the largest decrease at the main bearing, while they are essentially unaffected on blade and tower.
- None of the devices seems to significantly interfere with the collective pitch/-torque control system used for regulating the machine, although no re-tuning of the controller was performed. For the semi-passive solution, the load smoothing generated by the tip results in a slightly reduced duty cycle of the blade pitch actuator.
- The consequences of a blade tip fault are limited, with no effect on the ultimate design-driving loads. The active and semi-active devices can be used to reduce blade sail area in storm conditions. Although this technique did not reduced ultimate loads on this specific machine, it might be beneficial on other wind turbines more significantly driven by storm conditions.

Part II

FULL BLADE SPAN SOLUTIONS

CHAPTER 5

Realization and structural characterization of scaled multi-MW aeroelastic blades with bend-twist coupling

5.1 Introduction and motivation

This chapter describes the realization and the structural characterization of scaled aeroelastic blades with bend-twist coupling (BTC) capability. The BTC is a full blade span solution with very interesting potential in reducing the fatigue loads on the main spots on multi-MW wind turbines, since when the blade bends because of increased loads, the consequent twisting reduces the airfoils angle of attack thereby affecting the aerodynamic loads. This form of load mitigation can be obtained by exploiting the anisotropic mechanical properties of composite materials, like using off-axis fiber angles, and the literature [31, 32] clearly shows the potential benefits of BTC. This solution is also very attractive because of its passive nature: there are no actuators which may fail, no moving parts which may wear out, all characteristics that are very interesting for wind energy systems, where simplicity, low maintenance and high availability are key for reducing the cost of energy. To this end, ad-hoc multi-level design tool is developed, then a dedicated manufacturing process is set-up. Since their low intrusivity, Fiber Bragg Grating sensors (FBGs) are installed on the blade within two spar layers, in order to acquire the blade load at a certain spanwise position. The resulting blades were tested at bench. Test with hammer is performed to characterize the dynamic behaviour and verify the compliance to the scaling requirements, while static tests are used to characterize the distributed stiffnesses and the amount of BTC. The tests are used to seed the

identification procedure for blade structural properties estimation.

The chapter is organized according to the following plan. First, the design of the aeroelastic blades with BTC is described, with the choice of the scaling law, the aerodynamic design of the blades with the choice of the airfoils, the layout and the technology solution identified for the realization of the blade structure, the multi-level optimization tool used for the blade design. Then the manufacturing process is detailed, including all the necessary steps for the final realization. Finally the dynamic and static tests on the realized blades are described, together with the identification method used for evaluating the distributed structural properties.

5.2 Design of scaled rotor with bend-twist coupling

It is known that the non-dimensional parameters that drive the dynamics of the wind turbines are the tip-speed-ratio $\lambda = \Omega R/V$, where Ω is the angular speed of the rotor of radius R and V the wind speed, Reynolds number $Re = \rho V c/\mu$, where ρ is the density, c is a characteristics length and μ is the fluid viscosity, the Froude number problem $Fr = V^2/gR$, where g is the acceleration of gravity, the Mach number $Ma = V/a$, where a is the sound speed, and the Lock number $Lo = Cl_{/\alpha}\rho c R^4/I$, where $Cl_{/\alpha}$ is the slope of the lift curve and I is the blade flapping inertia, as well as the non dimensional natural frequency $\tilde{\omega}_i = \omega_i/\Omega$ and non dimensional time $\tau = \Omega t$, with t the indicating time. A perfect scaling would involve the matching of all the aforementioned non-dimensional parameters. Nevertheless, it is readily demonstrated that this ideal situation can never occur. Hence, there isn't a unique criterion to be followed for a correct scaling, but instead, the method should be set-up in order to fulfill some driving requirements that depend on the application and on the field where the model will be tested. The method used here is based on the loose scaling criteria derived by [36] that required the exact-matching of the aerodynamic kinematics, i. e. the same tip-speed-ratio, the exact-scaling of the structural dynamics, i. e. the same non-dimensional natural frequencies, and the enforcement to have the same ratio between the aerodyanamic and inertial properties, i. e. the same Lock number, which amounts to have the same scaled aeroelastic stiffness properties.

5.2.1 Aerodynamic design

The rotor model was design to be a loose scaled-representation of a multi-MW machine. To understand the designing solutions for the aerodynamics of the scaled blades, additional considerations should be taken in mind. First, due to the fact that the tests are conducted in a wind tunnel, the finite dimensions of the test chamber constraint the rotor diameter. Additionally it may introduce wake important blockage affects with the increasing of the rotor dimensions. Second, the limiting of the rotor dimensions would require a scaleing-up of the time in order to satisfy the scaling requirements, and therefore the control bandwidth must also be scaled-up which could lead to consequent excessive increase of the actuators' workload. Third, limiting the scaled-up bandwidth and velocity, together with the limited rotor dimensions, leads to an unavoidably high mismatch with the reference full-scaled ma-

chines in terms of Reynolds number, that changes the physics of the fluid-structure interactions and therefore reduces the energy conversion quality.

Table 5.1: *Scaling factors for the model characteristics with respect to multi-MW reference wind turbines*

	SF	**RWT 2MW**	**RWT 5MW [40]**	**RWT 10MW [41]**
Length	n_l	1 : 48.09	1 : 65.87	1 : 93.25
Rotor Speed	n_Ω	25.3 : 1	31.4 : 1	39.5 : 1
Wind Speed	$n_l n_\Omega$	1 : 1.90	1 : 2.10	1 : 2.36
Rotor Power	$n_l^5 n_\Omega^3$	$1 : 1.58 \cdot 10^4$	$1 : 4.00 \cdot 10^4$	$1 : 1.14 \cdot 10^5$

The previous considerations bring at the following driving requirements for the scaling:

- Rotor dimensions not excessive, to limit blockage effects due to the interference with the wind tunnel walls, but large enough not to lower too the Reynolds number. Past experience shows a good trade off value of the rotor diameter as ≈ 2 m.
- The scaling-up of the time to avoid an excessive increase in the pitch control bandwidth and a reasonable rendering of the principal dynamic effects of servo-actuators, mainly due to time delays and maximum attainable rates. For this purpose, the nominal rotor speed is chosen equal to ≈380 rpm, which translates in Re around $4.5 \div 6.5 \cdot 10^4$.
- A realistic energy conversion process, which translates into the same full-scale and model aerodynamic kinematics (i.e. same tip-speed ratio) as well as into realistic aerodynamic thrust and power. For this purpose, the blade is designed using special airfoils developed for Reynolds around 5-60000 and equipped with transition strip. The AH79-100C [75] and WM006 [76] profiles were used, with the former airfoil extending for $\eta \in [0.146, 0.451]$ and the latter for $\eta \in [0.697, 1]$. The choice of such airfoils is suggested by their capability in providing good aerodynamic performance at low Reynolds number [36]. In the blade inner region, the inboard airfoil is smoothly deformed into the blade root cylinder, which extends for $\eta \in [0.0, 0.021]$.

To account for the limitations induced by the scaling, the following expedients are also considered:

- the chord distribution is selected accordingly to have Reynolds number around 5-60000 for a large part of the span, that, with the chosen airfoils, guarantees good performances in terms of aerodynamic thrust and power coefficients. At the same time a resonable rotor solidity according to the reference multi-megawatt machines is also provided;
- to account for the choice of the airfoils and for the chord length distribution, the twist was accurately chosen in order to have an optimal axial induction distribution.

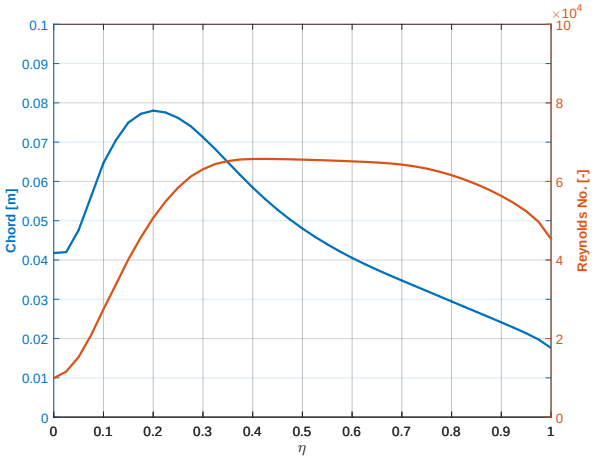

Figure 5.1: *Chord and airfoils Reynolds distribution for the designed blade*

Figure 5.1 shows the chord and Reynolds distribution at rated rotor speed (380 rpm). To validate the aerodynamic design, a set of three blades with high stiffness properties and high natural frequencies, with the chosen aerodynamic shape are manufactured in carbon fiber, then tested in the wind tunnel. The results are shown hereinafter in Chapter 6.

5.3 Structural design of the scaled aeroelastic blade

5.3.1 Blade layout

The realization of the aeroelastic blades is a complex challenge. The design process should identify optimal structural layout, choice of materials and sizing of the structural members to ensure the fulfillment of the requirements. According to the scaling, the shape of the blade passes from the root cylinder of diameter around 40 mm to airfoils whose thickness is around 1-2 mm. The required total mass is about 50 g, while the first flap-wise frequency is slightly greater than the 3xRev.

Modern wind turbine blades are typically realized with a D-spar structure: a carrying-box made up of two shear webs connected to the spar-caps, which are made of epoxy resin reinforced with glass fiber and/or carbon fiber and designed with the primary function of withstanding the aerodynamic and inertial loads, while an external shell, usually made of epoxy resin reinforced with glass fiber, provides the necessary torsional stiffness and gives the desired aerodynamic shape to the blade.

Since the goal is producing a scaled version of a multi-MW machine, the most obvious solution would be to directly scale all the structural elements using the ratios of Table (5.1). This would involve scaling the blade geometry, as well as the structural thicknesses, with the factor $n_l \approx \frac{1}{50 \div 100}$ and using materials whose Young's modulus is scaled with the factor $n_l^2 n_\Omega^2 \approx \frac{1}{5 \div 10}$. This solution appears to be unfeasible because the scaling of the original structural elements would require the manufacturing of components whose thicknesses would be in the order of a few

hundreds of microns, resulting in huge technological complications, as well as high fragility and difficult handleability of the manufactured components.

It is therefore necessary to identify a specific and innovative solution for the problem at hand. The manufacturing process should guarantee a certain level of controllability and reproducibility, in order to guarantee the production of same blades that should, all, fulfill the following requirements:

- The external shape should be consistent with the rotor model geometry and with good surface finishing, to guarantee a realistic energy conversion process;
- The bending stiffness consistent to the one specified by the scaling factors, together with a blade mass distribution and external shape such that requirements on the placement of the blade natural frequencies and of the Lock Number are fulfilled.
- The manufacturing process should allow the embedment of Fiber Optic Sensors (FOs) in desired positions inside of the blade structure .

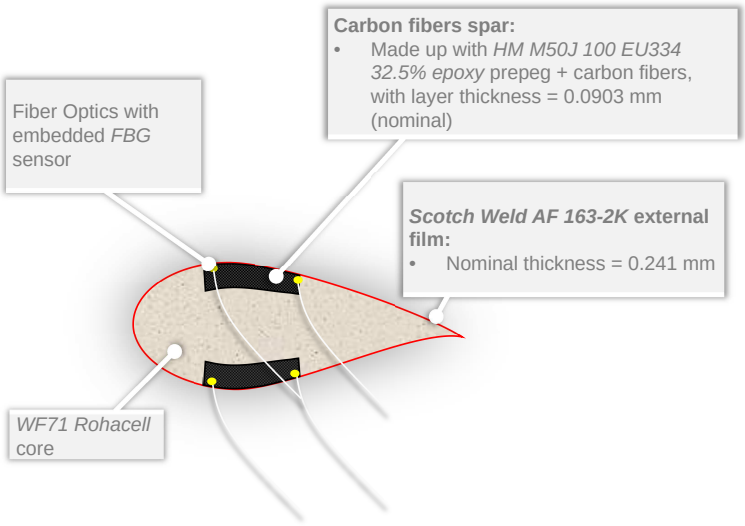

Figure 5.2: *Blade layout*

The blade layout is shown in Figure 5.2. Similar to applications descibed in [77] and [78], a Rohacell® [79] core is used to avoid any deformation of the airfoil's shape due to the forces exerted by the aerodynamic pressure. Instead of the more classical D-configuration, two properly sized composite spars are selected and located far from the airfoil mean line, in order to obtain adequate flap stiffness. The spars are made of non-symmetric and non-balanced stacking sequences of UD carbon fibers reinforced prepregs, thus provide the desired bend-twist coupling and guarantee a better stability to the whole blade. Finally, this solution allows FOs integration during the hand lay-up of the spars exploiting embedment techniques especially developed for composite laminates [80], which ensure high load transfer capability between FOs and host structure, low invasivity as well high accuracy of

embedded sensors. As underlined in Figure 5.2, four FOs, equipped each with one FBG sensor, are embedded from the blade root. The sensors are placed at ≈ one third of the blade span. The four application points within the section are chosen as those with higher strains (two at suction, two at pressure side), in order to maximize the sensitivity and the accuracy to the deformation shapes.

All the aforementioned requirements are achievable with this layout using a very small and predictable fraction of the blade target mass and with little increase of the torsional stiffness. The Rohacell provides the shape to the blade section, exhibits good deformability properties if subjected to conveniently high level of pressure, and resists at high cure temperature. It is necessary to pre-form the Rohacell before its inclusion in the model blade, as well as conveniently sized grooves must be realized for housing the carbon spars. In this regard, the high fragility of the material requires the use of appropriate techniques for its machining and handling during the lamination phase. Finally, an uncured polymeric layer is used to cover the blade surface and to provide good and smooth finishing by filling the Rohacell pore. Moreover, it contributes to increase the torsional stiffness with small effect in the bending directions. This solution allows one to precisely know the modest amount of mass added to the blade, which is not possible in the case, for example, of manual application of epoxy resin or similar; furthermore, during the curing process the adhesive film becomes very fluid allowing its homogeneous distribution all over the blade surface.

Material selection and characterization

The HM M50J 100 EU334 32.5% [81] uni-directional (UD) high-modulus graphite / epoxy prepreg (layer thickness equal to 0.0903 mm) is selected for the production of the carbon spars on the basis of its very high module to density ratio. With regard to the filler, Rohacell WF71 with nominal density of 71 kg/m^3 was chosen, which is a good compromise between low density and not excessive cells size. For the external skin a film of Scotch Weld®AF 163-2K [82], with nominal thickness equal to 0.241 mm was used; this epoxy structural adhesive has a curing temperature equal to that of the UD prepreg and its supporting carrier provides good drapability, which is fundamental given the complex and doubly curved blade surface, avoiding, at the same time, excessive deformation of the resin film during its application on the blade surface.

The HM M50J and AF163-2K mechanical properties were measured by performing standard tensile tests on sample coupons of the materials, following the requirements imposed by rules [83] and using a MT S793 Materials Test Machine. The measured longitudinal tensile modulus in the direction of the fiber orientation E_{11}, the tensile modulus transverse to the fiber direction E_{22}, the in plane shear modulus G_{12} and the major Poisson ratio ν_{12} of the HM M50J and AF163-2K are reported in Table 5.2.

As explained hereinafter in Section 5.4, the Rohacell core must be oversized in order to provide a sufficient level of pressure during the curing process; consequently, the material density will be much greater than the nominal one and variable along the blade span. The characterization of the Rohacell WF71 mechanical

Table 5.2: *Measured mechanical properties of the* `HM M50J` *and* `AF163-2K`.

	`HM M50J`	`AF163-2K`
E_{11} [MPa]	245019	2887
E_{22} [MPa]	5936	2887
G [MPa]	4151	1024
ν_{21}	0.324	0.41

properties is done by realizing several specimens with different density. Specimens with measured density equal to 72, 97 and 110 kg/m^3 were produced with ad-hoc molds used to compress small blocks with different thickness into the desired shape.

The specimen Young's and shear modulus are characterized as function of the temperature, using the `DMA 2980` Dynamic Mechanical Analyzer. The measured modulus are shown in Figure 5.3.

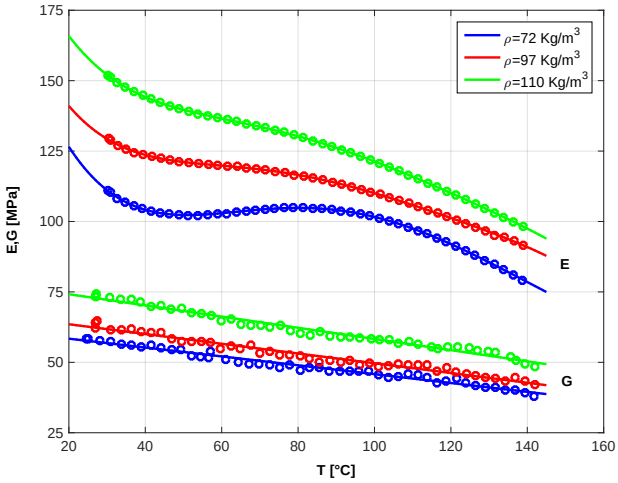

Figure 5.3: `Rohacell WF71` *modulus as function of the specimen density and temperature.*

Design optimization of the anisotropic composite structure

The problem of sizing was performed by looking at the following objectives. First, the correct aero-elastic scaling, i. e. the correct matching of the Lock Number and the lowest N_ω non-dimensional blade frequencies, i.e. $\hat{\omega}_i/\hat{\Omega} = \tilde{\omega}_i/\tilde{\Omega}$ for $i = 1 : N_\omega$, where N_ω is an appropriate number that selects all modes up to a certain frequency. Second, the anisotropic composite structure should be realized in a way of creating an effective bend-twist coupling. The bend-twist coupling is reached by rotating the carbon fibers in the spar of a certain angle θ_{spar} in order to guarantee a sufficient twist-to-feather coupling, quantified at section level with the coefficient $\alpha_s = \hat{K}_{ft}/\sqrt{\hat{K}_{flap}\hat{K}_{tors}}$ (defined as in [85], where $\hat{K}_{flap}$ is the local flap-wise bending stiffness, $\hat{K}_{tors}$ the torsional one and $\hat{K}_{ft}$ the coupled bend-twist stiffness).

The structural design of the blade is performed first without bend-twis coupling, i. e. considering the carbon fibers direction in the spar aligned with pitch axis. But

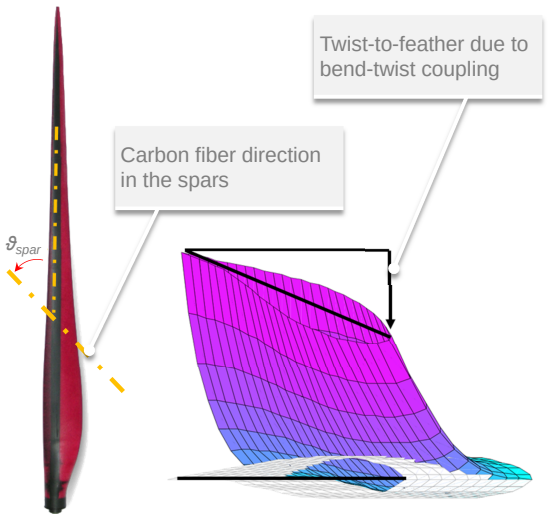

Figure 5.4: *Carbon fibers orientation with respect to pitch axis for twist-to-feather*

given the different layout between the scaled blade and the reference D-spar structure, the problem of matching many frequencies becomes hard and even impossible. On the other hand, as the final purpose is to demonstrate the capability of the bend-twist coupling in reducing the fatigue loads, it is considered enough to match only the first two flap modes and the first edge.

The structural design is made with a fast design tool that accounts for all the requirements listed and, at the same time, to capture the local effects in complex 3D structures made with anisotropic composite materials. The approach here proposed is based on the works published in [58, 84] and consists of a multi-level design procedure that conducts the design with a high level of integration and automation. Figure 5.5 illustrates the proposed multi-level constrained structural design optimization of the blade.

As a starting point, a guess configuration of the blade structure is required at section level. The primary design variables are defined at selected span-wise sections while intermediate values are interpolated using shape functions. Based on this, a beam-like multibody model of the blade is developed in the `Cp-Lambda` multibody environment, and the automatic computation of the beam eigenvalues allows the evaluation of the first three natural frequencies. The cost function is the error on the edgewise stiffness (distributed along the blade-span) with respect to the scaled reference blade. The reason associated with the use of this cost function is related to the chosen airfoils, that are much thinner than those used in the target blade, thus the achievable ratio between the blade edge-wise and flap-wise stiffness, will be greater than target one. With this cost function, the optimization problem seeks the best configuration with the minimum (unavoidable) descrepancy on the edgewise stiffness.

A 3D CAD model is then directly generated from the optimal blade geometry

which precisely accounts for all components of the blade (spar caps, external skin, `Rohacell` core and blade root insert) as well as their associated material properties and laminate characteristics. The meshing of the blade is performed with the commercial pre-processing software `HyperMesh` [86], which provides macro-based facilities for automatic mesh generation, using either shell and solid elements, and the subsequent export of the model data in the form of input files compatible with various commercial FEM solvers.

The 3D FEM model provides the framework for a fine-level verification of the design constraints, as the detailed model reveals effects that may have been overlooked by the coarse-level (multibody level) modeling. For example, local effects at regions with rapidly changing geometry in the span-wise direction cannot be correctly represented by beam models. If constraint violations are detected at the fine-level, the coarse optimization loop is repeated with constraint bounds that are tightened proportionally to the violation amount; coarse and fine-level iterations are repeated until an optimal design satisfies all the constraint conditions at the finest description level.

Coarse-level optimization

The numerical problem of finding the structural configuration to meet the design requirements was formulated as the following robust constrained optimization:

$$\mathbf{p}_s^* = \arg\min_{\mathbf{p}_s} \left\| \frac{\hat{\mathbf{K}}_{edge}(\mathbf{p}_s, D) - \tilde{\mathbf{K}}_{edge}}{\tilde{\mathbf{K}}_{edge}} \right\|, \tag{5.1a}$$

$$\text{s.t.:} \quad \mathbf{g}_s(\mathbf{p}_s) \leq \mathbf{0}, \tag{5.1b}$$

$$\left| \frac{\hat{\omega}_i(\mathbf{p}_s, D) - \tilde{\omega}_i}{\tilde{\omega}_i} \right| \leq \varepsilon_\omega \quad i = 1 : N_\omega, \tag{5.1c}$$

$$\left| \frac{\hat{Lo}(\mathbf{p}_s, D) - \tilde{Lo}}{\tilde{Lo}} \right| \leq \varepsilon_{Lo}, \tag{5.1d}$$

$$\left\| \frac{\hat{\mathbf{K}}_{flap}(\mathbf{p}_s, D) - \tilde{\mathbf{K}}_{flap}}{\tilde{\mathbf{K}}_{flap}} \right\| \leq \varepsilon_{\mathbf{K}_{flap}}, \tag{5.1e}$$

In problem (5.1), p_s are structural unknown parameters to be optimized, while D:

$$D = \{R, \text{AF}, c(\eta), \theta(\eta), \ldots\} \tag{5.2}$$

is a list of given data, i. e. the rotor radius R, the list $\text{AF} = \{\ldots, \text{AF}_i, \ldots\}$ containing the airfoil types used along the blade span, the twist $\theta(\eta)$ and chord $c(\eta)$ distributions along the blade span η, and many others, i. e. the mechanical properties of the materials or the direction of the fiber within the laminates.

Problem (5.1) looks at the minimum of the differences between model and target edge-wise bending stiffness, and subjected to some constraints; the quantities $\hat{(\cdot)}$ are referred to the model, and are function of the structural configuration p_s and given data D. The first constraint given by the Problem (5.1b), is used to express the bounds of the unknown structural parameters, for example the minimum and/or

maximum thickness of the spar cap, in order to account for the minimum carbon fibers layer thickness, or to limit the minimum spar width in order to succeed in cutting the carbon plies and to have enough gap between the optical sensors. Inequality (5.1c) constrains the lowest three natural frequencies $\hat{\omega}_i(p_s, D)$ to match, with a certain tolerance ε_ω, the corresponding scaled values of the target blade. Inequality (5.1d) constraints the difference in Lock number to be lower than a small tolerance ε_{Lo}, while Inequality (5.1e) constraints the norm of the sectional flap-wise bending stiffness difference to lay below the tolerance $\varepsilon_{\mathbf{K}_{\text{flap}}}$.

The aforementioned constrained optimization procedure requires the ability to define parametric beam models of the blade, as well as to numerically evaluate the blade natural frequencies. The beam models are based on the multibody formulation reviewed in [58]. The structural parameterization used by the optimization problem is based on detailed cross-sectional models of the blade at a certain number of span-wise locations; from these models, equivalent cross sectional stiffness and inertial data are generated using the approach of [87], which leads to the definition of the beam sectional data. The structural model of the blade comprises the following elements:

- a description of the external shape of the blade, which is obtained by providing the airfoil data coordinates at each span-wise location. This information, together with the curved and twisted aerodynamic reference line and its associated chord length data, fully defines the external blade geometry;
- a description of the blade cross section and span-wise internal geometry. The cross section definition requires, at a number of stations along the span, to define the chord-wise location, the chord extension and thickness of the spars, as well as the thickness of the external blade skin. The cross section is modeled using: 1) panels made of equivalent materials for modeling the spars, which involves a discretization of the mid-thickness line with 1D elements, and the external skin; 2) 2D quad elements for modeling the `Rohacell` core. The mesh density parameters are associated to the structural elements to support the computation of beam-like equivalent structural blade properties;
- for each cross section, a description of the lay-up of composite laminates of skin and spars, together with the definition of all the necessary material properties. In this regard, the carbon and skin-glue properties are constant for each cross section, while the `Rohacell` properties may vary from section to section due to the fact that the amount of core compression (see Section 5.4) changes along the blade span.

The optimization parameters $\mathbf{p}_s = \{p_{s,c}; p_{s,w}; p_{s,t}\}$ are the chord-wise location $p_{s,c}$, the width $p_{s,w}$ and thickness $p_{s,t}$ of the spars at a number of user-defined locations along the blade span. The distribution of the spars chord-wise location $s_c(\eta)$, width $s_w(\eta)$ and thickness $s_t(\eta)$ along the blade span, is then defined as:

$$s_c(\eta) = \chi_c(\eta) p_{s,c}, \tag{5.3a}$$

$$s_w(\eta) = \chi_w(\eta) p_{s,w}, \tag{5.3b}$$

$$s_t(\eta) = \chi_t(\eta) p_{s,t} \tag{5.3c}$$

where $\chi_c(\eta)$, $\chi_w(\eta)$ and $\chi_t(\eta)$ are linear shape functions.

The code `ANBA` [87] is used for defining the structural and inertial characteristics of the cross sections along the blade span, which are used as inputs for the definition of the beam model. The computation of a possibly fully populated sectional stiffness matrix, which hence accounts for all possible couplings (flap-torsion, flap-lag, extension-torsion, etc.), is performed starting from a detailed finite element mesh of the cross section using the anisotropic beam theory. The analysis also yields all other data of interest, including location of centroid and elastic center, orientation of principal axes, sectional inertia and mass. The analysis is conducted for each section along the blade span, whose number and location can be selected by the user, which provides for an accurate representation of the blade characteristics; the number of sections is usually significantly larger than the number of span stations where optimization parameters p_s are defined.

The Problem (5.1) is mixed continuous-discrete, since some of the the unknowns $\mathbf{p}_s$ can assume real values, i. e. the chord-wise location and the width of the spars, while the spar thickness is restricted to assume only discrete values, i.e multiple of the thickness t_{ply} of the ply. Instead of solving the problem using discrete optimization algorithms, usually slower and more complex to manage, the solution $\mathbf{p}_s^* = \left\{p_{s,c}^*; p_{s,w}^*; p_{s,t}^*\right\}$ of Problem (5.1) is considered intermediate, and used as guess for finding the final solution by solving the following problem:

$$\mathbf{p}_{s_f}^* = \arg\min_{\mathbf{p}_{s_f}} \left\| \frac{\hat{\mathbf{K}}_{edge}(\mathbf{p}_{s_f}, D_2) - \tilde{\mathbf{K}}_{edge}}{\tilde{\mathbf{K}}_{edge}} \right\|, \tag{5.4a}$$

$$\text{s.t.:} \quad \mathbf{g}_s(\mathbf{p}_{s_f}) \leq \mathbf{0}, \tag{5.4b}$$

$$\left| \frac{\hat{\omega}_i(\mathbf{p}_{s_f}, D_2) - \tilde{\omega}_i}{\tilde{\omega}_i} \right| \leq \varepsilon_\omega \quad i = 1 : N_\omega, \tag{5.4c}$$

$$\left| \frac{\hat{Lo}(\mathbf{p}_{s_f}, D_2) - \tilde{Lo}}{\tilde{Lo}} \right| \leq \varepsilon_{Lo}, \tag{5.4d}$$

$$\left\| \frac{\hat{\mathbf{K}}_{flap}(\mathbf{p}_{s_f}, D_2) - \tilde{\mathbf{K}}_{flap}}{\tilde{\mathbf{K}}_{flap}} \right\| \leq \varepsilon_{\mathbf{K}_{flap}}, \tag{5.4e}$$

with unknowns $\mathbf{p}_{s_f} = \left\{p_{s_f,c}, p_{s_f,w}\right\}$, i. e. the chord-wise location and the width of the spars, and $\mathbf{p}_{s_f}^{(0)} = \left\{p_{s,c}^*, p_{s,w}^*\right\}$. The span-wise distribution of the spars thickness is not anymore an optimization variables, but is included in the list of the given data D_2, where it appears as discrete value multiple of the ply thickness t_{ply}.

$$D_2 = \left\{R, \text{AF}, c(\eta), \theta(\eta), \left\lceil \frac{s_{t,s}^*(\eta)}{t_{ply}} \right\rceil * t_{ply}\right\} \tag{5.5}$$

The constrained Problem (5.1) and Problem (5.4) can both be solved with continuous optimization algorithms. In particular, when refining an already good design solution, i. e. the one of Problem (5.1), which hence provides an initial guess close

to the optimal one, more efficient gradient-based methods can be used to solve Problem (5.4). Both the problems are solved here by Sequential Quadratic Programming (SQP) method available in the `fmincon` routine of Matlab.

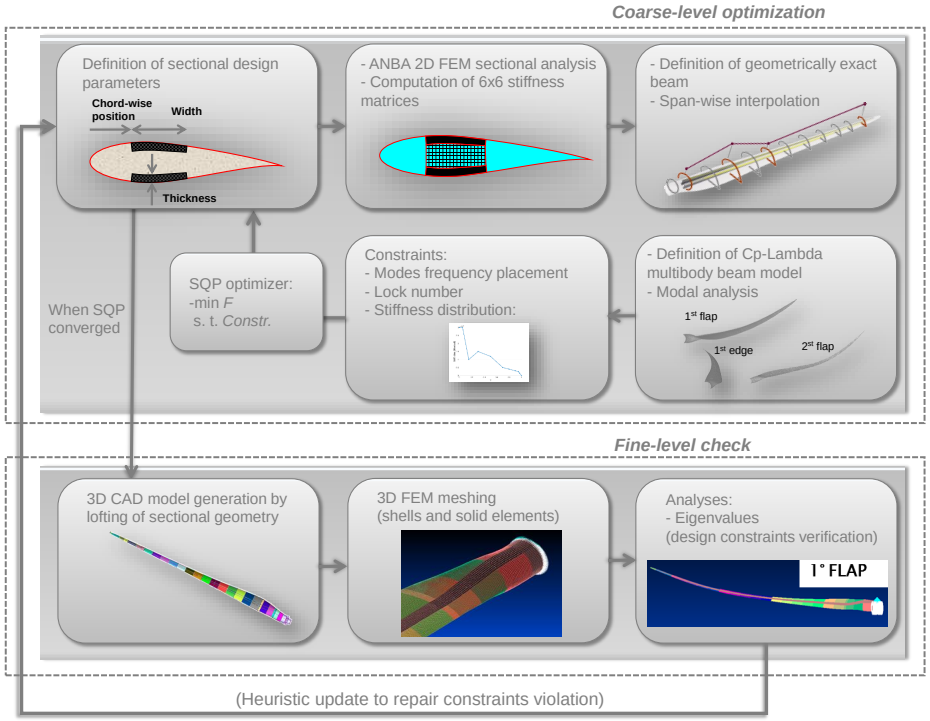

Figure 5.5: *Multi-level structural blade design tool*

Fine-level check of the requirements conformity

The next step to the coarse-level optimization is checking the fulfillment to the design constraints, i. e. natural frequencies and Lock number, by performing structural analysis on a detailed 3D FEM blade model. Indeed, the effect on blade structural properties, produced by regions with rapidly changing geometry in the span-wise direction can not be correctly represented by beam models, which is used in the multibody environment. The complete CAD solid model is generated as follows. A number of cross sections, typically of the order of one hundred, are obtained by thickness-interpolation of the generating airfoil data points, using their span-wise chord and twist distributions. From the chord-wise interpolation of the airfoils, collocations data points are obtained with sufficient sampling resolution (typically of the order of one thousand points per cross section) to allow for an accurate surface parameterization. The latter is obtained using NURBS [88], on each surface describing the two carbon fiber spars and on the skin (see Figure 5.6) covering the whole blade surface. The resulting 3D CAD geometry is then imported in HyperMesh.

The FEM model of the blade is based on mid-thickness shell elements used for the glue-made blade skin and the carbon fiber spars, while solid tetra elements are

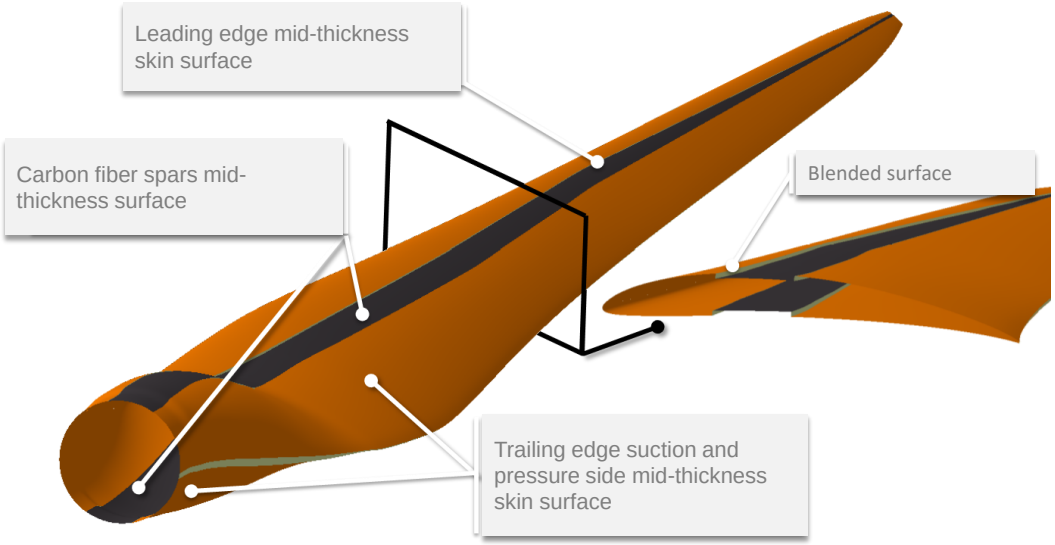

Figure 5.6: *NURBS surfaces for CAD model generation*

used for the `Rohacell` core and the metal part placed at the root of the blade during the lamination process. The material properties are associated to each element type, according to what is described in the Paragraph 5.3.1. Appropriate boundary conditions are then imposed by restraining all nodal translational degrees of freedom for the nodes located on the root surface.

The structural constraints are investigated through the detailed 3D FEM model. The Lock number is evaluated by looking at the flapping moment of inertia, while the blade modal frequencies are calculated by linear modal analysis in `MSC Nastran`.

Since the mass distribution is directly moved into the 3D FEM environment from the multibody model, no significant mismatches are found in terms of Lock number. If, instead, the verification of the constraint conditions on the fine level model reveals that design inequalities on frequency placement are not satisfied, a heuristic approach is applied, consisting of modifying the constraints proportionally to the violation amount. In particular, assuming that the beam-model first natural frequency $\hat{\omega}_1^{BM}$ is correctly placed at the end of the i^{th} coarse level optimization, i.e $\left|\hat{\omega}_1^{BM} - \omega_1\right| / \omega_1 \leq \varepsilon_\omega$, but it is not when the fine level 3D FEM analysis is performed, i.e. $\left|\hat{\omega}_1^{FEM} - \omega_1\right| / \omega_1 \geq \varepsilon_\omega$, then the target natural frequency for the next iteration is modified as

$$\omega_1^{(i+1)} = r_\omega \, \omega_1^{(i)}, \tag{5.6}$$

where $r_\omega = \hat{\omega}_1^{BM} / \hat{\omega}_1^{FEM}$. This way, a constraint condition reflecting the results obtained with the fine-level verification is imposed at the next coarse-level iteration. It may be expected that the ratio between the natural frequencies computed with the beam model and the 3D FEM analysis is almost constant for moderate variations of the structural element sizes. Therefore, the present approach can be used for refining the coarse level analysis according to the results from the fine level solution.

Aero-elastic blades design with BTC

Once the scaled blade is designed, a second step is to generate a sufficient bend-twist coupling, obtained by rotating the carbon fibers on the spars. For this purpose, the best approach is to introduce BTC to twist the blade sections in a way to decrease the angle of attack, the so called twist-to-feather concept shown in Figure 5.4, more suitable for load reduction applications, as discussed in [27, 85, 89].

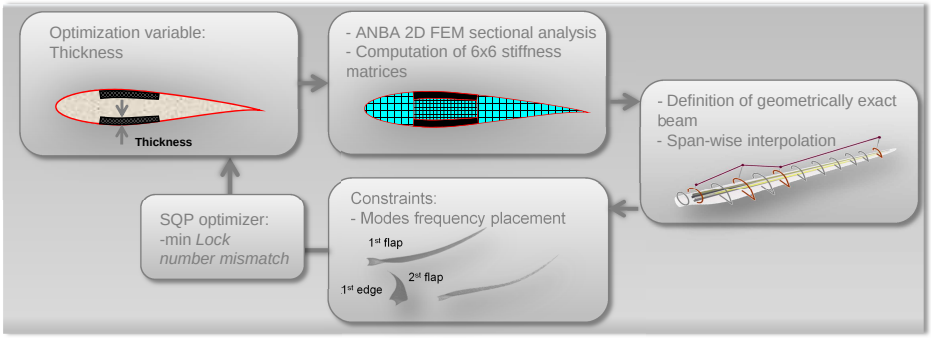

Figure 5.7: *Coarse-level optimization for the BTC blade*

To this end, the fibers are rotated in the spar of an angle equal to θ_{spar}. This way one gets the structural coupling coefficient defined as following [85]:

$$\alpha_s = \hat{K}_{ft} / \sqrt{\hat{K}_{flap}\hat{K}_{tors}} \tag{5.7}$$

where $\hat{K}_{flap}$ is the local flap-wise bending stiffness, $\hat{K}_{tors}$ the torsional one and $\hat{K}_{ft}$ the coupled bend-twist stiffness) is computed with `ANBA` for several cross-sections along the blade span for a fiber rotation θ_{spar}= 3 degs.

The design of the coupled blade is carried using the coarse level optimization described in the scheme in Figure 5.7 starting from the blade design without BTC. To better understand how the most suitable optimization problem is figured out, the following considerations should be kept in mind:

- From a design point of view, the rotation of the carbon fibers away from the blade axis leads mainly to a reduction of the out-of-plane bending stiffness; this would implies a redesign of the spar in order to match with the scaling constraints.
- As well explained in Section 5.4, the spars are manufactured with an ad-hoc mold, thought to be flexible for the realization of spars with generic θ_{spar}-oriented carbon fibers. This requires a constrained spar-shape, i. e. a constrained spar width and chord wise position along the span.
- Since the width and the chord-wise position of the spar should be kept frozen for the previous consideration, a redesign of the spars to compensate for the loss of the flap bending stiffness would imply an increase of the spars thickness, which in turn may bring to an increase (even if moderate) of the blade weight and a reduction of the modal frequencies, which would lead to increase

the bending stiffness to compensate for it, with a consequent mismatch in Lock number.

To account for all the aforementioned considerations, the width $s_w(\eta)$, and the chord-wise position $s_c(\eta)$ of the spars are not considered optimization variables anymore. They are taken from the design of the scaled blade without bend-twist coupling and added to the given data list, together with the carbon fibers orientation: $D_3 = \left\{R, \text{AF}, c(\eta), \theta(\eta), s_w(\eta), s_c(\eta), \theta_{\text{spar}}\right\}$. The design was carried out constraining the placement of the blade natural frequencies $\hat{\omega}_i$ and with the goal of minimizing the Lock number mismatch due to the unavoidable increase of the spars thickness. Hence, the coarse level design problem was formulated according to the following:

$$\mathbf{p}^*_{s_3,t} = \arg\min_{\mathbf{p}_{s_3,t}} \left| \frac{\hat{Lo}(\mathbf{p}_s, D_3) - \tilde{Lo}}{\tilde{Lo}} \right| \tag{5.8a}$$

$$\text{s.t.:} \quad \mathbf{g}_s(\mathbf{p}_{s_3,t}) \leq \mathbf{0}, \tag{5.8b}$$

$$\left| \frac{\hat{\omega}_i(\mathbf{p}_{s_3,t}, D_3) - \tilde{\omega}_i}{\tilde{\omega}_i} \right| \leq \varepsilon_\omega \quad i = 1:3 \tag{5.8c}$$

where the solution $\mathbf{p}^*_{s_3,t}$ is the optimal spar thickness distribution. The latter was then discretized according to the carbon ply thickness, and then the fine-level check is performed in order to verify the constraint condition. Few iterations of the overall algorithm were required until the final configuration is obtained. Figure 5.8 shows the spar distribution along the span in terms of width, chord-wise position and thickness, for the case with and without BTC.

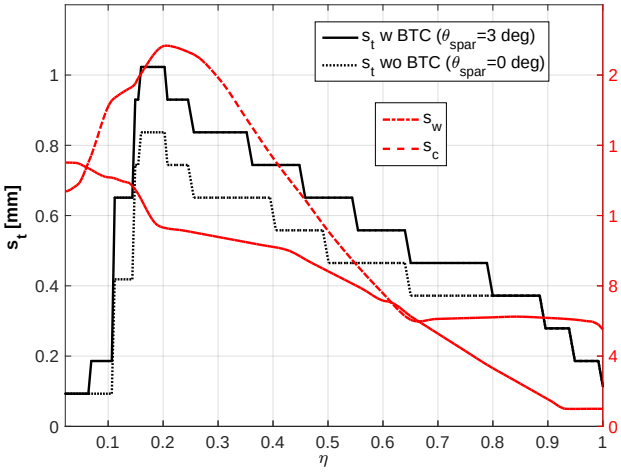

Figure 5.8: *Dimensions of the spars along the span for the scaled blade.*

In the case with BTC it is possible to observe that the thickness increases to compensate for the loss of stiffness due to the rotation of the fibers. The beam properties, including frequencies and Lock number remain very close to the case without BTC, therefore the choice of freezing the spar shape while taking the thickness as optimization variable is revealed successful. Table 5.3 shows the first three scaled-up

frequencies and the Lock number of the designed blade with BTC in comparison to the 5 MW RWT. The three natural frequencies are close to the reference value, with differences below 6%.

Table 5.3: *Computed frequencies of the scaled-up designed blade (3D FEM analysis). A comparison with the baseline.*

	Baseline	BTC Blade (scaled-up)	Diff.
1^{st} Flap-wise freq.	0.702 Hz	0.742 Hz	+5.7 %
1^{st} Edge-wise freq.	1.088 Hz	1.137 Hz	+4.5 %
2^{nd} Flap-wise freq.	1.960 Hz	1.981 Hz	+1.0 %
Lock number	21.76	20.25	-6.9 %

5.4 Blade manufacturing process

The entire manufacturing process was set up for realizing, with a high level of reproducibility, good quality blades capable to fullfill the design requirements. Since the shape of the blade is complex, and the technology is totally new, all possible critical aspects were unknown. Hence, the process is built step by step in order to acquire a certain confidence level of all aspects. It is debugged by the realization of several untapered and untwisted specimens samples with chord equal to 50 mm, equipped with two optical fibers and one FBG sensor per each. The speciments were designed with the design tool and then manufactured. Experimental modal analyses are also set-up and performed in order to see if the manufacturing process is capable to satisfy the design requirements. The results, compared with the design expectations, showed a good quality of the process, with mismatches in frequencies lower then 6%. The final manufacturing process consists of the following parts:

- **Blade core shaping**. The core part of the blade is made with `Rohacell WF 71`, which defines the overall shape of the blade that should match the designed geometry. For this reason, the 3D CAD model is used to seed a CNC machine tool that provided for the realization of the desired shape.

  The thickness distribution of the machined core is slightly greater than the blade one. With this stratagem, once the mold is closed, the core is forced to lay in a lesser volume which results in a slight increase of the `Rohacell` density and pressure that the core exerts on the inner mold surfaces. The mold is then put in the oven, and once the curing process reached the glass transition temperature, the inner pressure favors the homogenous distribution of the resin, which meanwhile become fluid, over the blade, and thus results in a good surface finishing. Furthermore, the core is conveniently machined in order to create, over its external surface, the grooves where the carbon spars are layed down during the assembly process. In the end, the filler root is worked up to allow the connection with a steel part, which was opportunely worked for housing the pitch motor.

- **Carbon fiber plies realization**. The plies with carbon fiber rotated of 3 degs are produced from the material roll and starting from the mathematics of the

plies flat pattern, an automatic cutting tool was used, which allows to obtain reproducible plies with a good finishing.

- **Spars lamination**. This process is carried out before the final assembly, with the goal of having the plies correctly stacked in accordance to the ply-book. During the lamination process the optical fibers are embedded between the two outer plies while the FBG sensors are placed at a certain location, by means of a printout of the spar layout. The spar's curing process is carried out through the aid of an ad-hoc mold, specifically designed to avoid damage of the optical fibers, as shown in Figure 5.9.

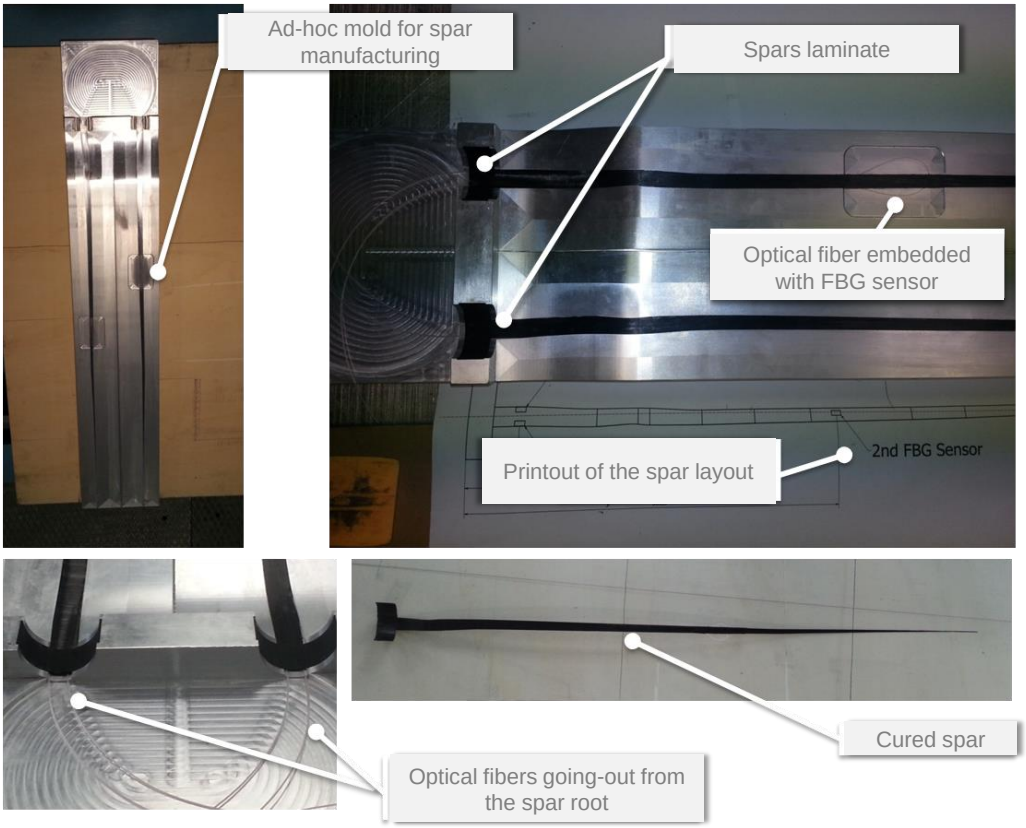

Figure 5.9: *The mold used for the spar curing process.*

- **Blade assembly**. Once all the blade sub-components are available, it is possible to proceed with the final assembly and, immediately after, with the final curing process. An aluminum alloy female mold, made up of two Computer Numerical Control (CNC) machined and polished halves, is designed by taking into account for the thermal expansion of the carbon fibers and the alloy itself. The two halves of the mold perfectly match at the leading edge parting plane, while there is a small gap of 0.1 mm at the trailing edge parting plane, so as to allow excess resin to squeeze out. Finally, some support blocks allow the fixing of the blade root to the mold.

Once spread a thin layer of release agent on the mold, the assembly is characterized by the phases shown in Figure 5.10 and listed below:

1. a thin film of glue is used for sticking together the `Rohacell` core and the metal part on which the bearings and the pitch motor are assembled;
2. both spars' laminates are laid down on the `Rohacell` core surfaces and a thin layer of glue is used to ensure the bonding between the two parts;
3. one single layer of glue is laid up over the core using the mold as supporting base, so as to avoid breaking the fragile core; the resin film is laid on one side of the blade, wrapped around the leading edge and then laid on the other side, so as to form a continuous and homogeneous coating;
4. finally, such an artifact is placed over one half of the mold, with the second half successively fixed to the first one using several uniformly spaced screws: in this way high and uniform pressure is generated thanks to the `Rohacell` compression. The metal root part is fixed, by means of small screws, at the mold support blocks, where small holes allow the optical fibers going out from the mold without causing damage.

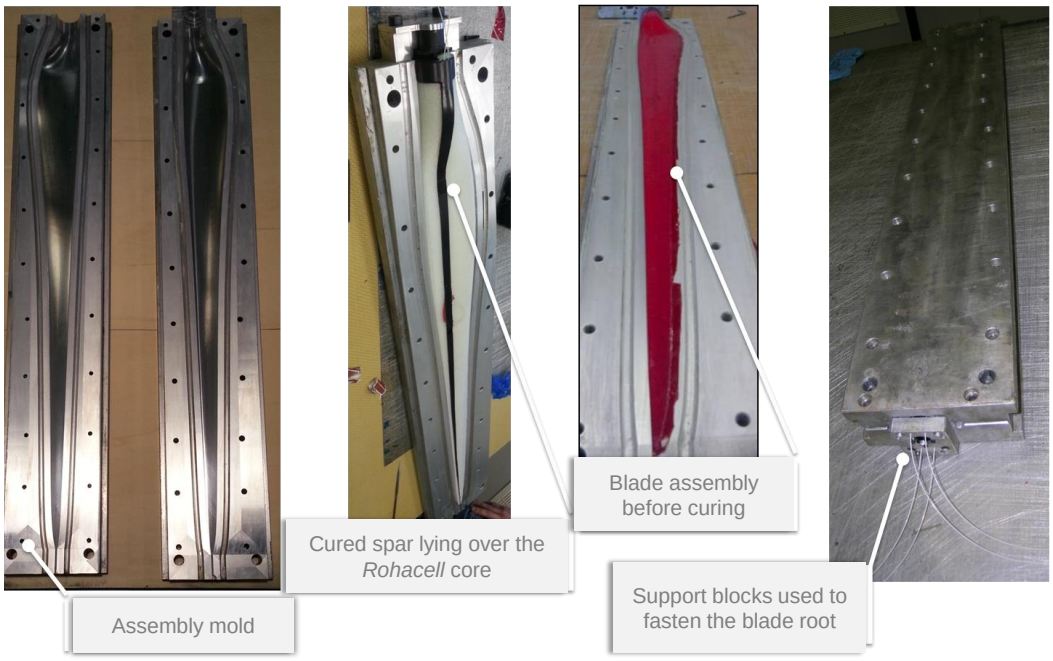

Figure 5.10: *Blade sub-components assembly.*

Once the assembly procedure is finished, the polymerization process takes place in the oven with monitored temperature. At the end of the production process, modest finishes are necessary to obtain a high-quality aero-elastic blade.

5.5 Blade structural characterization

The structural characterization consisted of the following items:

- verify the compliance to the design requirements discussed in Section 5.3.1, i.e. the modal frequencies and the Lock number;
- verify the amount of BTC;
- identify the distributed structural properties of each blade;
- calibrate the FBG sensors.

5.5.1 Dynamic *Frequency Response Functions* test

Experimental modal analysis is carried out to characterize the structural dynamics of the blades. With a certain level of confidence on the reproducibility of the manufacturing process, the test is conducted on only one blade. The root is constrained rigidly to a steel-made plate fixed to the floor, thus ensuring a perfectly rigid constraint. The modal analysis is performed with the procedure debugged by some sample speciments, and consisted in some impact hammer tests to excite the structure; then, through miniaturized and lightweight (0.5 g) `PCB 352C22` accelerometers and exciting the structure at almost 20 different locations using an hammmer instrumented with a load cell `PCB 086B03` (see Figure 5.11), it was possible to reconstruct, with a good accuracy, the eigen-shape associated to out-of-plane and torsional modes.

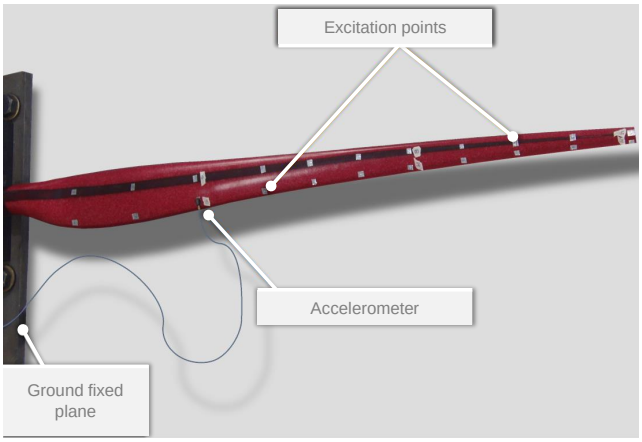

Figure 5.11: *Modal testing with hammer.*

On the basis of the measured Frequency Response Functions (FRFs), six out-of-plane and torsional natural frequencies $\check{\omega}$, related damping $\check{\zeta}$ and eigenvectors $\check{\mathbf{\Phi}}$, are identified, together with two in-plane natural frequencies with related dampings.

Table 5.4 reports the comparison between the experimental and numerical natural frequencies, as well as the value of the MAC($\hat{\mathbf{\Phi}}_i^{(3D-FEM)}, \check{\mathbf{\Phi}}_i$) operator, where $\hat{\mathbf{\Phi}}_i^{(3D-FEM)}$ is the i^{th} eigenvector computed with the 3D FEM model. The comparison is quite satisfactory and especially the measured eigen-shape of the flap-wise modes

Table 5.4: *Measured natural frequencies, and related damping, identified on the basis of the measured FRFs and compared with the one computed on the 3D FEM model.*

Mode	$\check{\omega}$ [Hz]	$\check{\zeta}$ [%]	$\hat{\omega}^{(3D\text{-}FEM)}_{[3]_{st}}$ [Hz]	$\Delta\omega$ [%]	MAC
1^{st} Flap-wise	20.7	0.86	20.6	0.5	0.99
1^{st} Edge-wise	33.73	-	35.7	-5.6	-
2^{nd} Flap-wise	55.1	0.74	54.1	1.8	0.978
2^{nd} Edge-wise	109.7	-	108.6	1.0	-
3^{rd} Flap-wise	115.9	0.85	113.5	2.1	0.917
1^{st} Torsional	155.5	1.52	165.4	-5.9	0.563
4^{th} Flap-wise	194.2	1.25	189.8	2.3	0.969
2^{nd} Torsional	240.6	1.51	253.6	-5.3	0.539

well matches the corresponding numerical ones. Also the numerical values of the natural pulsations of the torsional and edge-wise modes well match the measured ones, with maximum errors of less than 6%.

Table 5.5: *Measured blade mass and center of gravity span-wise position, variation with respect to the design*

	$\check{m}$ [g]	$\check{r}_g$ [mm]	Δm [%]	Δr_g [%]	ΔLo [%]
1^{st} Blade	76.7	190.6	+1.05	+3.38	-7.40
2^{nd} Blade	76.5	190.5	+0.78	+3.32	-7.06
3^{rd} Blade	76.0	191.2	+0.13	+3.70	-7.14

To evaluate the Lock number mismatch, the three blades were checked in terms of mass $\check{W}$ and center of gravity span-wise position $\check{r}_g$. Table 5.5, reports the measurements, where the mass of the blade root steel part is also accounted. The results effectively highlight a discrete reproducibility of the manufacturing process and the good match with the design, highlighting errors in the Lock number of approx 7%.

5.5.2 Static tests

The static tests are performed on three blades with the following main goals:

- identify the blade distributed structural properties;
- verify the amount of BTC;
- calibrate the FBG sensors.

The bend-twist coupling is readily verified by loading the blades opportunely and evaluating the kinematics in terms of flapping and torsion. To this end, the blade is fixed from its root at a rigid steel-made structure and is equipped with four saddles placed at span $\eta = [0.2, 0.5, 0.8, 0.93]$. The blades are positioned with the suction side facing down and the saddles in the horizontal position. Dead loads are applied at each saddle by some hooks located at three different points: the central point aligned with the pitch axis, while the other two aligned respectively with the trailing edge and the leading edge. Three laser LAS8010 displacement transducers

are used at each saddle to measure the vertical and horizontal deflections, as well as to evaluate the torsion. Each blade is subjected to various loads inducing either mostly pure flap or flap-torsional deformations. For the pure flap-wise tests saddles are loaded at the central hooks. Similarly, for the flap-torsional tests, saddles are loaded at both lateral hooks which resulted respectively in a leading edge pull-down and in a trailing edge pull-down. By comparing the latter cases it is possible to distinguish the BTC effect, since it seems that a leading edge load is not able to twist the blade, differently from the trailing edge pull-down.

To complete the structural characterization, together with the FBG sensors calibration, several tests are performed in both flap and edge directions. For the edge tests each blade is rotated in a vertical position, with the trailing edge facing down. Dead loads are applied at each saddle by hooks located at a point aligned with the trailing edge. Totally, twelve load cases were performed:

- 3 flap (flap test configuration)
- 3 trailing edge pull-down (flap test configuration)
- 3 leading edge pull-down (flap test configuration)
- 3 edge (edge test configuration)

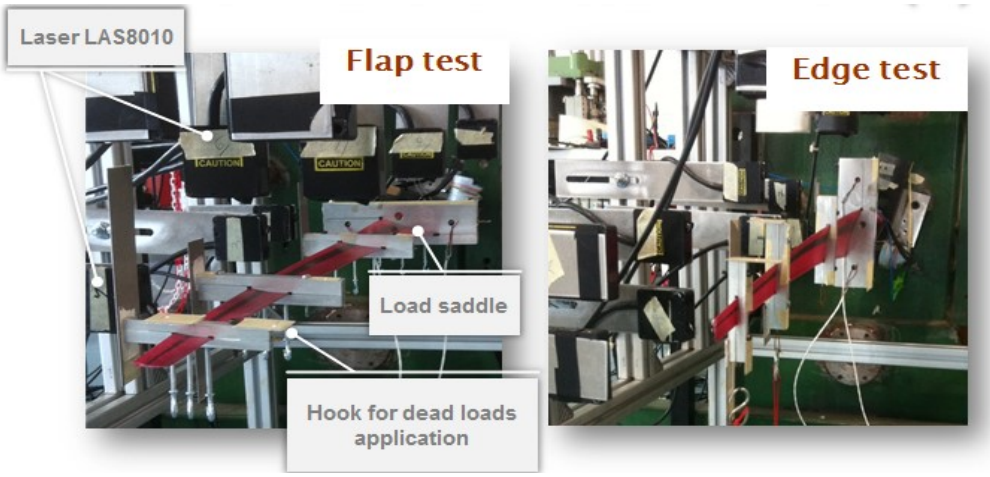

Figure 5.12: *Static testing set-up.*

Figure 5.12 shows the static tests configurations, with the twelve laser installed to acquire the four saddles' displacements. The left picture shows the set-up for the flap tests, i. e. with the blade suction side facing down. In this configuration, for each saddle, two lasers are mounted at the top of the fixture, in order to acquire the vertical displacement of two distant points: in this way it is possible to estimate the torsion of the blade at the saddle station by difference of the two measures. A further laser is mounted laterally to acquire the edge displacement. The right picture shows the set-up for the edge tests, i. e. with the blade trailing edge facing down. With the same scope of estimating the torsion, for each saddle two lasers are mounted laterally, while for capturing the edge displacement, one laser is used at the top.

Figure 5.13 shows two flap test cases. At left a leading edge pull-down while at right a trailing edge pull-down.

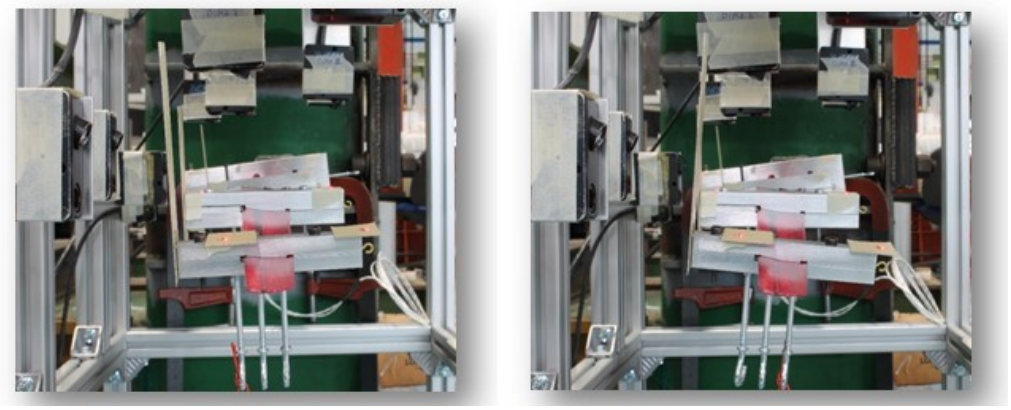

Figure 5.13: *Leading edge pull-down to the left side, Trailing edge pull-down to the right side*

The experiments are modeled in the `Cp-Lambda` multibody environment, by using the blade design model, while rigid bodies are used to model the saddles. All the tests are simulated and the laser measurements opportunely reconstructed. Hereinafter in Figure 5.14 and Figure 5.15 some results related to the first blade are reported. The figures comprise either the measurements and the results of the simulated tests. These results are also used for calibrating the FBGs.

5.5.3 Identification of the blade distributed structural properties

Improving the fidelity of the blade beam structural model is a key aspect in order to obtain a comprehensive validated model of any wind turbine. In fact, although modern wind turbine models are able to capture the coupled aero-servo-structural behavior of the machine, having a correct tuning of structural (and aerodynamic) properties is still a challenge. This issue becomes even more pronounced when considering a complicated structural behavior like the one involved in BTC blades. From the structural point of view, the BTC blade can be modeled according to geometrically exact beam formulations [90], with fully populated sectional stiffness matrices. With the goal of updating such structural beam properties so as to reduce the mismatch between measured and simulated deflections, an updating procedure has been deployed and here briefly described. The parameter estimation problem is formulated as a maximum-likelihood constrained optimization [92, 93], solved using a Sequential Quadratic Programming (SQP) approach [94]. A Singular Value Decomposition (SVD) is used to strengthen the formulation and allow for the effective tuning of the model even when, as it is often the case, its parameters may be affected by a relatively low observability.

Consider a parameterized version of a beam structural model $\mathcal{M}(\mathbf{p})$ where $\mathbf{p}$ represents the vector of to-be-estimated parameters related to the distributed structural properties. The output of this model, either displacements and/or vibrational frequencies, is defined as $\mathbf{y} = \mathbf{h}(\mathbf{p})$, with $\mathbf{y} \in \mathbb{R}^m$. Their associated measured quantities

$\mathbf{z}$ can be expressed as

$$\mathbf{z} = \mathbf{y} + \mathbf{r}, \tag{5.9}$$

where the error $\mathbf{r}$ is due to both measurement and modeling, the latter caused by modeling approximations or unresolved physics in $\mathcal{M}$.

Having a sample of observations $S = \{\mathbf{z}_1, \mathbf{z}_2, \ldots, \mathbf{z}_i, \ldots, \mathbf{z}_N\}$, where N is the total number of the measures, the problem of finding the vector of parameters $\mathbf{p}$ leads to the minimization of the quadratic cost function J defined as

$$J = \frac{N}{2} \ln \det \mathbf{R} + \frac{1}{2} \sum_{i=1}^{N} \mathbf{r}_i^T \mathbf{R}^{-1} \mathbf{r}_i, \tag{5.10}$$

where the error covariance matrix is noted $\mathbf{R} = E[\mathbf{r}_i \mathbf{r}_j^T] = \mathbf{R}\,\delta_{ij}$, $E[\cdot]$ being the expected value operator and δ_{ij} the Kronecker delta symbol. Since $\mathbf{R}$ depends on the estimation errors $\mathbf{r}_i$ the problem can not be solved as simple weighted least square. Instead, the robust minimization is based on the following iteration:

1. Assuming a temporarily frozen error covariance $\mathbf{R}$, minimize with respect to $\mathbf{p}$ the cost

$$\hat{J} = \frac{1}{2} \sum_{i=1}^{N} \mathbf{r}_i^T \mathbf{R}^{-1} \mathbf{r}_i, \tag{5.11}$$

   which is obtained from Equation (5.10) by neglecting all irrelevant constants.

2. Assuming temporarily frozen parameters $\mathbf{p}$, minimize J with respect to $\mathbf{R}$, which gives [93]:

$$\mathbf{R} = \frac{1}{N} \sum_{i=1}^{N} \mathbf{r}_i \mathbf{r}_i^T. \tag{5.12}$$

3. Return to step 1, and repeat until convergence.

The optimization problem is completed by multiple equality and inequality constraints and solved using a SQP approach [95]. Among many possible constraints, bounds on parameters and equality constraints are used here to enforce that the total mass and the blade center of gravity position do not change throughout the optimization process. The well-posedness for the estimation problem is one of the major concerns. In fact, for different reasons, one or more parameters or a linear combination of them may not be identifiable. Three examples can be mentioned to clarify the importance of such issue. First, a parameter may happen to have no effects on outputs. In this case, easily such parameters should be removed by the set of to-be-estimated unknown. Second, - and this is a rather interesting situation - it is possible that two parameters affect in a very similar way the outputs. In such a case, either the parameters cannot be identified together for the fact that one unknown can be compensated by a suitable change of the second. Finally, it is also possible that a parameter affects only an output associated to a higly noisy measurement. Again, although the parameter seems identifiable, the level of noise does not allow its precise estimation. This discussion highlights two aspects. First the

sensitivity-to-noise ratio, $\mathbf{R}^{-1/2}\mathbf{G}$, being $\mathbf{G} = \partial\mathbf{y}/\partial\mathbf{p}$, determines the observability of all parameters and, second, the fact that, especially in highly complicated estimation procedure, an a priori reformulation is needed in order to strengthen the optimation and ensure the well-posedness of the problem.

Such non-trivial reformulation can be obtained for constrained and unconstrained problems through the singular value decomposition (SVD) of the matrix $\mathbf{M}$ defined as:

$$\mathbf{M} = \begin{bmatrix} \mathbf{R}^{-1/2}\mathbf{G}_1 \\ \mathbf{R}^{-1/2}\mathbf{G}_2 \\ \vdots \\ \mathbf{R}^{-1/2}\mathbf{G}_N \end{bmatrix}, \tag{5.13}$$

with $\mathbf{G}_i$ the sensitivity matrices of the $i-$th observation. Infact, the SVD of matrix $\mathbf{M}$ writes

$$\mathbf{M} = \mathbf{U}\mathbf{\Sigma}\mathbf{V}^T, \tag{5.14}$$

where $\mathbf{U}$ and $\mathbf{V}$ are square orthogonal matrices, whose columns are respectively the left and right singular vectors of $\mathbf{M}$. Matrix $\mathbf{\Sigma}$ is then structured as

$$\mathbf{\Sigma} = \begin{bmatrix} \mathbf{S} \\ \mathbf{0} \end{bmatrix}, \tag{5.15}$$

where $\mathbf{S}$ is a diagonal matrix whose entries s_i are the singular values, customarily sorted in descending order, i.e. $s_1 \geq s_2 \geq \ldots \geq s_n \geq 0$. Now, given Equation (5.14) it is possible to verify that projecting the parameters $\Delta\mathbf{p}$ (with Δ refering to the variation respecting the initial nominal condition) in the subspace $\mathbf{V}^T$ one gets new orthogonal parameters, so that the

$$\mathrm{Var}(\bar{\theta}_j - \theta_j^*) \geq \frac{1}{s_j^2}. \tag{5.16}$$

with θ_j the new projected parameters, the symbols $(\bar{\cdot})_j$ and $(\cdot)_j^*$ are the true (unknown) ones and the estimates. The Equation (5.16) is the so-called Cramér-Rao condition [96] that limits the parameter uncertainties from below. The s_j^2 are the eigenvalues of the Fisher's matrix $\mathbf{F} = \mathbf{M}^T\mathbf{M}$. With this decoupling, the identification problem is significantly simplified, as one can now select an acceptable threshold for the variance of the estimates and identify only those parameters that can be estimated with a satisfactory level of accuracy.

In this way, the parameters $\mathbf{\Delta\tilde{p}}$, with the marker $(\tilde{\cdot})$ defining an intermediate transformation explained hereinafter, can be obtained at the end of the identification by projecting back the orthogonal parameters, so that the transformation writes $\mathbf{\Delta\tilde{p}} = \mathbf{V\Theta}$.

The afore described SVD robust re-formulation is applicable for the problems without equality constraints. For this reason, a suitable procedure is deployed as intermediate step for transforming the original problem in a form without equality

constraints, so that the parameter $\mathbf{\Delta\tilde{p}} = \mathbf{V}_{\mathrm{eq_N}}^T \mathbf{\Delta p}$, where $\mathbf{V}_{\mathrm{eq_N}}$ is the null-space of the equality constraints matrix.

Dealing with the beam property estimation considered here, the goal is to update the entire structural stiffness matrix and the mass distribution of the beam model. In order to keep the number of parameters to a minimum and to ensure the well-posedness of the problem, a two pronged approach is used. First, the unknowns to-be-estimated are represented by the nodes of a low-order span dependent linear piece-wise function which multiplies the baseline distribution of each property, according to the following:

$$\Pi_i(\eta) = \Pi_{0i}(\eta) p_i(\eta) \tag{5.17}$$

where η is the non-dimensional span-wise coordinate, Π_i is the $i-$th beam property, Π_{0i} is the related baseline property and finally $p_i(\eta)$ is the piece-wise linear corrective function, defined as

$$p_i(s) = \sum_j n_{ij}(s) p_{ij} \tag{5.18}$$

being p_{ij} the j-th node of the i-th corrective function and n_{ij} the related shape function. Second, the reformulation of the problem according to the SVD [97] is employed to ensure the well-posedness of the estimation procedure.

5.5.4 Results

In the following, results related to identification of the structural properties of the three blades are reported. Hereinafter the blades are labeled as Blade 1, Blade 2 and Blade 3, whose numbers identify the manufacturing sequence. The results reported from Figure 5.14 and Figure 5.15 refer to the Blade 2. Figure 5.14 shows the vertical ΔY and the torsion $\Delta\theta$ of one blade for the leading edge pull-down test, while Figure 5.15 shows the same parameters for the trailing edge case. On each figure, three plots are displayed. The blue triangle markers refer to the measurements acquired by the lasers, the green dot-dashed lines refer to the multibody simulations with the nominal beam-like model used for the blade design, while the red solid lines refer to the beam-like identified model. The torsion $\Delta\theta$ is evaluated at each saddle as the arctangent of the ratio between the the two in-plane laser measurements difference and their interaxis. The comparison with the numerical displacements of the initial beam-like multibody model highlights some differences. With respect to the nominal model, the manufactured blade shows a higher tendency-to-twist, especially for the inner sections (around $\eta = 0.5$). In the two tests the BTC twist-to-feather is observed, since the torsion along most of the span is always in a pitch-up sense, even when a leading edge pull is applied.

It is also clear that the identified model is improved with respect to the initial one and appears to be well correlated with the measurments especially in the half outer part of the blade. From the results obtained, it is possible to appreciate the goodness of the identified model outputs and, on the other side, to assess the ability of the beam model employed to characterize the behavior of the BTC blade.

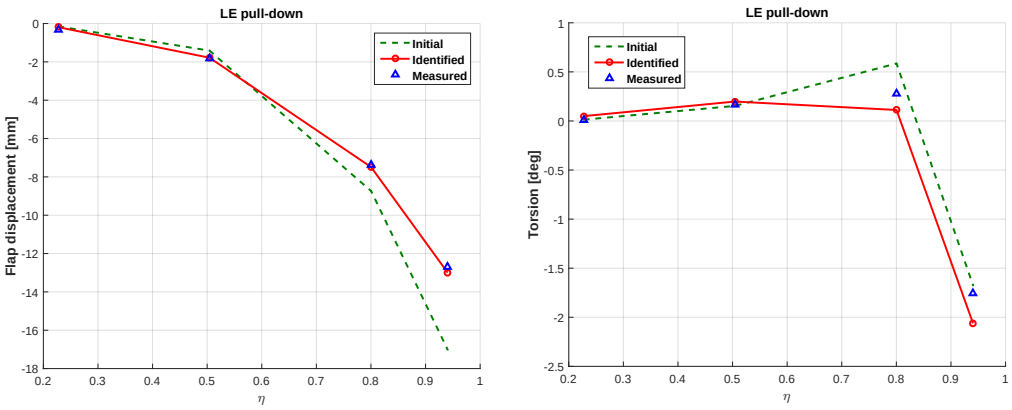

Figure 5.14: *Flap (left) and torsion (right) displacement related to the a leading edge pull down test case.*

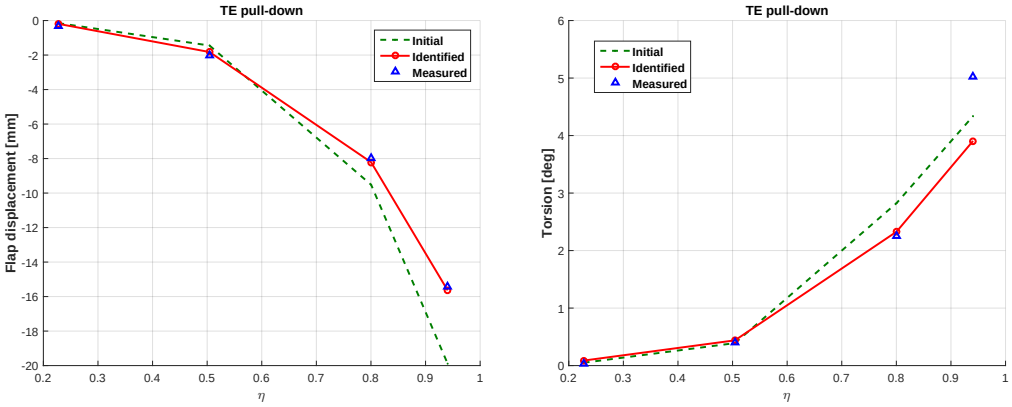

Figure 5.15: *Flap (left) and torsion (right) displacement related to the a trailing edge pull down test case.*

Figure 5.16 shows the frequency variation of the first eight eigenvalues respecting to the measurements of the (FRFs) analysis conducted on the Blade 1 (see Section 5.5). The figure highlights that no significant changes occur. A possible improvement on the frequencies can be achieved by a proper change of the weight coefficients of the cost function in the identification problem, for example increasing the ones related to the lower frequency modes, i.e. those with higher energy content.

The identification procedure is used to estimate the distributed structural properties on the three blades. For the blade on which the FRFs analysis is available, the optimization output are the twelve measurments with lasers of the static tests and the eight modal frequencies, while for the other blades the optimization outputs are only the static measurements. For the latter cases the mass distribution is not estimated. Figures from 5.17 to 5.20 show at left the most significant distributed properties of the three blades compared with the nominal values, while at right the relative percentage variation. The flapping stiffness reported in Figure 5.17 appears to be discretely matching the nominal values, with the Blade 2 and Blade 3 reaching the maximum mismatch of approx -10% in the inner portion.

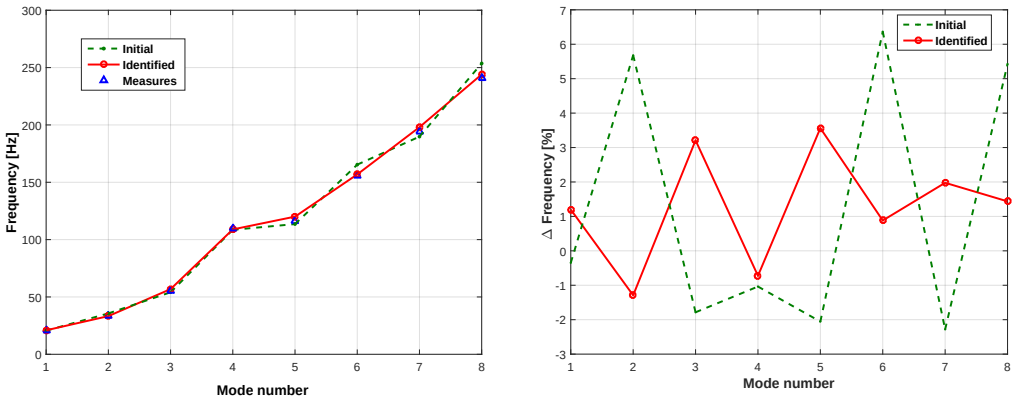

Figure 5.16: *Frequency and frequency variation wrt measurements of the vibration modes.*

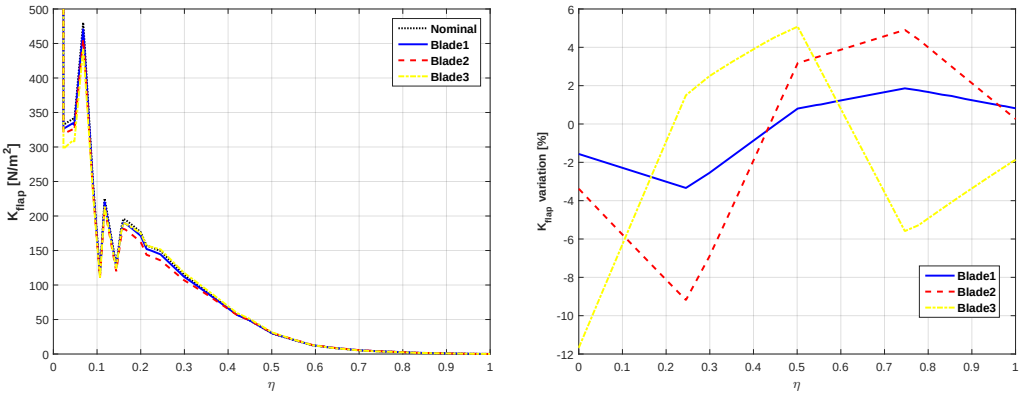

Figure 5.17: *Identified blade beam properties. Blade flap stiffness (left) and percentage variation with respect to the nominal values (right).*

The edge stiffness reported in Figure 5.18 appears to be lower respecting to the nominal value, with the Blade 3 reaching the maximum mismatch of approximately -25% in the inner portion.

The torsional stiffness are reported in Figure 5.19, showing a maximum mismatch of around -7% in the Blade 1.

Since the three blades are manufactured with the same lots of materials, but at different periods of time, with a distance of more than two years between Blade 1 and Blade 3, the mismatches may be imputable to the aging of the pre-preg. A deeper investigation would be necessary, and eventually a revisiting of the manufacturing process to improve its repeatability.

Figure 5.20 shows the structural BTC coefficient as defined in the Equation (5.7) over the span. It appears a discrete matching with the nominal value, the maximum mismatch reached in the Blade 3 for up to -12% in the inner span.

Finally, Figure 5.21 shows the mass distribution over the span for the only Blade1, since it needs the measurements of the modal frequencies obtained with the FRFs analysis, performed on the sole Blade1. The matching with the nominal values is very good, with minor differences of up to 4% at the tip, which by the way

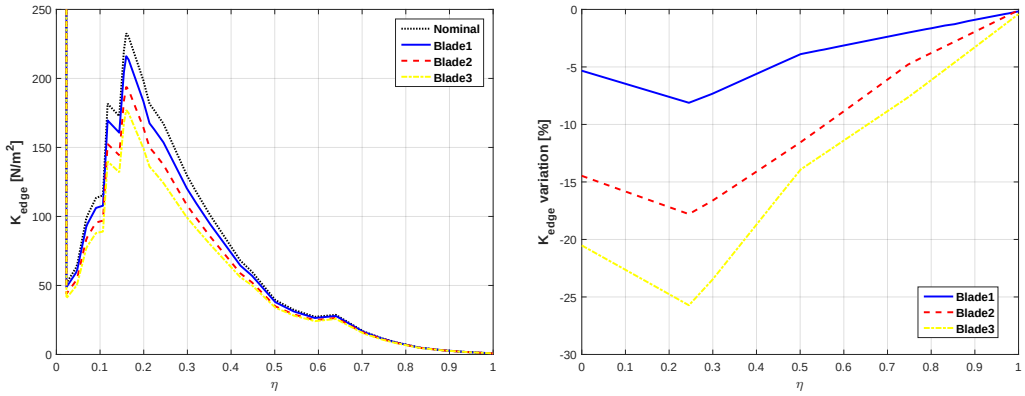

Figure 5.18: *Identified blade beam properties. Blade edge stiffness (left) and percentage variation with respect to the nominal values (right).*

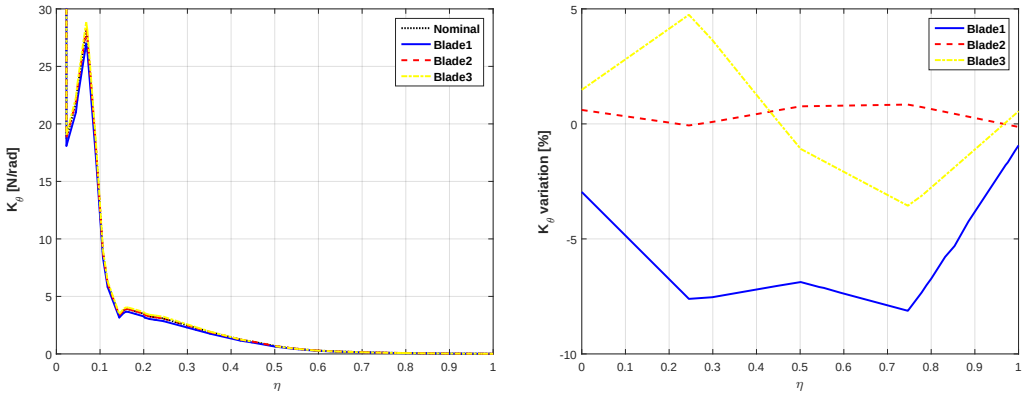

Figure 5.19: *Identified blade beam properties. Blade torsional stiffness (left) and percentage variation with respect to the nominal values (right).*

is the blade region not easily identifiable.

5.6 FBG sensors calibration

The FBG sensors are calibrated using the static tests and reading the bending moment at one third of the blade span. In order to acquire all the FBG sensors through only one optical channel, the four optical fibers embedded in the blade are connected to a miniaturized 4x1 optical coupler. The four FBG sensors work at different wavelengths, respectively at 1582, 1564, 1529 and 1547 nm. For this reason the four signals remain separated in the light beam thanks to the Wavelength Division Multiplexing (WDM). Sensors are acquired by a MICRON OPTICS SM130 interrogator system at a sample rate of 1kHz.

The position of the sensors is known with an uncertainty $\epsilon_{\text{FBG}} = \pm 10$ mm. Since the sensors are placed at approx. $\eta = 0.3$ and the four saddles at $\eta = [0.2, 0.5, 0.8, 0.93]$, only the load applied on the outer three saddles is used for the calibration.

For the twelve loads conditions, the associated flap wise and edge wise bending moment components at the sensor position are evaluated with an uncertainty of

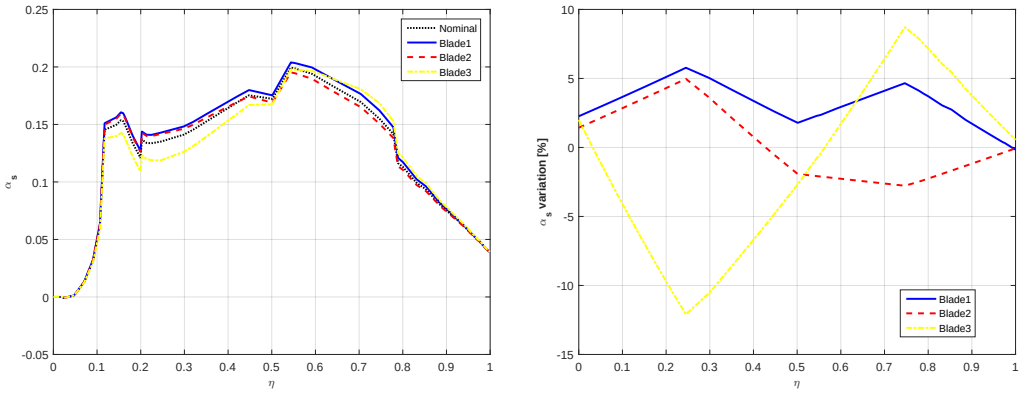

Figure 5.20: *Identified blade beam properties. BTC coupling coefficient (left) and percentage variation with respect to the nominal values (right).*

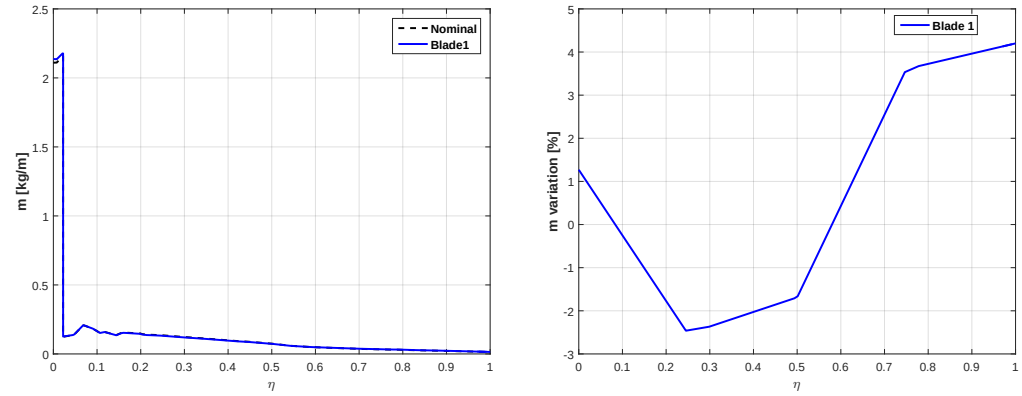

Figure 5.21: *Identified blade beam properties. Blade mass distribution (left) and percentage variation with respect to the nominal values (right).*

ϵ_{FBG}. Then the calibration problem of finding the two sets (one per each bending moment component) of four weight coefficients associated to the four FBG sensors is formulated as two least squares problems. For the flapping moment, the FBG position uncertainty ϵ_{FBG} is also included as unknown:

$$[\mathbf{c}^*_{\text{flap}}, \epsilon_{\text{FBG}}] = \arg\min_{\mathbf{c},\epsilon} \sum_{i=1}^{n_{\text{meas}}} \left(M_{\text{flap},i}(\epsilon) - \Delta\lambda_i^T \mathbf{c} \right)^2 , \tag{5.19a}$$

$$\mathbf{c}^*_{\text{edge}} = \arg\min_{\mathbf{c}} \sum_{i=1}^{n_{\text{meas}}} \left(M_{\text{edge},i}(\epsilon_{\text{FBG}}) - \Delta\lambda_i^T \mathbf{c} \right)^2 \tag{5.19b}$$

where $\mathbf{c}$ is the vector of the four sensors weights, $\Delta\lambda_i$ is the vector of the four sensors outputs (given in wave length) of the i-th load case, while $M_{\text{-},i}$ is the bending moment component of the i-th load case. Note that the uncertainty ϵ_{FBG} is solved in the first optimization problem (5.19b).

During the static test, one FBG signal was lost, therefore the weight coefficient associated to that measure is imposed null. The sensors position is found as η =

Table 5.6: *Estimated dead loads with FBG sensors in the static tests.*

Load Case	$\check{M}_{\text{flap}}$ [Nm]	$\tilde{M}_{\text{flap}}$ [Nm]	ΔM_{flap} [%]	$\check{M}_{\text{edge}}$ [Nm]	$\tilde{M}_{\text{edge}}$ [Nm]	ΔM_{edge} [%]
1^{st} Flap	2.1714	2.1760	0.09	0	-0.0130	-
2^{nd} Flap	2.0225	2.0292	0.33	0	-0.0125	-
3^{rd} Flap	0.7799	0.7748	-0.65	0	-0.0202	-
1^{st} TE pull-down	1.4623	1.4726	0.71	0	-0.0063	-
2^{nd} TE pull-down	1.6946	1.6895	-0.30	0	-0.0205	-
3^{rd} TE pull-down	0.6570	0.6500	-1.06	0	0.0173	-
1^{st} LE pull-down	1.4623	1.4469	-1.05	0	0.0467	-
2^{nd} LE pull-down	1.6946	1.6964	0.11	0	0.0193	-
3^{rd} LE pull-down	0.6570	0.6616	0.70	0	0.0021	-
1^{st} Edge	0	0.0019	-	4.6984	4.6991	0.02
2^{nd} Edge	0	-0.0039	-	5.7655	5.7587	-0.12
3^{rd} Edge	0	0.085	-	1.6399	1.6594	1.19

0.337. Table 5.6 reports a comparison between the applied loads and the estimates. The errors always remains below 1.1% in the flap direction and 1.2% in the edge direction. Therefore the results obtained are considered satisfactory.

5.7 Synopsis

The design and manufacturing processes of the scaled aeroelastic blade with BTC for wind tunnel testing are developed ad-hoc for this application and detailed in this chapter. One blade of the set is embedded with FBGs sensors. The structural characterization of the blades is succesfully performed. Following the results, some considerations may be drawn:

- The structural design, which is made with a multi-level structural blade design tool, showed good accuracy in matching the 5 MW WT scaling requirements, since the errors of the scaled-up modal frequencies and the Lock Number remain below 7%.
- The modal analysis shows errors in the modal frequencies and the Lock number below 10%.
- The identified blade distributed properties, obtained using a robust algorithm, are reported in terms of stiffnesses distribution, showing some discrepancies with respect to the nominal design. The mismatch reaches 25% for the edge stiffness. The results address to a general review of the manufacturing process.
- The mass distribution is identified for only one blade, and it resulted very close to the nominal design.
- The FBG sensors are calibrated from the static tests. The reconstructed loads by means of the FBGs are very accurate, with error around 1% in the flapping direction and 1.2% in the edge direction. During the static tests one sensor was lost and the calibration is done with only three sensors.

CHAPTER 6

Aerodynamic and load characterization of scaled multi-MW wind turbine with bend twist coupling

6.1 Introduction and motivation

This chapter describes the wind tunnel activity for the characterization of the scaled wind turbine model equipped with BTC aeroelastic blades, whose the realization is detailed in Chapter 5. The set of three aeroelastic blades is assembled on the hub of a scale tower-nacelle system provided with hard real-time module for supervising and monitoring the model in several working conditions. Two type of investigations are conducted in order to characterize the aerodynamic performance of the rotor with BTC and to evaluate its load mitigation. For the former goal, the tests are conducted in the aeronautical section of the wind tunnel of *Politecnico di Milano*, featured with a low turbulence level and a wide flow velocity range, while for the latter the boundary layer chamber is deployed, where it is possible to perform tests in several turbulent wind conditions. The wind turbine model is equipped with individual pitch actuators, therefore some tests are performed to verify the synergy between the passive BTC solution and the active IPC strategy.

The chapter is organized according to the following plan. First, the description of the scaled experimental facilities used for the aerodynamic and load characterization are described, therefore the scaled tower-nacelle model with its sensorization and the hard real-time module, then the wind tunnel of *Politecnico di Milano* with its facilities for testing of aeroservoelastic models. Then, the wind tunnel testing activity for the aerodynamic characterization is described, and the activity for the load characterization, including tests and post analysis is shown.

6.2 Scaled wind testing facilities

The scaled wind turbine model consists of three scaled multi-MW blades with BTC, mounted on the hub of a scaled tower-nacelle system by two bearing, and a zero-backlash pitch motor with built-in relative encoder housed at the root is used for pitching. This system is realized with the goal of supporting such activities of validating aeroelastic models and control laws. All its sub-components are also capable of representing the mutual interaction of aerodynamic, elastic and inertial forces, as required by the scaling laws. Table 6.1 reports the main geometrical parameters of the model.

Table 6.1: *Main geometrical parameters of the wind turbine model.*

Parameter	Value
Rotor diameter	1.913 m
Up-tilt angle	6°
Cone angle	4°
Over-hang	≈ 80 mm
Nacelle height	≈ 90 mm
Nacelle width	≈ 90 mm
Nacelle length	≈ 215 mm
Tower height	1.723 m

The shaft is mounted on other two bearings, held by a rectangular carrying box that features the main structural member of the nacelle. Behind the nacelle carrying box, the three electronic control boards of the pitch actuators are mounted on the shaft and therefore rotate with it. A 36-channel slip ring occupies the aft part of the nacelle, held in place by a plate and connected to the main carrying box by four rods. The tower is realized with a tube whose stiffness is designed so that the first fore-aft and side-side natural frequencies of the nacelle-tower group of the scaled model be close to the ones of the multi-MW machines. At the top of the tower is housed the torque actuator, connected to the shaft through a pair of conical spiral gears, with a reduction ratio of 0.5.

At the tower base, the model is mounted on a balance, that provides measurements of the three force and three moment components. Finally, aerodynamic covers of the nacelle and hub ensure a satisfactory quality of the flow in the central rotor area.

The model is highly sensorized. At the root of one blade, strain gauge bridges provide measures of the bending moments and their output voltages are conditioned and A/D converted by an electronic board placed in front of the rotor hub. The presence of the 4x1 optical coupler (installed in a special composite reel frame on the rotor hub) allows the transmission of the optical signals of the embedded FBGs from the rotating part to the fixed one of the model through a special Fiber Optic Rotary Joint (FORJ) mounted coaxially with the electrical slip ring.

Onboard sensorization of the machine provides the ability to measure, with sufficient accuracy, the aerodynamic torque and the bending loads on the shaft by means of strain gauges, whose output voltages are conditioned and A/D converted by the

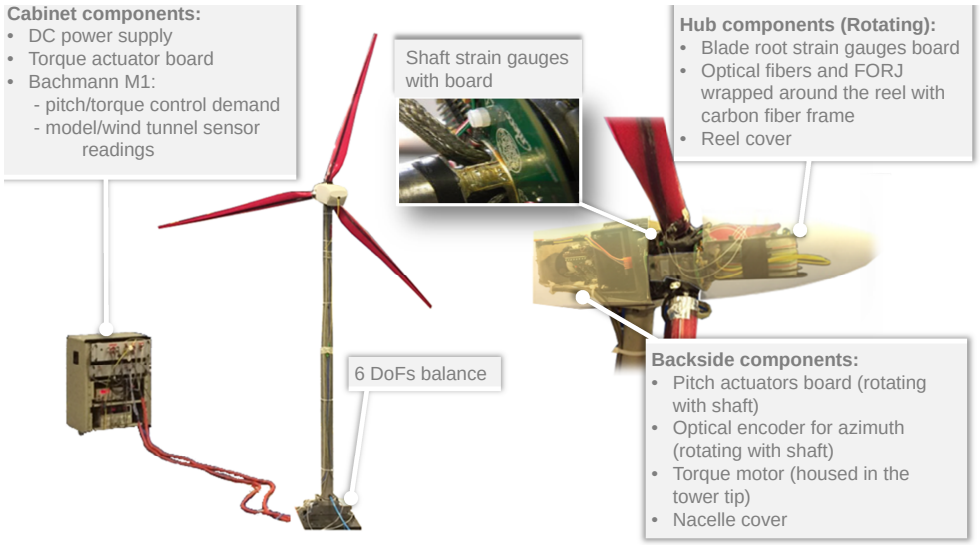

Figure 6.1: *Wind turbine model with its main features.*

electronic board placed between the rotor and the nacelle. An optical rotary encoder disk dragged from the shaft, mounted behind the two bearings, provides for rotor azimuth position. The model is controlled by a hard real-time module implementing a supervisor of the state machine and the pitch-torque control laws. The control action is performed by varying the blades pitch and the electrical torque provided by the generator. For each blade, the pitch actuation is demanded to a small brushed motor driven by its own control board mounted on the shaft and rotating with it. The feedback is based on the motor built-in encoder measures. The torque actuation is instead provided by a brushless motor lodged in the tower top and driven by a 4-quadrant control board, so as to allow the motor operating also as a generator. These actuation devices enable the testing of modern control strategies with appropriate bandwidth and a reasonable rendering of the principal dynamic effects of servo actuators. The electrical onboard sensors signals, together with the wind flow measurements from the wind tunnel, are sampled by the analog acquisition modules of the industrial `Bachmann M1` hard real time system URL `http://www.bachmann.info` at the sampling frequency of 250 Hz. The machine states and the pitch-torque control laws are compiled into the *M1* CPU, while the control outputs, represented by pitch and torque demands, are sent to the actuators control boards via *M1* CAN module. The overall model is illustrated in Figure 6.1, where the main features are highlighted.

The testing activity is performed in the wind tunnel of *Politecnico di Milano*, arranged in a vertical layout, whose Figure 6.2 shows the configuration for testing of wind turbine models. At the bottom level, the aeronautical section is useful for the aerodynamic characterization. It is featured of a low turbulence ($< 0.1\%$) level and a wide flow velocity range (up to 55 m/sec), with a cross sectional chamber of 4 m $\times$ 3.84. At the top level, the boundary layer section has a wider cross area of 13.84 m $\times$ 3.84 m and a length of 35 m. This feature allows to perform tests with

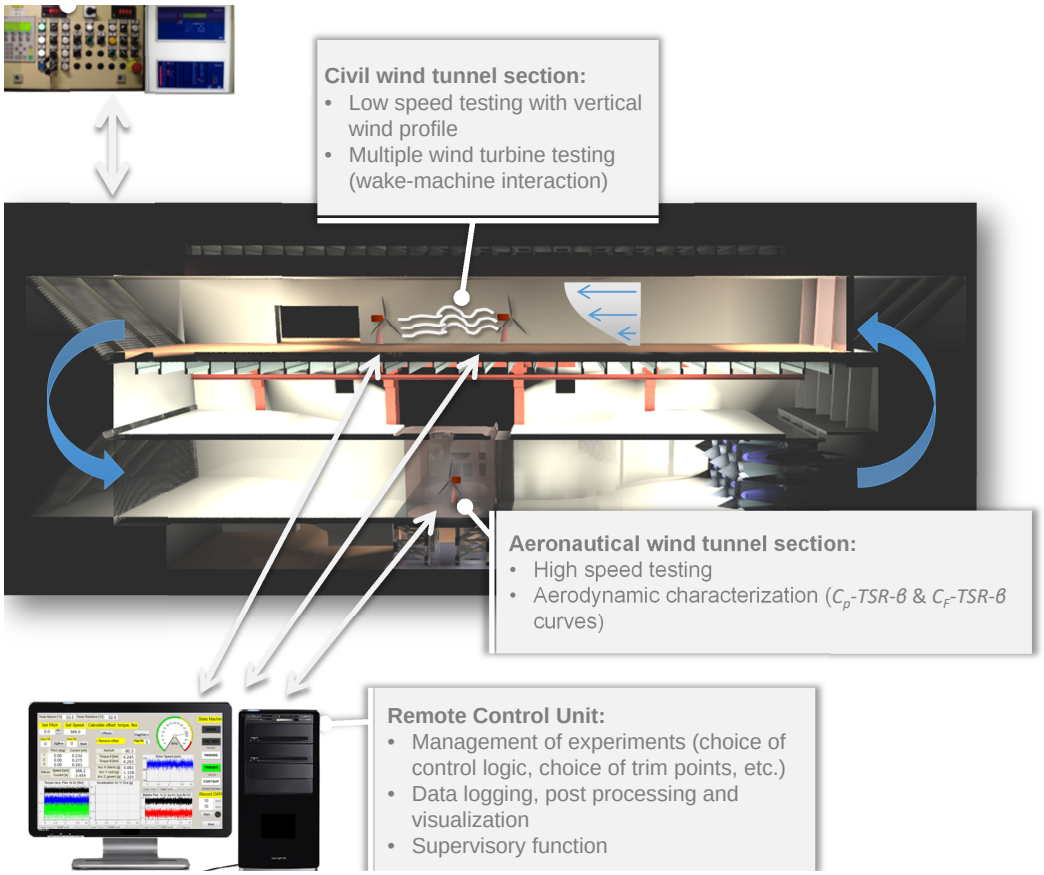

Figure 6.2: *Wind tunnel layout with testing management system.*

low blockage effects. In this test chamber, that is mainly used for civil and wind engineering applications, the boundary layer and the high turbulence level are introduced with the use of appropriate *spires* installed at the inlet of the chamber. The dimensions of the chamber allows testing of multiple wind turbines so as to be able to simulate wind farm configurations. Both the chambers can be used simultaneously in a closed loop configuration. The wind tunnel is equipped with wide range of devices for measuring the physical quantities of the environment and for controlling the flow conditions, as well as with control rooms that allow to supervise the models and conducting the tests. A Remote Control Unit is used for managing the model during the experiments via a GUI interface directly linked to the Bachmann M1 of the model. The interface allows the visualization of the main measurements, i. e. signals from shaft strain gauges, blade strain gauges, azimuth position and rotor speed, pitch position, wind speed, environment temperature, density etc., but also to switch among the several operation modes. A wind tunnel operator is capable of controlling the wind tunnel environment through the wind panel control unit.

6.3 Aerodynamic characterization

A first test campaign is performed in the aeronautical section of the wind tunnel, with the goal of evaluating the aerodynamic characteristics of the model with the BTC blades. This step is necessary for the following reasons:

- To evaluate the impact of the BTC technology on the performances, in terms of power production capability and thrust;
- To create the aerodynamic database useful for setting correctly the control strategy;
- To compare the results with those obtained by simulating the multibody model in the numerical environment.

The wind turbine is installed on a 6 DOFs balance used to acquire the thrust. The balance is in turn installed on a turntable that allows for a precise orientation of the rotor in the airflow direction. A laser system is used to align correctly the nose to the middle position of the flow inlet section.

The chamber is equipped with distributed pressure probes and temperature sensors, and a pitot tube is installed in a certain position ahead of the model. While the thrust measurement is provided by the balance, strain gauges on the shaft are used to acquire the torque. The torque and thrust are evaluated in several static wind conditions, by combining different wind speeds, rotor speeds and pitch angles, with the goal of characterizing the $C_F - \lambda - \beta$ and $C_P - \lambda - \beta$ curves.

To set-up the test matrix with the choice of wind speeds, pitch angles and the tip speed ratios, the aeroservoelastic model of the machine is used, and the tests are first performed in the multibody environment, in order to understand the most significant $\lambda - \beta$ points to be tested. Once the testing grid points are determined, the wind tunnel tests are performed. The resulting thrust and power coefficients are shown in Figure 6.3, with thick solid lines, both corrected from non negligible blockage effects ($\pi R^2 / A_{\text{chamber}} = 0.189$) with the disk actuator method presented in [98]. The maximum power coefficient is approximately 0.39, reached with tip speed ratio around 7.5 and blade pitch around -5°. The curves trend are in accordance with those of the multibody simulations, whose the results are reported in the same graphs in dot-dashed lines, with a mismatch that becomes relevant at low pitch angles. This mismatch is mainly caused by the differences between the effective structural properties of the blades and the nominal implemented in the multibody model, not yet updated with the identified values, where the higher tendency to twist is shown by the coupling coefficient α_s in Figure 5.20, thus affecting the local incidence of the blade airfoils. The updating of the blade model with the identified structural properties will help address this mismatch.

The power coefficient is compared with that from a rigid rotor (RGD), without BTC and with the same diameter and blade geometry. The results are reported in Figure 6.4. This rotor, equipped with low-flexible blades in carbon fibers, shows a maximum power coefficient of around 0.4, reached with a tip speed ratio around 7.5, and with a pitch angle around -1.7°. The comparison highlights what is expected: the BTC does not significantly affect the power production capabilities, but

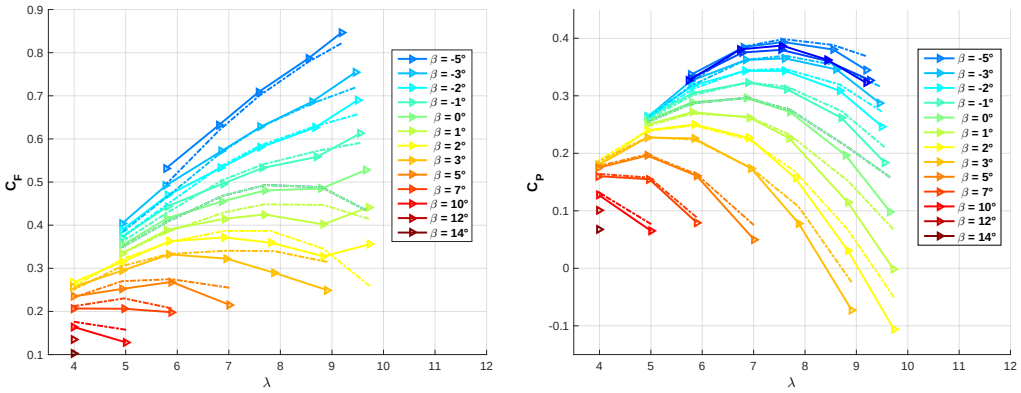

Figure 6.3: *Thrust and power coefficient of the rotor with bend-twist coupling. Experimental with thick solid lines, numerical values with dot-dashed lines.*

the maximum performance is obtained at lower pitch angle, which compensates for the reduction of the local incidence of the blade airfoils caused by the twist-to-feather.

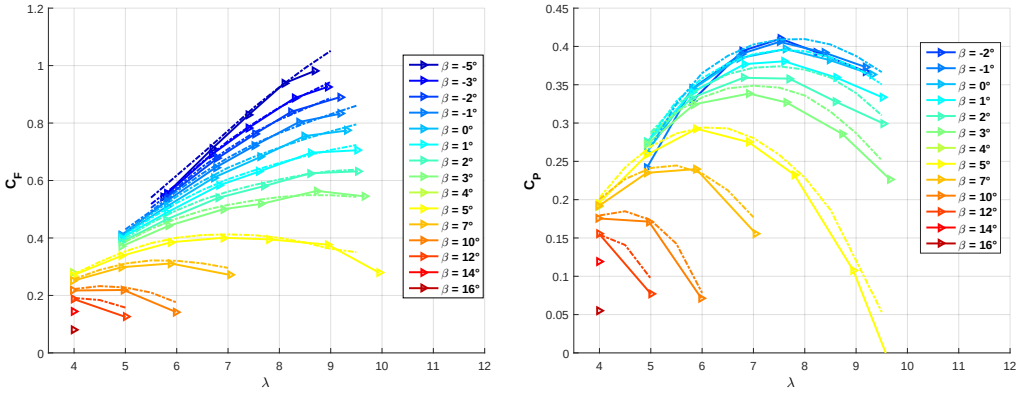

Figure 6.4: *Thrust and power coefficient of the rotor without bend-twist coupling. Experimental with thick solid lines, numerical values with dot-dashed lines.*

6.4 Load characterization

The second test campaign is performed in the boundary layer section of the wind tunnel. The goal is to characterize the model in terms of fatigue loads, and thus to asses the capability of the BTC.

Figure 6.5, shows the general arrangement of the tests. The scaled wind turbine with BTC is mounted on the 6-DOFs balance, fixed at the floor of the chamber. By the use of the laser system, an accurate alignment with the wind flow is guaranteed. In front of the model, approximately half diameter ahead, a pitot tube was installed at the height of the hub, in order to measure the wind speed. The cabinet providing the hardware equipment for the control system was also put in the test chamber far enough to not aerodynamically interfere with the tests. A model with RGD blades

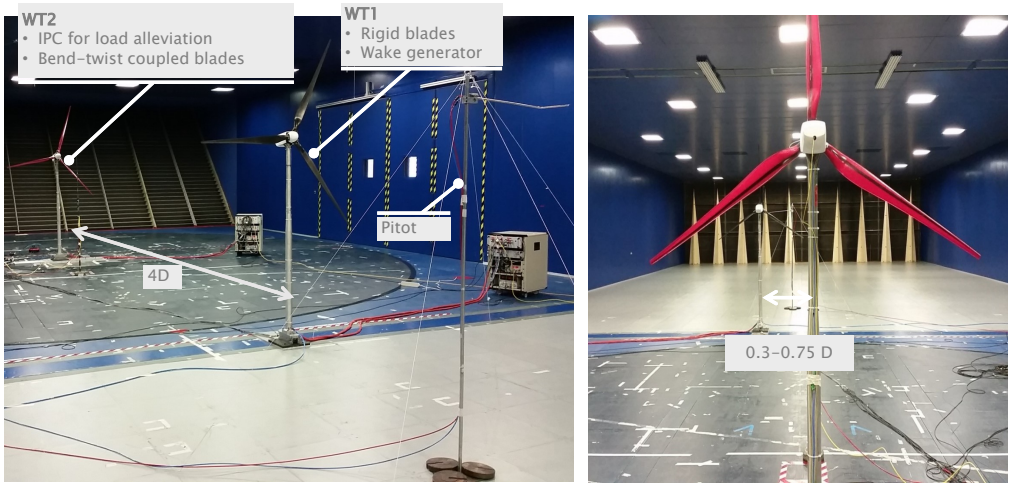

Figure 6.5: *Partial wake tests configuration: RGD in front, BTC model in downwind position*

is put in the test chamber in front at a distance of four diameters, with the scope of generating repeatable wake conditions (for details on the regulation strategy of the models, please refer to Section 6.4.1).

The 6-DOFs balance was used to acquire the thrust, the bending moment and the yawing moment at the tower root. The strain gauges at the shaft provided the torque and the bending moment measurements, while the FBG sensors measured the loads of one blade at approximately one third of the span. The experiment consisted in several tests at different wind speeds and partial wake conditions, with the goal of exploiting the loads in some relevant points of the operative envelope.

The standard turbulent wind to which HAWTs are subjected is described by the certification standards in terms turbulence integral length, turbulence intensity and power spectral density (PSD). The scaling of the model requires also the scaling of the turbulent wind, by using the scaling factors of reported in Table 5.1.

In such wind tunnel tests the turbulent boundary layer is generated by passive vortex generators (*spires*) with triangular shape, placed at the inlet of the chamber, with the scope of generating conditions similar to the atmosphere. In a previos work [99] it was measured that with a mean hub wind speed of 6 m/s and with a certain partialization of the wind tunnel engines it was possible to obtain a boundary layer power coefficient[1] $\alpha_{bl} \approx 0.33$. This value is high if compared to the atmospheric one ($\alpha_{bl} \approx 0.2$) but assures a stronger wind shear and a complete immersion of the model in the boundary layer.

The integral length scale and the intensity measured in the wind tunnel at the hub height are respectively 1 m and 12%. These values do not exactly match those from the scaling (respectively 0.65 m and 18-21%, according to [39]) but are quite comparable. Figure 6.6 reports the comparison between the PSD of the wind tunnel turbulent wind and the asymptote required by [39], for a wind speed of 6 m/s.

The aforementioned considerations bring to consider the turbulent wind generated by the wind tunnel acceptable for the scope of assessing the BTC effectiveness

[1]The power coefficient defines the wind shear profile by the formula $\frac{U}{U_e} = (\frac{z}{\delta})^{\alpha_{bl}}$, where U_e is the external wind speed and δ the boundary layer thickness

in reducing the fatigue loads, whose most of the energy is concentrated within a bandwidth up to 3xRev.

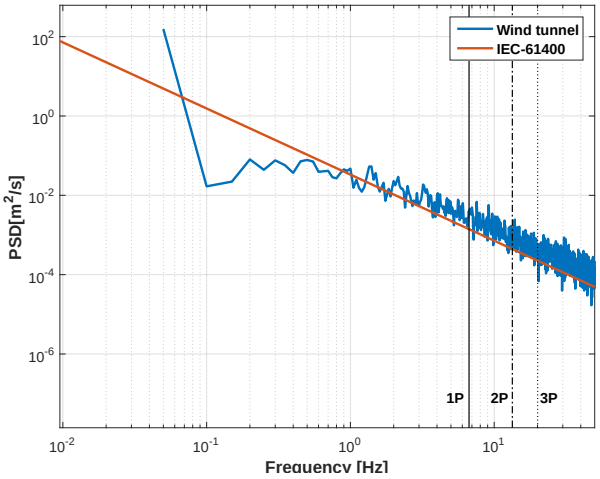

Figure 6.6: *Hub height wind speed power spectral density at 6 m/s*

6.4.1 Model control strategy

From the knowledge of the rotor aerodynamics it is possible to set-up the control law for the power production operation. A look-up table is used for the generator torque in region II, whose values are scheduled in function of the rotor speed, following the feed-forward law: $T = k_{\text{opt}}\Omega^2$, where the constant $k_{\text{opt}} = \frac{1}{2}\rho\pi R^5 \frac{C_{P_{\text{Max}}}}{\lambda^3_{C_{P_{\text{Max}}}}}$ is imposed using the data of the rotor aerodynamics. In order to allow a smooth transition between region II and region III, where the torque reaches the rated value, a rotor speed PI controller with anti wind-up scheme within upper and lower bounds is implemented as following:

$$T_{g\text{Min}} = k_{\text{opt}}\Omega^2 \tag{6.1a}$$

$$T_{g\text{Max}} = T_{g\text{Rated}} \tag{6.1b}$$

$$T_g = K_{P_T}(\Omega - \Omega_{\text{R}}) + K_{I_T}\int(\Omega - \Omega_{\text{R}}) \tag{6.1c}$$

$$(\textbf{if} \quad T_{g\text{Min}} < T_g < T_{g\text{Max}}) \tag{6.1d}$$

Similarly, the collective blade pitch control in region II is set to that allowing the maximum power coefficient $C_{P_{\text{Max}}}$, hence assuring the maximum aerodynamic performances. In region III the pitch motion is driven by the rotor speed through a PI controller with anti wind-up scheme, permitting to reject the excess wind power. The maximum value is set to the value $\bar{\beta}$ corresponding to the flag position, in order to allow the recovery procedure from an emergency shutdown. The control law on

the collective pitch is then the following:

$$\beta_{\text{Min}} = \beta_{C_{P_{\text{Max}}}} \tag{6.2a}$$

$$\beta_{\text{Max}} = \bar{\beta} \tag{6.2b}$$

$$\beta = K_{P_\beta}(\Omega - \Omega_{\text{R}}) + K_{I_\beta} \int (\Omega - \Omega_{\text{R}}) \tag{6.2c}$$

$$(\textbf{if} \quad \beta_{\text{Min}} < \beta < \beta_{\text{Max}}) \tag{6.2d}$$

Table 6.2 reports the values used for the control system scaled from the 5 MW RWT.

6.4.2 Test description

The downwind model is tested in several no-wake/partial-wake conditions. For the no-wake (NW) cases the upwind turbine is kept turned off and the rotor is invested by the turbulent wind generated with the spires. Two wind speeds are used, 5 m/s and 6.5 m/s, corresponding respectively to region II and region III scenarios. For the partial-wake (PW) cases the downwind model is placed at four different positions away from the wake axis. By referring to Figure 6.5, 0.30, 0.45, 0.60 and 0.75 diameter distances are used. All the tests are repeated three times:

1. the downwind model is equipped with rigid blades (RGD model), in order to have the baseline for the load comparison;
2. the downwind model is equipped with aeroelastic blades with (BTC model), to characterize the loads of the passive solution and compare with baseline;
3. the downwind model with BTC is tested in synergy with the individual pitch controller (BTC+IPC model), to verify the synergy of the integrated passive (BTC) / active (IPC) load reduction solutions.

Table 6.2: *Models controller settings.*

Model:	**RGD**	**BTC**
Rated wind speed [m/s]	5.4	5.4
Rated rotor speed [rpm]	380	380
Rated power [W]	124.9	124.9
Rated torque [Nm]	3.14	3.14
Torque Look-Up k_{opt} [Nm/(rad/s)^2]	1.45x10^{-3}	1.35x10^{-3}
Min. pitch $\beta_{C_{P_{\text{Max}}}}$ [deg]	-1.7	-5
Max. pitch $\bar{\beta}$ [deg]	90	90

Each test is run for 60 seconds, corresponding to a scaled-up activity of around 30 mins. Figure 6.7 shows the mean power produced by the downwind models in the tests selected for the comparison. The other cases are not considered due to the significant power production differences caused by a wrong setting of the controller. Blue bar represents the RGD model, the red bar refers to the BTC, while the yellow

bar identifies the hybrid BTC+IPC model. For these cases the power mismatch remains under 1%.

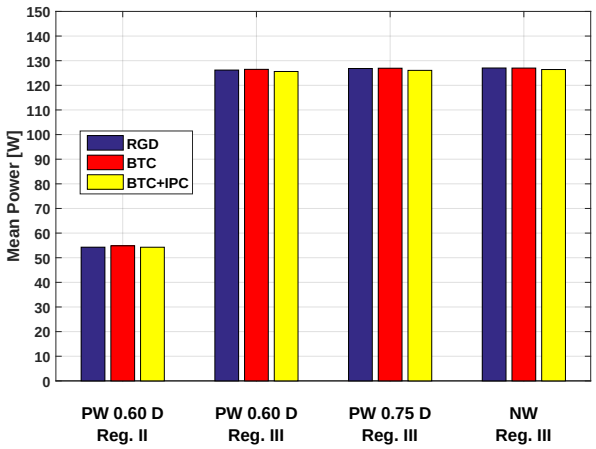

Figure 6.7: *Mean power produced by the downwind model.*

6.4.3 Fatigue analysis

The test campaign is conducted for assessing the fatigue load mitigation capability of the BTC. A comparison between the RGD and BTC model is first carried out, then the hybrid BTC+IPC is considered. The data related to the hub come from the strain gauges at the shaft, while the tower loads are acquired by the 6-DOFs balance. The BTC blade loads coming from the FBG sensors are analysed next for some considerations on the hybrid BTC+IPC solutions. All the loads signals are pre-processed with a low-pass Butterworth filter of the 8-th order at a cut-out frequency of 50 Hz, which is sufficient high to guarantee the spectra analysis for up to the 8xRev.

Figure 6.8, Figure 6.9 and Figure 6.10 refer to the NW test case. Figure 6.8 shows the frequency response of the shaft bending moment in the direction of the computed highest DEL (*physical DEL*). Here, many characteristics of the models can be observed. Looking at the RGD, marked with blue line, the 1^{st} and 2^{nd} xRev frequencies are clearly visible. The other emerging load components are in correspondence to the spurious tower frequencies: ω_T, $\omega_T \pm \Omega$, $\omega_T \pm 2\Omega$, $\omega_T \pm 3\Omega$, where the tower frequency ω_T in side-side direction is 7.8 Hz. In fore-aft direction the resonant frequency is slightly higher (around 8.6 Hz), but is highly damped, and therefore the associated load components is not visible. Looking at BTC model, marked with red line, it appears that the BTC damps out the loads associated to the tower resonant frequency. Furthermore, the bending moment is mitigated over the bandwidth up to the first blade flapping mode frequency, at around 23 Hz.

At the 1xRev the load of the BTC model appears higher, for the reason that the rotor weight with its arm with respect to the strain gauge position, generates a bending moment at this frequency. It is verified that by removing this load source from the measures of both the RGD and the BTC models, the 1xRev component

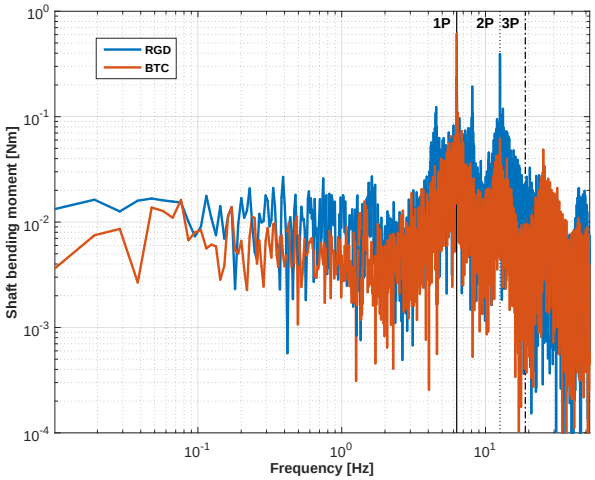

Figure 6.8: *NW Reg. III test. Shaft bending moment (rotating). Frequency response. The black vertical lines indicate the frequencies of 1xRev, 2xRev and 3xRev.*

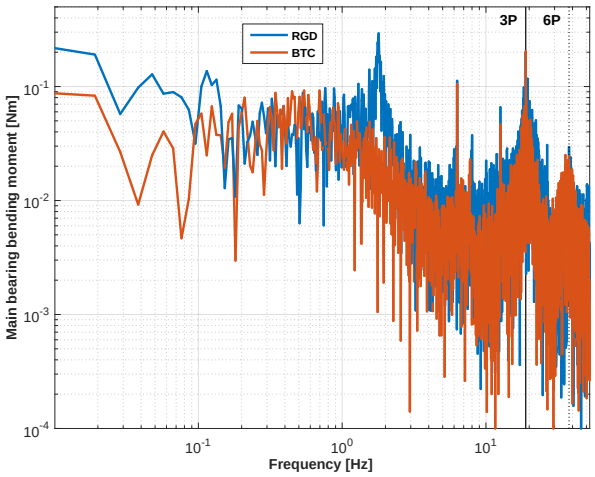

Figure 6.9: *NW Reg. III test. Main bearing bending moment (fixed). Frequency response. The black vertical lines indicate the frequencies of 3xRev and 6xRev.*

of the latter becomes lower. Infact, the BTC has the capability of mitigating the aerodynamic load sources. Since at 1xRev the main aerodynamic load is the wind shear and is phased of 180° with respect to the rotor weight, and appering the two load sources very similar in magnitude, they tend to compensate each other. When the wind shear effect is reduced by the BTC, the rotor weight contribution is not opposed anymore, causing an increment of the total load.

The main bearing bending moment components are evaluated projecting the shaft components in the fixed reference system: the signals are first filtered from the mean value, which brought the rotor unbalancies, hence rotated by using the transformation of coordinates. Figure 6.9 shows the frequency response of the combined bending moment, -in the direction of the highest DEL- in the fixed reference system. The direction of the combined moment is close to the nodding for both the models. As expected, the more pronunciated peaks are multiples of 3xRev frequencies. Looking at the RGD model, there are some peaks corresponding to the 1xRev and 2xRev frequencies due to some small pitch misalignements and the turbulence instability, and the peaks at the tower resonant ω_T frequency with related spurious at $\omega_T \pm n\Omega_R$. The BTC seems to damp out some of the load components and mitigate in the overall spectrum.

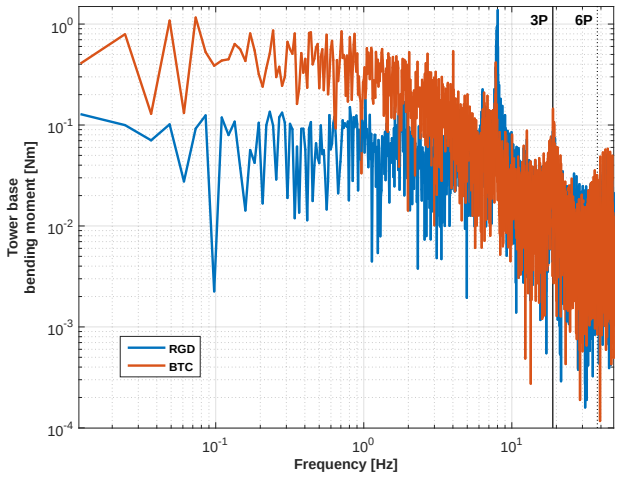

Figure 6.10: *NW Reg. III test. Tower base bending moment. Frequency response. The black vertical lines indicate the frequencies of 3xRev and 6xRev.*

Figure 6.10 reports the combined bending moment measured at the tower base. The spectrum is corrected from the rotor unbalancies measured by the shaft strain gauges. In this case the direction of the highest DEL is different. The RGD model shows a more pronunciated tower side-side resonant frequency, since the direction is close to the side side component, while the spectrum of the BTC is close to the fore aft, showing higher loads component at lower frequencies.

Figure 6.11 reports the specrtum of the combined shaft bending moment for the PW 0.60 D Reg. II test. Here the load attenuation capability of the BTC seems to be reduced at low frequencies, but still remains important at higher frequencies (from 2xRev to around 23 Hz, corresponding to the out of plane frequencies).

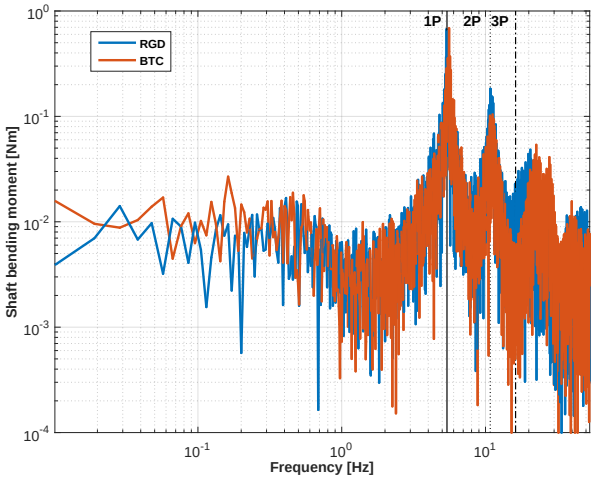

Figure 6.11: *PW 0.60 D Reg. II test. Shaft bending moment (rotating). Frequency response. The black vertical lines indicate the frequencies of 1xRev, 2xRev and 3xRev.*

Figure 6.13 reports the amount of DEL and ADC reduction in all the test configurations, evaluated in 60 seconds of testing (which corresponds to around 30 mins of scaled-up activity). The DEL is calculated by Rainflow-counting algorithm. For bending moments the *physical* DEL is considered. Then, per each direction the DEL is calculated and then the higher is selected. Looking at top graph, which refers to the comparison using the BTC without enabling the IPC, the results related to the NW tests show important reductions (between 20% and 50%) for all the loads considered, which translates in a potential increase in life-time of the components, and a significant saving of ADC, remarking good synergy with the collective pitch system. The results related to the PW tests confirm that the BTC effectiveness is reduced. The case PW 0.60 D Reg. II shows no reduction on the rotating shaft bending moment DEL, since the low frequencies loads component, i. e. those with the higher load energy, are not affected by the BTC, which seems to be still effective in reducing the main bearing moment of around 5-15%. PW 0.60 D Reg. III and PW 0.75 D Reg. III show similar results: in the case of PW 0.60 D Reg. III the shaft bending moment is slightly increased, due to the higher 1xRev load, while for the main bearing a reduction of around 10-20% is observed. In all the cases a reduction on the shaft torque is observed, which translates in an improved power quality. The BTC has shown an important fatigue load mitigation over the spectrum. The twist to feather of the blade reduces the effective angle of attack of the airfoils and therefore the aerodynamic load fluctuation. It appears that in some spots mitigating the aerodynamics may not be beneficial at all. Indeed, it is shown that in some cases the inertial loads, like the rotor weight, are also important for the fatigue. As the BTC does not have the ability of reducing the overall load, but the only aerodynamic one, a possible improvement of the load reduction may be exploited by using the BTC in synergy with the active IPC system.

The IPC implemented here has the primary goal of cutting out the 1xRev load on the shaft. The implementation, whose the details can be found in [36], follows

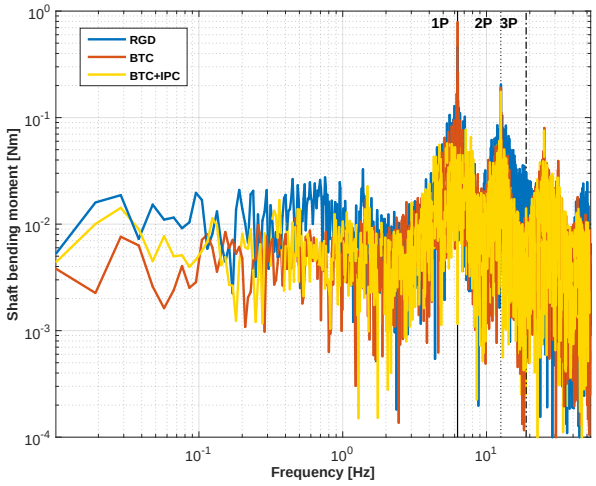

Figure 6.12: *PW 0.60 D Reg. III test with the hybrid BTC+IPC model. Shaft bending moment (rotating). Frequency response. The black vertical lines indicate the frequencies of 1xRev, 2xRev and 3xRev.*

the method presented in [26]. The control is feedback on the shaft bending moment components, that are first rotated in the fixed reference system and then a filter cuts the components over 0.5 Hz. For its intrinsic working principle of cutting out the shaft 1xRev load, one expects a positive synergy with the BTC. In Figure 6.12 the frequency response of the shaft bending moment at PW 0.60 D Reg. III case is proposed with the hybrid BTC+IPC model. It is possible to see how the load specrtum is very similar to the BTC-only model, except at 1xRev, where the peak is cut out. The synergic effect of the BTC with the IPC is then clearly visible. The synergy determines a consistent DEL reduction in the shaft bending moment, as shown in Figure 6.13 at bottom, with also some little improvements on the other spots, at the expenses of the increased ADC.

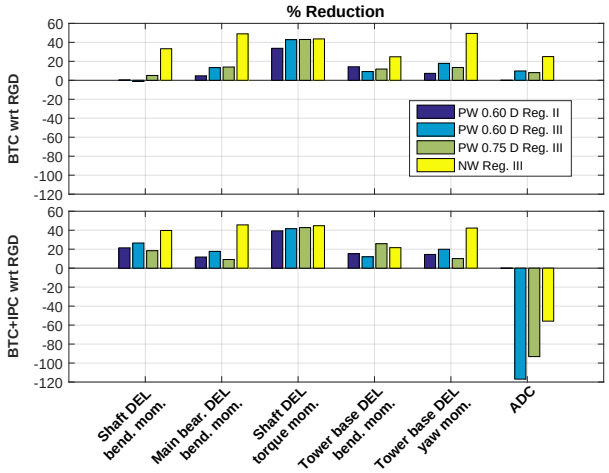

Figure 6.13: *DEL reduction with respect to the RGD. BTC only at top, BTC+IPC at bottom.*

Figure 6.14 shows the blade bending moment measured with the FBG sensors for the hybrid BTC+IPC and the BTC-only model. Here the multiples of the 1xRev are remarked up to the 8^{th}, with also the first flapping frequency that is located at around 23 Hz. The spectra are very similar, the hybrid model seems to slightly mitigate in the overall.

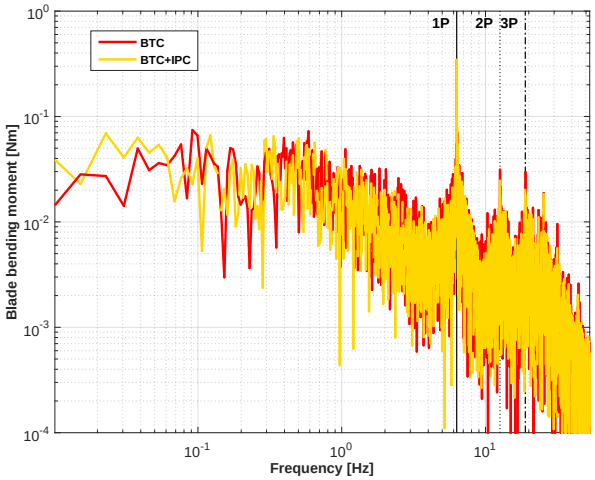

Figure 6.14: *PW 0.60 D Reg. III test with the BTC and hybrid BTC+IPC model. Blade bending moment. Frequency response. The black vertical lines indicate the frequencies from 1xRev to 7xRev.*

The 1xRev is instead increased: since the IPC system works with the goal of cutting out the 1xRev load at the shaft, an effective way to do it is to overload the blade so as to mitigate the inertial load by increasing the unphased aerodynamic load on the shaft. This way of working may impact on the blade life-cycle, since the fatigue load may increase.

Possible ways to mitigate this phenomenon are:

- using the blade loads as feedback for the IPC, instead of the shaft bending moments. This would require the installation of strain gauges at the three blade roots, not available in the tests conducted.
- since the cost of using the IPC is an increased ADC, and the BTC-only helps to reduce it, as shown in Figure 6.13 at bottom, a better synergy is achieved by tuning the IPC using only the amount of ADC reduction given by the BTC.

6.5 Synopsis

A scaled model of large conceptual multi-MW wind turbine featured with BTC is developed and characterized. Test campaigns are conducted in the wind tunnel to characterize its aerodynamics and loads. Based on the results obtained, the following considerations are drawn:

- The test in the aeronautical section of the wind tunnel showed little differences

with respet to the rotor without BTC in the power coefficient, with the minimum pitch angle moving from -1.7 to -5 degrees.

- Turbulent partial wake tests, conducted in the boundary layer section of the wind tunnel, highlight the capability of the BTC to reduce the fatigue loads on the main bearing and the tower base, but the inertial load contributions determine an increase bending moment on the shaft. Also the ADC is reduced considerably. The use of hybrid model IPC+BTC showed a further reduction of the fatigue loads, and a cut-out of the 1xRev component at the shaft, at the cost of an increased ADC and loads at the blade root.

CHAPTER 7

Conclusions and remarks

In this thesis dissertation, blade solutions for load mitigation are investigated. At the beginning, it is revised how technologies for load reduction implemented on the blades can be either passive and active and distributed/full-blade span. The thesis investigates beyond what has been already conceived for the wind energy systems in the context of load reduction, focusing on the study of the potentialities of passive solutions to mitigate the loads and to work in synergy with active architectures, with the goal of reducing the Cost of Energy.

7.1 Distributed devices for load alleviation

Blade distributed devices for HAWTs are widely exploited in the literataure. When used actively, i.e. when they require sensors and actuators, they tipically increase the complexity of the system, bringing sometime to unacceptable higher costs in terms of installation and maintenance, with possible negative effects when weighted in the Cost of Energy. However, at present, the most mature applications appear to be the ones based on trailing edge flaps. [5–7], although also alternative solutions based on micro-tabs and compliant structures have been considered [8, 9]. Passive distributed devices apper to be very promising in the development of larger wind energy systems, since they have similar performances to the active ones, without necessitating of further sensors or actuators. Passive distributed techniques were first developed for aeronautical applications. Passive trailing edge and free pitching tip were intensively exploited numerically and experimentally. Although these studies did show the general ability of passive devices in decreasing loads, these advantages are typically offset by an increase of weight, to the point that passive

solutions do not seem nowadays to be commonly employed in aeronautical applications. In fact, in aeronautical applications higher levels of complexity are acceptable if they entail superior performance and/or weight savings. The situation appears somewhat different in the wind energy field, where the increased weight is certainly a concern, but the main and often unique driver is the Cost of Energy. In this case, availability and maintenance costs are of a paramount importance. Therefore, for wind energy applications a passive solution might be more appealing than an active one, if the former implies greater simplicity, robustness and ease of repair than the latter. Passive distributed devices are based on spring-mass system principles, and react to the loads by different means, depending on the type of approach adopted for their tuning. Indeed, as this thesis dissetation showed throught the Chapter 2-3-4, the working principle of such devices, which can be either flaps or free pitching tips, depends on the position of the hinge line, with respect to the device aerodynamic center and center of gravity. In the specific, if the hinge line lies in front of the device aerodynamic center, its response is primarily driven by the aerodynamic forces. In this case, changes in pressure distribution due to local angle of attack fluctuations produce changes in the aerodynamic moment about the hinge line, that in turn counteract the originating disturbance. In this case, no added masses are typically necessary, as a proper tuning is obtained by purely aerodynamic means. On the other hand, if the hinge line is close to the aerodynamic center of the device, the aerodynamic hinge moment varies little with respect to changes in the angle of attack. This way, the device is relatively insensible to aerodynamic load fluctuations. Motion must therefore be induced by using inertial loads, typically by displacing the device center of gravity from the hinge line, possibly with the use of tuning masses. The advantage of this solution is that the device does not respond to deliberate changes in angle of attack, as the ones induced by the wind turbine control system. A side effect of this approach can be the excessive reduction of the machine modal frequencies due to the increased blade mass, which in turn puts a limit on the use of the offset masses.

Chapter 2 proposes a preliminary study of the passive distributed device concept for load mitigation. The idea, implemented by means of a freely moving flap, has been investigated with regard to a conceptual 10 MW machine. Ad-hoc simulation models were developed to conduct the present study. The models include a typical section of the blade with unsteady aerodynamics described by thin airfoil theory in the frequency and time domains. This model was used for sizing the main parameters of the passive flap and to evaluate the system response to angle of attack inputs. A tuning procedure of the flap parameters was presented, that maximizes DEL mitigation while ensuring stability. The typical section was coupled to a closed-loop aeroservoelastic model of the wind turbine. This second model was used for providing angle of attack driving inputs to the typical section, and to estimate power production by correcting a posteriori the blade aerodynamic forces based on the typical section results. Various analyses were conducted to evaluate relevant performance metrics with and without the passive flap. The results obtained seemed to indicate that the proposed concept has some interesting potentials:

- The optimal flap parameters are very reasonable, and do not require excessive

size nor masses.

- Fatigue load alleviation is very noticeable, and accompanied only by modest AEP reductions
- The behavior is robust and consistent within the entire operating regime of the wind turbine, without necessitating of scheduling of system parameters with respect to wind speed or other quantities. To this end, an instrumental role was played by a sizing of the flap that performs an approximate cancellation of the effects due to centrifugal forces and non-circulatory aerodynamics.
- The solution is compatible with standard active blade pitch control strategies, routinely adopted on board modern wind turbines. In fact, differently from other passive flap concepts, the present device does not respond to deliberate changes in angle of attack due to active blade pitching.
- The flap concept appears to be applicable without the need for radical changes in the design of blades (although, to fully exploit the benefits of the passive device, it is expected that a passive-flap-equipped blade will have to be re-designed, for example by increasing its span, reducing its weight, or resizing some of its components).
- There is the potential also for the reduction of ultimate stresses during violent transients, as in emergency shutdown procedures.

The continuation of this study is conducted in Chapter 3 making use of more sophisticated simulation models, whereby the passive flap is implemented within a complete aeroservoelastic model of the machine, with the scope of demonstrating the effectiveness of the system in high-fidelity simulation tool. Here the passive flap effectively works in synergy with the wind turbine, accounting for large deformations and the complex geometry of the machine. Additional loads were included, such as gravity and centrifugal non-linear effects. Multiple scenarios and load cases were considered to characterize the load mitigation of the passive flap system, as required by the certification standards [38, 39]. The most critical design loads cases were simulated, including possible device faults scenarios. The sizing of the passive flap was performed with two flap extents respectively 10% and 15% of the blade span. The overhang was selected in order to obtain an adeguate level of aerodynamic balancing, necessary to avoid any aerodynamically driven response, thus the flap response does not respond to any deliberate changes in the blade pitch control system, therefore limiting the interaction with the active control strategy implemented on-board. The tuning of the device was a matter of reducing as much as possible the fatigue loads within the operating range of the machine, therefore normal turbulent wind conditions in a comprehensive simulation environment were performed first to identify the best combinations of offset mass and distance from the hinge line, necessary for the inertially-driven response to the load fluctuations. The cautious selection of the hinge preload was also necessary for limiting the AEP loss due to the blade camber modification introduced by the passive flap, which caused a reduction of the rotor efficiency, necessary below the rated condition. The

load analysis has considered both fatigue and ultimate loads, including also device fault conditions, following accepted standard certification procedures. Based on the results of this analysis, the following conclusions may be drawn:

- The implementation of the passive flap system in the high fidelity multibody environment confirmed the potential of this concept in mitigating the loads on large conceptual wind turbines.
- The proposed passive flap solution improves on the baseline in terms of fatigue and ultimate load alleviation. These results might possibly be further improved by a more complete optimization of the devices, including their aerodynamic shape.
- The more significant effects on fatigue are reported at the tower base. This is due to the tower top acceleration that drives the passive flap deflection and smoothing of the airloads. The fatigue at the main bearing is also mitigated, and this is essentially due to the driven flap response by the blade flapping. The fatigue mitigation at the blade root appears to be very poor. A more detailed analysis on the blade root bending components reveals that an increased drag fluctuation induced by the flap deflection and the increased blade weight due to the installation of offset masses increases the bending moment in the edgewise. At the same time a considerable reduction of the bending in the flap wise is encountered. The blade torsion DEL is also increased, due to the increased pitching moment fluctuation generated by the passive flap deflection. This, in turn may lead to an increased fatigue on the blade pitch actuator, which by the way sees also a reduction of its duty cycle. Therefore a more complex analysis should be conducted for assessing the effective benefits.
- Ultimate loads see a considerable decrease at the three main spots, i. e. blade root, main bearing, and tower base. Therefore the passive flap system, even if not its primary function, appears to be lowering also the ultimate peaks. Furthermore, the increased flap extent showed that the peaks are further decreased.
- The device seems to not significantly interfere with the collective pitch/torque control system used for regulating the machine, although no re-tuning of the controller was performed. For both the flap extents, the load smoothing generated by the passive flap results in an apprecciable reduced duty cycle of the blade pitch actuator.
- The consequences of device faults are limited, with no effect on the ultimate design-driving loads. Indeed, by ranking the results, it seems that only with the flap extent of 15%, at tower base, the bending moment peak is comparable to those of the standard design conditions.

Chapter 4 investigates the load alleviation capabilities of a tip device, i. e. where the outermost portion of the blade rotates with respect to the rest of the blade. In particular, a passive solution is compared with semi-passive and active architectures. In

the passive and semi-passive configurations tip pitching is mainly driven by aerodynamic means, obtained by putting the hinge ahead of the device aerodynamic center, while for the active case the rotation is obtained with an actuator commanded by a feedback control law. Each configuration is analyzed and tested using a high-fidelity aeroservoelastic simulation environment, by considering standard operating conditions as well as fault situations. The passive solution achieves the simplest configuration because it does not involve active components, while the active tip requires sensors and servo motors and implements a feedback control algorithm. The semi-passive tip is in a sense in between the other two configurations, requiring active slow regulation of the hinge preload but no feedback control. The free motion of the passive and semi-passive devices is driven by the weathercock tendency of the tip due to a suitable chordwise location of its hinge, together with a restraining spring. These devices results in a passive decentralized control strategy powered by local fluctuation of the aerodynamic loads. The resulting tip pitching smooths out the airloads without incurring in AEP losses of any significance. Quite differently, the active tip implements a centralized IPC control strategy, that targets the nodding and yawing moments at the hub. The chapter described the preliminary sizing of all devices. The hinge preload and stiffness for the passive and semi-passive configurations were defined by an ad hoc procedure, while simple guidelines were reported for the tuning of the gains of the active tip system.

The devices were tested in a comprehensive simulation environment, with application to a conceptual 10 MW machine. The analysis considered both fatigue and ultimate loads, including also tip fault conditions, following accepted standard certification guidelines.

Based on the results of this analysis, the following conclusions may be drawn:

- All proposed tip devices improve on the baseline both in terms of fatigue and ultimate load alleviation, although to a different extent on different wind turbine components. The passive tip showes similar performances to tho other architectures, but achieved with simplier configuration, not involving active components, therefore it appears very interesting at the light of considerations on the Cost of Energy.

- The more significant effects on fatigue are reported at the blade root and tower base. For the passive and semi-passive devices, this seems to be attributable to a smoothing of the airloads. Ultimate loads see the largest decrease at the main bearing, while they are essentially unaffected on blade and tower.

- AEP losses are negligible, and none of the devices seems to significantly interfere with the collective pitch/torque control system used for regulating the machine, although no re-tuning of the controller was performed. For the semi-passive solution, the load smoothing generated by the tip results in a slightly reduced duty cycle of the blade pitch actuator.

- The consequences of a blade tip fault are limited, with no effect on the ultimate design-driving loads. The active and semi-active devices can be used to reduce blade sail area in stormy conditions. Although this technique did not reduced

ultimate loads on this specific machine, it might be beneficial on other wind turbines more significantly driven by storm conditions.

Further studies are clearly necessary before final conclusions may be drawn, although these initial results seem to be promising. In particular, the passive (and semi-passive) solution behaves nearly as well as the active one, at a reduced complexity. This might be interesting for applications were reliability, low cost of maintenance and high availability are at a premium, as in the offshore case.

7.2 Full blade span solutions

Full blade span solutions for load alleviation involve the response of the entire blade, and can also be distinguished between active and passive. Individual pitch control is a well known full-span active technique, being investigated for many years by the scientific community, and now is seeing an ever increasing acceptance by industry. It was widely prooven that individual pitch control laws [26–29] is very effective in reducing both the fatigue and ultimate loads. However the IPC shows a load reduction capability at the cost of an increased pitch activity, and this would require the design of more robust pitch actuators with effect on costs, complexity and maintenance. The full-span passive technique is based on the idea of designing a structure that, when loaded, deforms so as to induce a load reduction. A solution to achieve this structural behavior is to design blades with some degree of bend-twist coupling. This form of load alleviation is very attractive because of its passive nature, since there are no actuators which may fail, no moving parts which may wear out, all characteristics that are very interesting since simplicity, low maintenance and high availability are key for reducing the Cost of Energy. Furthermore, the literature has shown that, beside a significant load alleviation, the BTC induces also a consistent reduction of the pitch actuator duty cycle. In fact, since the blade self-reacts to wind fluctuations, less workload is demanded to the control system. This result is of potential interest, because it opens the way to a synergy between passive and active load alleviation technologies: since BTC and IPC can both mitigate loads, but BTC reduces ADC while IPC increases it, is clear that the systems can potentially work together in a way of maximizing the load reduction without graving to the pitch system robustness. At the light of the aforementioned considerations, the second parts of this dissertation is focused on the study of full blade span solutions for wind turbine load mitigation, throught scaled multi-MW models testable in the wind tunnel. The use of scaled models helps overcame the limitations regarding field testing, e. g. difficulties to have full and accurate knowledge of the environmental conditions and relevant costs and times of testing. In Chapter 5 ad-hoc design and manufacturing processes is described for the realization of scaled multi-MW blades with some degrees of BTC for testing in the the wind tunnel. Then, the realized blades are tested at bench for structural characterization. The results obtained are summarized in the following:

- The possibility of embedding low-intrusivity, high-accuracy FBG sensors with the scope of monitoring the load at some stations along the blade span is successfully exploited.

- The structural design, which was made with a multi-level structural blade design tool, showed good accuracy in matching the scaling requirements, since small errors of the scaled-up modal frequencies and the Lock Number are encountered. To evaluate the manufacturing, the blade is characterized at bench, by the use of static tests and modal tests with hammar. The modal analysis showed the modal frequencies and the Lock number remain close to the nominal design, with mismatches below 10%.
- The static tests showed the twist-to-feather behaviour of the blades structure. The BTC coupling is slightly higher in the manufactured blades. The structural characterization, i. e. the identification of the mass distribution and the structural stiffness, is performed using a robust SQP algorithm with the problem reformulated by SVD. The results are shown in terms of outputs (measures) of the laser measurements in the static tests, compared with the one obtained by simulation of the nominal blade multibody model and the final identified one. The latter improves the estimation of the measurements, highlighting the goodness of the identification procedure. The modal frequencies are also improved, allowing for the correct estimation of the inertial properties' distribution.
- The identified properties are reported in terms of stiffness distribution, showing some differences with respect to the nominal design, suggesting a revisiting of the manufacturing process to improve its repeatability. The mass distribution is evaluated on only the blade with the FRFs analysis, and shows very small discrepancies with respect to the nominal.
- The FBG sensors are calibrated from the static tests. The calibration showed an estimation error around 1.1% in the flapping direction and 1.2% in the edge direction. The error is very low, despite the calibration is done with only three of the four FBG sensors installed, due to the unavailability of one.

In Chapter 6 the wind tunnel activities for aerodynamic and load characterization of a scaled wind turbine model equipped with BTC blades is described. The aerodynamic characterization consisted of tests with low turbulence level to obtain the rotor performances in terms of power and thrust coefficients. The load characterization was performed in the boundary layer wind tunnel section, with high turbulence level and partial wake conditions produced by putting ahead a wind turbine model equipped with rigid blades. The model to be characterized was put downwind, and several partial wake conditons were tested, by placing the downwind model at different partial wake positions.

Based on the results obtained so far, the following considerations are drawn:

- The test in the wind tunnel showed little differences with respect to the rotor without BTC in the power coefficient, with the minimum pitch angle passing from -1.7 to -5 degrees.
- Turbulent partial wake tests highlight the capability of the BTC to reduce the fatigue loads on the main bearing and the tower base, but the inertial load contributions determine an increased bending moment on the shaft. Also the actuator duty cycle is reduced considerably. The use of hybrid model IPC+BTC

showed a further reduction of the fatigue loads, and a cut-out of the 1xRev component at the shaft, at the cost of an increased ADC and loads at the blade root.

7.3 Outlook

The passive flap concept could be further developed along different guidelines. The detailed design of the joint, accounting for the stresses to which it is subjected during the life-cycle may raise the problem of an even increased weight due to the joint mass. More sophisticated aerodynamic models should be used to better evaluate the effect on the flap leading edge on the aerodynamic balancing. The effect of the degraded performances due to erosion of the aerodynamic shape may also be accounted, which may suggest the use of different, more resisting materials for the manufacturing of the device. The life-cycle of the mechanical parts of the flap should also be evaluated carefully, since possible failures, such as jamming, (scenarios that are considered in the load analysis), would require some maintenance actions, with impact on availability and costs in the AOE index.

Regarding the blade tip concept, it may also be further developed along different lines. The detailed design of the tip joint should be performed, addressing some critical aspects as the realization of the passive screw joint or the installation of the servo motors. More sophisticated aerodynamic models could be used to take into account the mutual interference between the tip and the inner part of the blade, as well as the vortices shed by the twist discontinuity at the joint [100]. The control system could be re-tuned to better account for the presence of the tip devices, while shut-down procedures could also be revisited at least in the active tip case.

Finally, the integration of the appended devices in a rotor redesign activity [101] could shed light on the actual potential beneficial effects on CoE, or lack thereof.

Concernign the scaled multi-MW blades with BTC, at the light of the mismatches between the manufactured blades with BTC and the nominal design in terms of structural properties distribution, the manufacturing process should be revised with the goal of improving its repeatability.

Full-blade span solutions require further investigation to assess the synergy between passive and active solutions. Indeed, the analysis of the blade load measured by the FBG sensors conducted on the BTC and hybrid BTC+IPC models showed that the IPC implemented here by doing feedback on the shaft bending moments negatively affects the blades loads. Therefore an implementation of the feedback law by using the blade root bending component, like the one simulated by [25] may reveal a better choice. The increased ADC due to the IPC may be mitigated by fine tuning of the IPC gains, possibly using the reduction margin provided by the BTC technology.

Bibliography

[1] GWEC, 2015. Global wind report: annual market update.

[2] Lindvig, K., 2011. The installation and servicing of offshore wind farms, European Forum for Renewable Energy Sources, A2SEA.

[3] Fingersh, L. , Hand, M., Laxson, A., 2006. Wind Turbine Design Cost and Scaling Model, Technical Report NREL/TP-500-40566, National Renewable Energy Laboratory, Colorado.

[4] Thresher, R., Schreck, S., Robinson, M., Veers, P., 2008. Wind Energy Status and Future Wind Engineering Challenges. 1st American Association for Wind Engineering Workshop, Vail, CO.

[5] Andersen, P. B., Henriksen, L., Gaunaa, M., Bak, C., Buhl, T., 2010. Deformable trailing edge flaps for modern megawatt wind turbine controllers using strain gauge sensors. Wind Energy, 13, 193–206. doi:10.1002/we.371.

[6] Bergami, L., Poulsen, N. K., 2015. A smart rotor configuration with linear quadratic control of adaptive trailing edge flaps for active load alleviation. Wind Energy, 18, 625–641. doi:10.1002/we.1716.

[7] Bernhammer, L.O., De Breuker, R., Van Kuik, G.A.M, 2015. Fatigue and extreme load reduction of wind turbine components using smart rotors, Journal of Wind Engineering and Industrial Aerodynamics, submitted.

[8] Chow, R., van Dam, C.P., 2007. Computational Investigations of Deploying Load Control Microtabs on a Wind Turbine Airfoil. 45th AIAA Aerospace Sciences Meeting and Exhibit, Reno, NV. doi:10.2514/6.2007-1018.

[9] Lachenal, X., Daynes, S., Weaver, P. M., 2013. Review of morphing concepts and materials for wind turbine blade applications. Wind Energy, 16, 283–307. doi:10.1002/we.531.

[10] Donely, P., Shufflebarger, C.C., 1940. Test of a Gust-Alleviating Flap in the Gust Tunnel, Tech. Report 745, NACA.

[11] Bielawa, R.L, 1984. Analytic Investigation of Helicopter Appended Aeroelastic Devices. NACA Report 166525, NASA Ames Research Center.

[12] Stroub, R.H., 1982. An Analytical Investigation of the Free-Tip Rotor for Helicopters. NASA Technical Memorandum 81345.

[13] Stroub, R.H., 1985. Analysis of the Free-Tip Rotor Wind-Tunnel Test Results. NASA Technical Memorandum 86751.

[14] Young, L.A., 1986. The Evaluation of a Number of Prototypes for the Free-Tip Rotor Constant-Moment Controller. NASA Technical Memorandum 86664.

[15] Louie, A., 1988. An Experimental and Analytical Evaluation of the Tapered Tension-Torsion Strap Concept. NASA Technical Memorandum 101049.

[16] Konstanzer, P., Enenkl, B., Aubourg, P. A., Cranga, P., 2008. Recent advances in Eurocopter's passive and active vibration control. American Helicopter Society 64th Annual Forum. Montréal, Canada, April 29th – May 1st.

[17] Lambie, B., Jain, P., Tropea, C., 2011. Passive camber change for wind turbine load alleviation. AIAA Aerospace Sciences Meeting including the New Horizons Forum and Aerospace Exposition, Orlando, Florida.

[18] Marten, D., Spiegelberg, H., Pechlivanoglou, G., Nayeri, C. N., Paschereit, C. O., Tropea, C., 2015. Configuration and Numerical Investigation of the Adaptive Camber Airfoil as Passive Load Alleviation Mechanism for Wind Turbines, 33rd AIAA Applied Aerodynamics Conference. doi:10.2514/6.2015-3390.

[19] Arrieta, A.F., Bilgen, O., Friswell, M.I., Hagedom, P., 2012. Passive load alleviation bi-stable morphing concept. AIP Advances, 2, DOI: 10.1063/1.4739412.

[20] Arrieta, A.F., Kuder, I.K., Rist, M., Waeber, T., Ermanni, P., 2014. Passive load alleviation aerofoil concept with variable stiffness multi-stable composites. Composite Structures, 116, 235–242, DOI:10.1016/j.compstruct.2014.05.016.

[21] Bottasso, C.L., Croce, A., Gualdoni, F., Montinari, P., 2015. Load mitigation for wind turbines by a passive aeroelastic device, Journal of Wind Engineering and Industrial Aerodynamics, 148, 57–69.

[22] Van Kuik, G.A.M., Dekker, J.W.M., 1992. The FLEXHAT program, technology development and testing of flexible rotor systems with fast passive pitch control. J. Wind Eng. Ind. Aerod., 39, 435–448. doi:10.1016/0167-6105(92)90567-T.

[23] Hagg F., Joosse P.A., van Kuik G.A.M., Beurskens J.H.M., Dekker J. W. M., 1993. The results of the Dutch exhat program, the technology for the next generation of wind turbines. Proceedings of Windpower 93, San Francisco, CA.

[24] Bottasso, C.L., Croce. A., Gualdoni, F., Montinari, P., Riboldi, C., 2016. Articulated blade tip devices for load alleviation on wind turbines, Wind Energy Science, submitted and under revision.

[25] Bottasso, C.L., Campagnolo, F., Croce, A., Tibaldi, C., 2013. Optimization-based study of bend-twist coupled rotor blades for passive and integrated passive/active load alleviation. Wind Energy 16, 1149–1166. doi:10.1002/we.1543.

[26] Bossanyi, E. A., 2003. Individual blade pitch control for load reduction, Wind Energy, 6/2, 119-128.

[27] Bottasso, C. L., Croce, A., Riboldi, C. E. D., Nam, Y., 2013. Multi-Layer Control Architecture for the Reduction of Deterministic and Non-Deterministic Loads on Wind Turbines, Renewable Energy, 51, 159–169.

[28] Geyler, M. and Caselitz, P., 2007. Individual blade pitch control design for load reduction on large wind turbines, Proceedings of the European Wind Energy Conference, Milan, Italy.

[29] Kanev, S., and Van Engelen, T., 2010. Exploring the limits in individual pitch control, Wind Energy, 13, 18–35.

[30] Bossanyi, E. A., Wright, A., and Fleming, P., 2010. Further progress with field testing of individual pitch control, European Wind Energy Conference, Warsaw, Poland.

[31] Ashwill, T., 2010. Passive load control for large wind turbines, 51-st SDM Conference, Orlando, FL, USA.

[32] Capellaro, M., and Kühn, M., 2010. Boundaries of bend twist coupling, In Proceedings of TORQUE 2010: The Science of Making Torque from Wind, June 28-30, Crete, Greece.

[33] Berring, P., Branner, K., Berggreen, C., and Knudsen, H. W., 2007. Torsional performance of wind turbine Blades-Part I: Experimental investigation,16-th International Conference on composite materials, Kyoto, Japan.

[34] Branner, K., Berring, P., Berggreen, C., Knudsen, H., 2007. Torsional Performance of Wind Turbine Blades: Part II: Numerical Validation, 16-th International Conference on Composite Materials, Kyoto, Japan.

[35] Luczak, M., Manzato, S., Peeters, B., Branner, K., Berring, P., and Kahsin, M., 2011. Dynamic investigation of twist-bend coupling in a wind turbine blade, Journal of theoretical and applied mechanics, 49, 765–789.

[36] Bottasso, C. L., Campagnolo, F., Petrović, V., 2014. Wind tunnel testing of scaled wind turbine models: Beyond aerodynamics, Journal of Wind Engineering and Industrial Aerodynamics, 127, 11–28.

[37] Bak,C., Zahle, F.,Bitsche, R., Kim, T., Yde, A., Henriksen, L.C., Andersen, P.B., Natarajan, A., Hansen, M.H., 2013. Description of the DTU 10MW Reference Wind Turbine. DTU Wind Energy Report-I-0092.

[38] Guideline for the Certification of Wind Turbines, Ed. 2010. Germanischer Lloyd Industrial Services GmbH, Renewables Certification, Brooktorkai 10, 20457 Hamburg, Germany.

[39] Wind Turbines — Part 1: Design Requirements, Ed. 3. International Standard IEC 61400-1, 2005.

[40] Jonkman, J., Butterfield, S., Musial, W., and Scott, G., 2009. Definition of a 5-MW Reference Wind Turbine for Offshore System Development. Technical Report NREL/TP-500-38060, URL `http://www.nrel.gov/docs/fy09osti/38060.pdf/`.

[41] Bak, C., Zahle, F., Bitsche, R., Kim, T., Yde, A., Henriksen, L. C., Natarajan, A., 2013. The DTU 10-MW Reference Wind Turbine. Danish Wind Power Research, Fredericia, Denmark, URL `http://dtu-10mw-rwt.vindenergi.dtu.dk`.

[42] Schubel, P.J., Crossley, R.J. , Boateng, E.K.G., Hutchinson, J.R., 2013. Review of structural health and cure monitoring techniques for large wind turbine blades, Renewable Energy, 51, 113–123, doi:10.1016/8.2012-72, URL `http://www.sciencedirect.com/science/article/pii/S0960148112005423`.

[43] Bottasso, C.L., Croce, A., 2006–2015. `Cp-Lambda` User's Manual. Dipartimento di Scienze e Tecnologie Aerospaziali, Politecnico di Milano, Milano, Italy.

[44] Bauchau, O.A., Epple, A., Bottasso, C.L., 2009. Scaling of constraints and augmented Lagrangian formulations in multibody dynamics simulations. Journal of Computational and Nonlinear Dynamics, 4(2), DOI:10.1115/1.3079826.

[45] Bauchau, O.A., Bottasso, C.L., Trainelli, L., 2003. Robust integration schemes for flexible multibody systems. Computer Methods in Applied Mechanics and Engineering, 192, 395–420, DOI:10.1016/S0045-7825(02)00519-4.

[46] Hansen, M.O.L., 2008. Aerodynamics of Wind Turbines, 2nd Edition. Earthscan.

[47] Kelley, N., Jonkman, B., 2015. NWTC Computer-Aided Engineering Tools: TurbSim. http://wind.nrel.gov/designcodes/preprocessors/turbsim/.

[48] Bottasso, C.L., Croce, A., Devecchi, D., Riboldi, C.E.D, Nam, Y., 2013. Multi-layer control architecture for the reduction of deterministic and non-deterministic loads on wind turbines. Renewable Energy 51, 159–169.

[49] Bisplinghoff, R.L., Ashley H., 1962. Principles of Aeroelasticity. John Wiley & Sons, Inc., Hoboken, New Jersey.

[50] Theodorsen, T., Garrik, I.E., 1935. General Theory of Aerodynamic Instability and the Mechanism of Flutter. Tech. Report 496, NACA.

[51] Theodorsen, T., Garrik, I.E., 1942. Nonstationary Flow About a Wing-Aileron-Tab Combination Including Aerodynamic Balance. Tech. Report 736, NACA.

[52] Leishman, J.G., 2006. Principles of Helicopter Aerodynamics, 2nd Edition. Cambridge University Press, Cambridge, England.

[53] Kanda, A., Dowell, H., 2005. Worst-case gust-response analysis for typical airfoil section with control surface. Journal of Aircraft, 42 (4), 956–962.

[54] DTU 10 MW Reference Wind Turbine Project, 2015. Web site: http://dtu-10mw-rwt.vindenergi.dtu.dk.

[55] Bak, C., Zahle, F., Bitsche, R., Kim, T., Yde, A., Henriksen, L.C., Andersen, P.B., Natarajan, A., Hansen, M.H., 2015. Design and performance of a 10 MW wind turbine. Wind Energy, to appear.

[56] Bak, C., Bitsche, R., Yde, A., Zahle, F., Gaunaa, M., Blasques, J., Døssing, M., Heinen, J.J.W., Behrens, T., 2012. DTU 10 MW Reference Wind Turbine Project. http://orbit.dtu.dk/fedora/objects/orbit:111503/datastreams/file_7946742/content.

[57] Hodges, D.H., Pierce, G.A., 2002. Introduction to Structural Dynamics and Aeroelasticity. Cambridge Aerospace Series, Cambridge University Press.

[58] Bottasso, C. L., Campagnolo, F., and Croce, A., 2011. Multi-Disciplinary Constrained Optimization of Wind Turbines, Multibody System Dynamics, 27/1, 21–53, doi:10.1007/s11044-011-9271-x.

[59] ESDU, 1989. Item No. 89010, URL https://www.esdu.com/cgi-bin/ps.pl?sess=unlicensed_1160924094047vzh&t=doc&p=esdu_89010

[60] Wentz, W.H., Snyder, M.H., Calhoun, J.T., 1980. Feasibility study of aileron and spoiler control systems for large horizontal axis wind turbines, NASA Tech. Report, DOE/NASA/3277-1-NASA CR-159856 WER-10, URL http://ntrs.nasa.gov/archive/nasa/casi.ntrs.nasa.gov/19800019302.pdf

[61] Drela, M., Yougren, H., 2001. Xfoil Subsonic Air Development System, URL http://web.mit.edu/drela/Public/web/xfoil/xfoil_doc.txt.

[62] Bauchau, O.A., Rodriguez, J., Bottasso, C.L., 2001. Modeling of Unilateral Contact Conditions with Application to Aerospace Systems Involving Backlash, Freeplay and Friction, Mechanics Research Communications, 28, 571–599.

[63] Jonkman, B. J., Buhl, M. L., 2006. TurbSim user's guide. Golden, Co, National Renewable Energy Laboratory.

[64] Bottasso, C.L., Croce, A., Nam, Y., Riboldi, C.E.D., 2011. Power curve tracking in the presence of a tip speed constraint. Renew. Energ., 40, 1–12. doi:10.1016/j.renene.2011.07.045.

[65] Bottasso, C.L., Croce, A., Savini, B., Sirchi, W., Trainelli, L., 2006. Aero-servo-elastic modeling and control of wind turbines using finite-element multi-body procedures. Multibody Syst. Dyn., 16, 291–308. doi:10.1007/s11044-006-9027-1.

[66] Hansen, M.H., Henriksen, L.C., 2013. Basic DTU Wind Energy controller. DTU Wind Energy Report-E-0018.

[67] Stroub, R.H., Kumagai, H., Keys, C., 1986. Wind tunnel test of a model rotor with a free-tip, 4th Applied Aerodynamics Conference, San Diego, CA. doi:10.2514/6.1986-1781.

[68] Martin, D.M., Fortin, P.E., 1988. VSAERO Analysis of tip Planforms for the Free-Tip Rotor. NASA Contractor Report 177487.

[69] Bossanyi, E., 2003. Wind turbine control for load reduction. Wind Energy, 6, 229–244. doi:10.1002/we.95.

[70] Bossanyi, E., 2003. Individual blade pitch control for load reduction. Wind Energy, 6, 119–128. doi:10.1002/we.76.

[71] Bossanyi, E., 2005. Further load reductions with individual pitch control. Wind Energy, 8, 481–485. doi:10.1002/we.166.

[72] Leithead, W.E., Neilson, V., Dominguez, S., 2009. Alleviation of unbalanced rotor loads by single blade controllers. European Wind Energy Conference (EWEC 2009), Marseille, France.

[73] Johnson, W., 2013. Rotorcraft Aeromechanics. Cambridge University Press, ISBN: 978-1-107-02807-4.

[74] Van Engelen, T. G., 2006. Design Model and Load Reduction Assessment for Multi-rotational Mode Individual Pitch Control (Higher Harmonics Control). Proceeding of European Wind Energy Conference (EWEC 2006), Athens, Greece, February 27th – March 2nd.

[75] Althaus, D., 1998. ProfilPolaren für den Modellflung, Band 1. Institut für Aerodynamik und Gasdynamik der Universität Stuttgart, Necktar-Verlag, Vs-Villingen.

[76] Olesen, N., 2009. Personal communication. Vestas Wind Systems. Aarhus, Denmark.

[77] Bernhard, A., and Chopra, I., 2002. Hover test of a Mach-Scale Rotor Model with active blade tips, Journal of the american helicopter society, 47, 273–284.

[78] Jinsong B., Nagaraj V., Chopra I. and Bernhard A., 2008. Wind Tunnel Test of Five Sets of Mach Scale Composite Tailored Rotor with Flap-Bending/Torsion Couplings for Vibration Reduction, Journal of the american helicopter society, 53, 215–225.

[79] Anonymus: Evonik Corporation Rohacell®71 WF High Heat Grade Polymethacrylimide (PMI) Foam, MatWeb, URL `http://www.matweb.com/`.

[80] Sala, G., Di Landro, L., Airoldi, A., Bettini, P., 2015. Fiber optics health monitoring for aeronautical applications, Meccanica, 50/10, 2547–2567.

[81] Anonymous: Toray Company, Web Site: URL `http://www.toraycompam.com/`

[82] Anonymus, 2009. 3M Scotch-Weld Structural Adhesive Film AF 163-2, Technical Datasheet, Aerospace and Aircraft Maintenance Department 3M Center, Building 223-1N-14 St. Paul, MN 55144-1000, 1-800-235-2376, URL `http://www.3M.com/aerospace/`.

[83] Anonymous, 2000. Standard Test Method for Tensile Properties of Polymer Matrix Composite Materials, Standard Designation D 3039/D 3039 M, Approved by agencies of the Department of Defense.

[84] Bottasso, C.L., Campagnolo, F., Croce, A., Dilli, S., Gualdoni, F., Nielsen, M.B., 2013. Structural Optimization of Wind Turbine Rotor Blades by Multi-Level Sectional/Multibody/3DFEM Analysis, Multibody System Dynamics, doi:10.1007/s11044-013-9394-3.

[85] Lobitz D., Veers, P.S., Laino, D., 2000. Performance of twist-coupled blades on variable speed rotors, ASME Wind Energy Symposium, Reno, January 10â13, doi:10.2514/6.2000-62.

[86] Anonymus, 2010. The Fastest, Solver Neutral CAE Environment for High Fidelity Modeling, HyperMesh, part of HyperWorks, Altair Engineering, Troy, MI.

[87] Giavotto, V., Borri, M., Mantegazza, P., Ghiringhelli, G., Carmaschi, V., Maffioli, G.C., Mussi, F., 1983. Anysotropic beam theory and applications, Computers and Structures, 16(1-4), 403–413.

[88] Piegl, L., Tiller, W., 1996. The NURBS Book (Monographs and Visual Communications), Springer, 2ns edition.

[89] Lobitz, D.W., Laino, D.J., 1999. Load mitigation with twist-coupled HAWT blades, ASME Wind Energy Symposium, Reno, January 11â14, doi:10.2514/6.1999-33.

[90] Bauchau, O.A., 2011. Flexible Multibody Dynamics, Solid Mechanics and its Applications, Vol. 176, Springer, Dordrecht Heidelberg London New York.

[91] Jategaonkar, R. V., 2006. Flight Vehicle System Identification: a Time Domain Methodology, AIAA, Education Series, Reston, VA, USA.

[92] Klein, V. and Morelli E. A., 2006. Aircraft System Identification, Theory and Practice, AIAA Education Series, Reston, VA, USA.

[93] Jategaonkar, R. V., 2006. Flight Vehicle System Identification: a Time Domain Methodology, AIAA, Education Series, Reston, VA, USA.

[94] Barclay, A., Gill, P. E. and Rosen, J. B., 1997. SQP methods and their application to numerical optimal control, Report NA 97â3, Department of Mathematics, University of California, San Diego, CA.

[95] Barclay, A., Gill, P.E., Rosen, J.B., 1997. SQP methods and their application to numerical optimal control, Report NA 97-3, Department of Mathematics, University of California, San Diego, CA.

[96] Cramér, H., 1946. Mathematical Methods of Statistics, Princeton University Press, Princeton, NJ, USA.

[97] Bottasso, C.L., Cacciola, S., 2014. Estimation of wind turbine model properties â Towards the validation of comprehensive high-fidelity multibody models, Proceedings of the EWEA 2014 Annual Event, Barcelona, Spain, March, 10–13.

[98] Bahaj ,A.S., Molland, A.F., Chaplin, J.R., Batten, W.M.J., 2007. Power and thrust measurements of marine current turbines under various hydrodynamic flow conditions in a cavitation tunnel and a towing tank, Renewable Energy, 32/3, 407â-426.

[99] Campagnolo, F., Wind tunnel testing of scaled wind turbine models, PhD dissertation, Politecnico di Milano, Dipartimento di Scienze e Tecnologie Aerospaziali, Doctoral Programme in Rotary Wing Aircraft, 2013.

[100] Van Aken, J. M., Stroub, R. H., 1986. Tip Aerodynamics From Wind Tunnel Test of Semi-Span Wing. NASA Technical Memorandum 88253.

[101] Bottasso, C.L., Bortolotti, P., Croce, A., Gualdoni, F., 2015. Integrated aero-structural optimization of wind turbines. Multibody Syst. Dyn., 1–28, doi:10.1007/s11044-015-9488-1.